Conductance Fluctuations in GaAs Nanowires and Graphene Nanoribbons

by

Bobo Liu

A Dissertation Presented in Partial Fulfillment
of the Requirements for the Degree
Doctor of Philosophy

Approved May 2015 by the
Graduate Supervisory Committee:

David Ferry, Chair
Richard Akis
Marco Saraniti
Michael Goryll

ARIZONA STATE UNIVERSITY

August 2015

ABSTRACT

In mesoscopic physics, conductance fluctuations are a quantum interference phenomenon that comes from the phase interference of electron wave functions scattered by the impurity disorder. During the past few decades, conductance fluctuations have been studied in various materials including metals, semiconductors and graphene. Since the patterns of conductance fluctuations is related to the distributions and configurations of the impurity scatterers, each sample has its unique pattern of fluctuations, which is considered as a sample fingerprint. Thus, research on conductance fluctuations attracts attention worldwide for its importance in both fundamental physics and potential technical applications. Since early experimental measurements of conductance fluctuations showed that the amplitudes of the fluctuations are on order of a universal value (e^2/h), theorists proposed the hypothesis of ergodicity, e.g. the amplitudes of the conductance fluctuations by varying impurity configurations is the same as that from varying the Fermi energy or varying the magnetic field. They also proposed the principle of universality; e.g., that the observed fluctuations would appear the same in all materials. Recently, transport experiments in graphene reveal a deviation of fluctuation amplitudes from those expected from ergodicity.

Thus, in my thesis work, I have carried out numerical research on the conductance fluctuations in GaAs nanowires and graphene nanoribbons in order to examine whether or not the theoretical principles of universality and ergodicity hold. Finite difference methods are employed to study the conductance fluctuations in GaAs nanowires, but an atomic basis tight-binding model is used in calculations of graphene nanoribbons. Both short-range disorder and long-range disorder are considered in the simulations of

graphene. A stabilized recursive scattering matrix technique is used to calculate the conductance. In particular, the dependence of the observed fluctuations on the amplitude of the disorder has been investigated. Finally, the root-mean-square values of the amplitude of conductance fluctuations are calculated as a basis with which to draw the appropriate conclusions. The results for Fermi energy sweeps and magnetic field sweeps are compared and effects of magnetic fields on the conductance fluctuations of Fermi energy sweeps are discussed for both GaAs nanowires and graphene nanoribbons.

ACKNOWLEDGMENTS

First of all, I would like to express my deep gratitude to my advisor, Prof. Ferry, for his strong support and patient guidance on my Ph.D. research work during these years. I also want to thank his suggestions and assistance at every stage of my research project. I am always grateful for his help and encouragement each time when I turn to a new research step. I feel lucky to have the opportunity to be one of his students.

I would like to specially thank Prof. Akis for his academic support throughout my Ph.D. study. I appreciate his valuable suggestions and time that helps me a lot when I was facing problems. I am also grateful for Prof. Saraniti and Prof. Goryll for working as my graduate committee and providing me valuable suggestions on my research work.

I also want to thank my colleague Srinivasa Varadan Ramanujam for many interesting discussions on academic topics and life experiences.

Finally, I would like to thank my parents for their entire and full support in my study and life overall wholeheartedly.

TABLE OF CONTENTS

Page

CHAPTER Page

LIST OF FIGURES

Figure Page

Figure Page

Figure Page

Figure Page

Figure Page

CHAPTER 1

INTRODUCTION AND HISTORICAL REVIEW

1.1 Basic concepts of quantum transport

In this section, some important concepts in condensed matter physics and electron transport theory are introduced as a preparation for the following chapters. In quantum mechanics, the superposition principle is used to create a composite wave function which is the sum of the individual electron wave functions, so the interference between different electron waves may be observed [1]. If we write

$$\psi(x,y,z,t) = \psi_A(x,y,z,t) + \psi_B(x,y,z,t) \ , \tag{1.1}$$

then

$$n(x,y,z,t) = \left|\psi(x,y,z,t)\right|^2 = \psi(x,y,z,t)\psi^*(x,y,z,t) \ . \tag{1.2}$$

The square of the composite wave amplitudes will be the probability for the electrons to be found at that position. The observation of the famous Aharonov–Bohm effect [2, 3, 4, 5] at low-temperature experiments can be explained by the theory of coherent electron wave interference, which is similar to the phenomenon of coherent optical wave interference in Young's double-slit experiment [6, 7]. In Fig. 1.1(a), a simplified schematic of the experimental setup of the interference of electron wave is presented and the experimental schematic of the Young's double slits experiment is given in Fig. 1.1(b). In theory, the concepts of wave functions, which are the solutions of Schrödinger's equation, are the widely-used interpretation of quantum states in the wave mechanics version of quantum theory [1]. Schrödinger's equation is

$$i\hbar\frac{\partial y}{\partial t}\psi = \hat{H}\psi \tag{1.3}$$

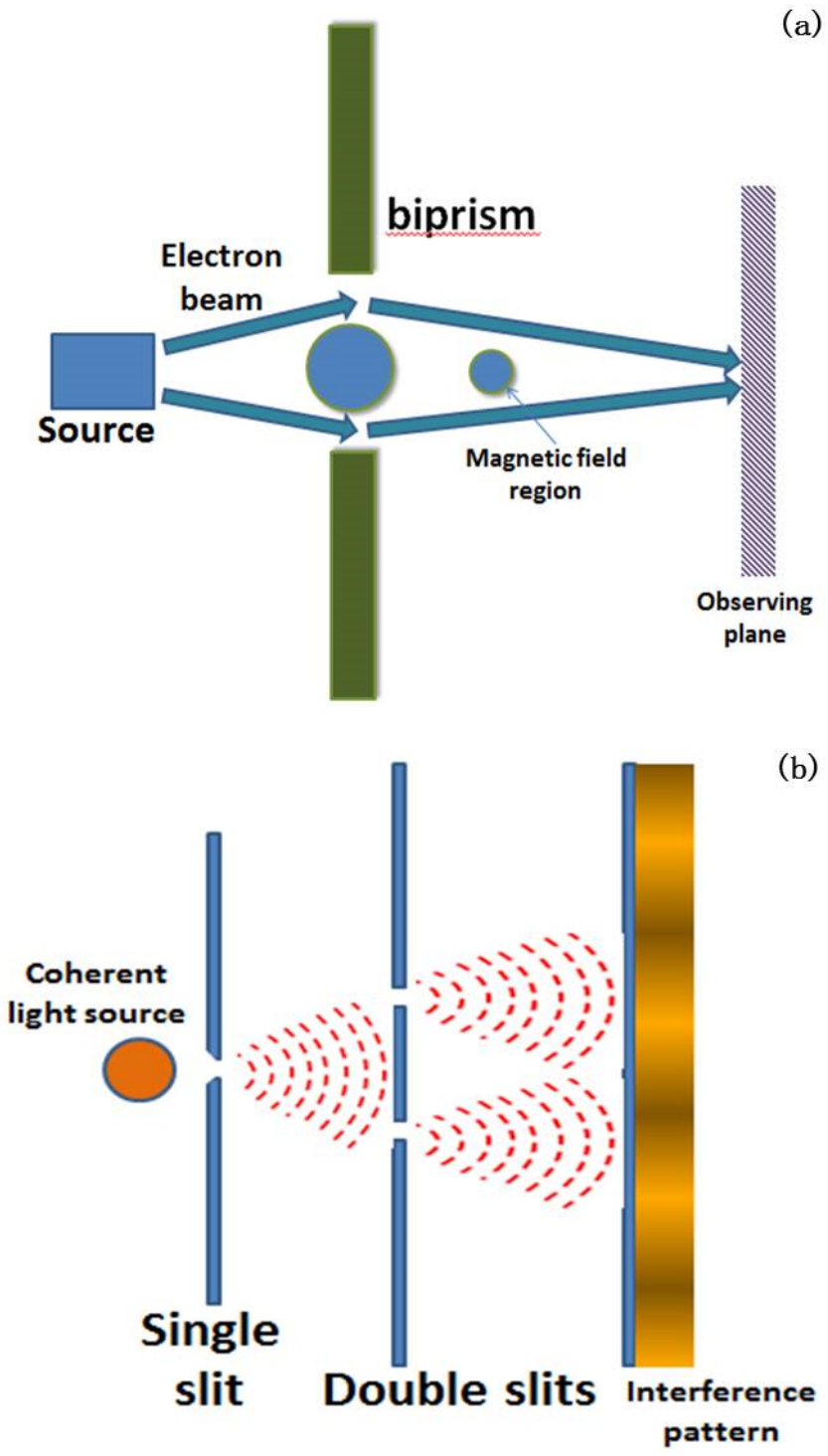

Fig. 1.1 (a) A simplified experimental schematic of the electron wave interference measurement [2, 3, 4, 5]. (b) A simplified schematic of the Young's double slit interference experiment [6, 7].

In studying quantum transport problems in small mesoscopic systems, such as a quantum point contact or nanowires, one important approach is the use of the Landauer formula [8, 9]. It relates the conductance of a nanowire to the transmission probabilities of electrons propagating in different channels in the wires. In this thesis, the conductance of both GaAs nanowires and graphene nanoribbons are calculated using the Landauer formula

$$G = \frac{2e^2}{h}\sum_{i=1}^{n} T_i = N \cdot \frac{2e^2}{h} \ . \tag{1.4}$$

A simplified potential landscape of a typical quantum point contact for a GaAs two-dimensional electron gas (2DEG) is shown in Fig. 1.2 (a) [10, 11, 12]. If I increase the width of the constriction in the quantum point contact, the number of propagating modes will increase gradually, so the conductance also increase in unit of $2e^2/h$. The results are presented in Fig. 1.2 (b). The conductance is also calculated using different grid sizes from 0.5nm to 5nm.

One important concept in the physics of electron transport is the relaxation time. As the electrons travel inside the crystal, they will experience several scattering events and the average time during which the initial momentum of an electron is reversed by scattering is defined as the relaxation time [13]. Then the average distance an electron travels before backscattering is the mean free path. Considering the interference effect of electron waves, the concepts of phase-breaking time and phase-breaking length are used to describe the average time and distance that electrons diffuse in the material before their phase information is disrupted through scattering events [14]. So, in order to observe the interference effect of electron waves, the sample size needs to be comparable to the

phase-breaking length and the experiments are performed at very low temperature, because the phase-breaking length decays as temperature increases [15].

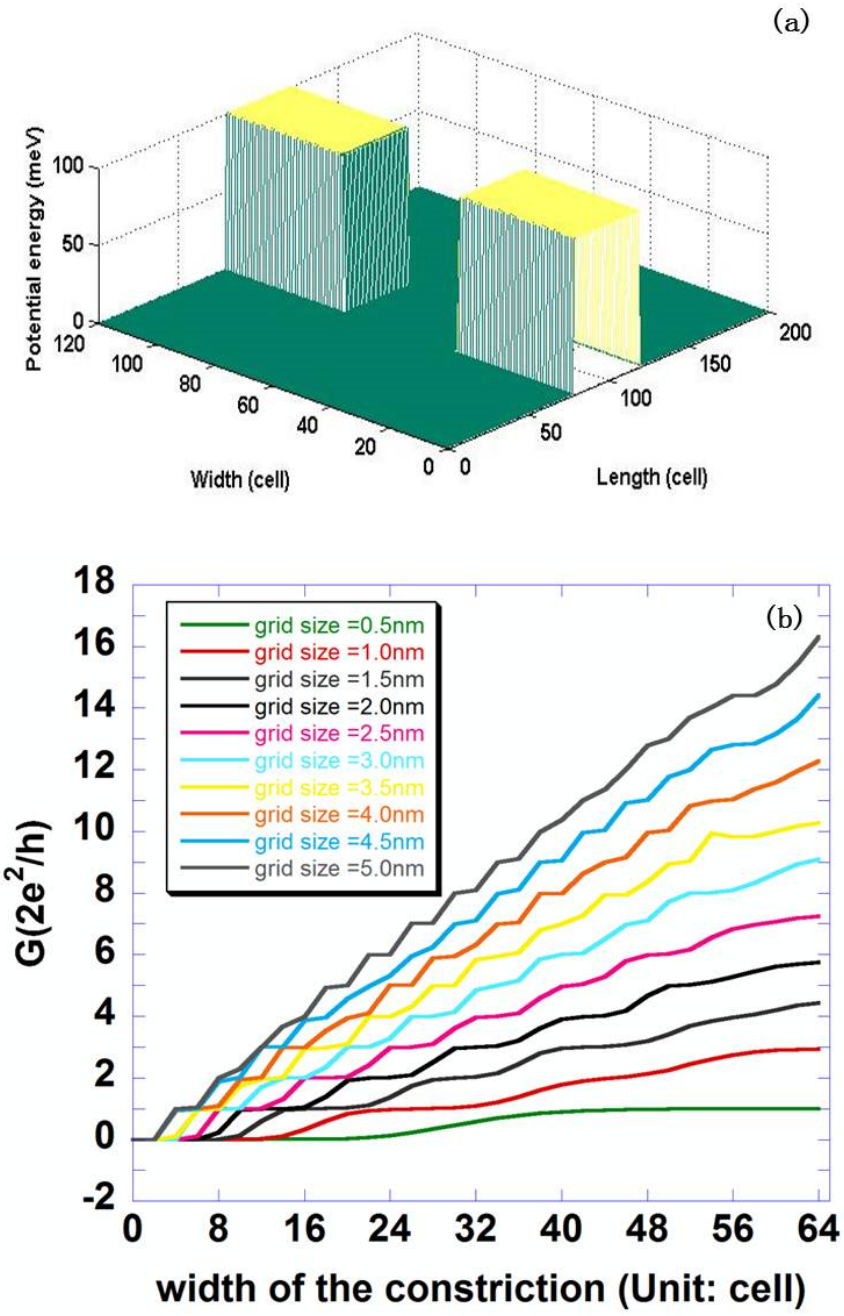

Fig. 1.2 (a) The potential landscape of a typical quantum point contact. (b) The conductance as a function of the width of the constricting region of a quantum point contact for different grid sizes.

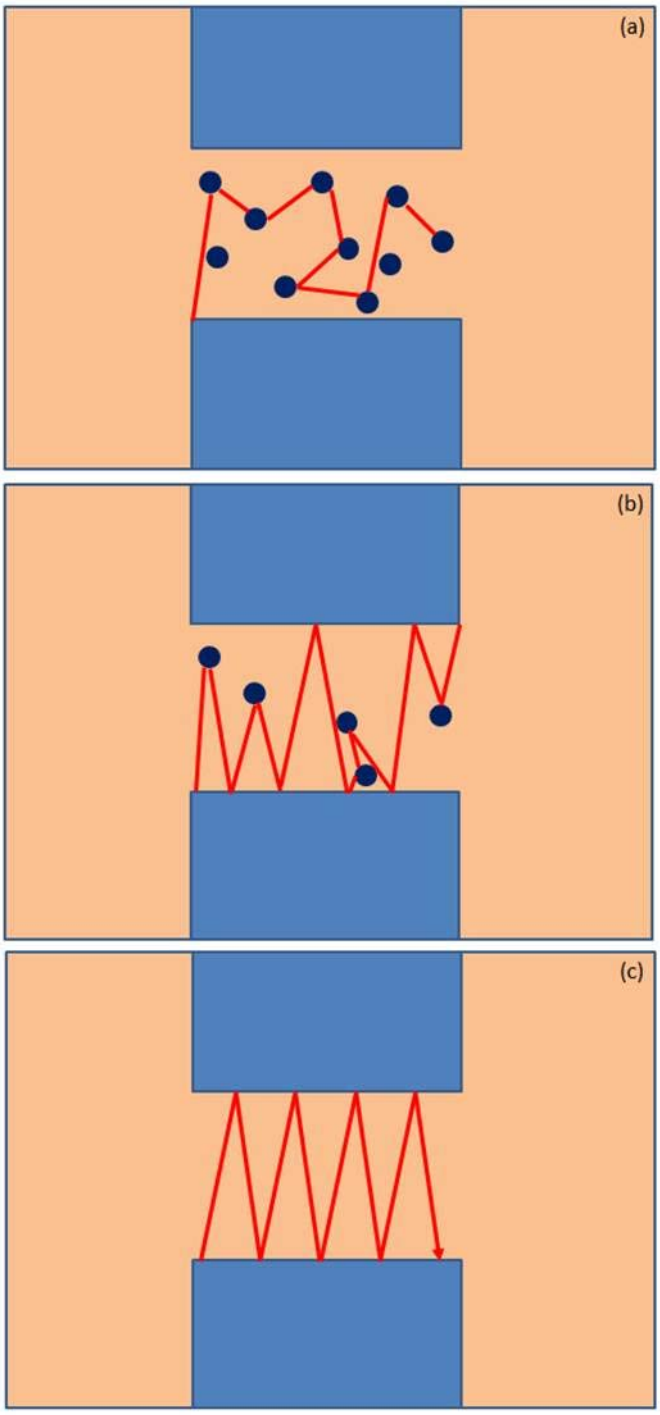

Fig. 1.3 (a) Diffusive transport in a quantum point contact. (b) Quasi-ballistic transport in a quantum point contact. (c) Ballistic transport in a quantum point contact [17].

Based on the size of the nanostructure and mean free path, the electron transport in nanostructure can be studied in three different regimes [16]. In cases that the device size is much larger than the mean free path, the electron transport is in the diffusive regime. If the size of nanostructure is comparable to the mean free path, it is quasi-ballistic transport. Finally, ballistic transport means that there are no impurities, and the scattering mainly take place at the boundaries of the devices. In Fig. 1.3, a schematic diagram for the diffusive transport (Fig. 1.3 (a)), quasi-ballistic transport (Fig. 1.3 (b)) and the ballistic transport (Fig. 1.3 (c)) in a simple structure of a quantum point contact are presented.

1.2 Universality of conductance fluctuations

At zero temperature, when the electron transport in the disordered sample is diffusive or quasi-ballistic as discussed above, there will be quantum interference between different paths that electrons travel along as indicated in Fig.1.4. Then, the conductivity of the conductor will have a correction due to interference of the scattered electron waves. If we vary the Fermi energy or the magnetic fields, the paths that the electrons travel along will be varied and, correspondingly, the electron wave interference patterns will be changed too. Thus, the conductance of the conductor will fluctuate as a function of the Fermi energy or magnetic field [17]. Based on the theory given by Lee and Stone [18, 19], the amplitude of the conductance fluctuations is of the order e^2/h. This feature is termed the universality of conductance fluctuations. Since different samples have their unique distributions of impurities, so the details of the conductance

fluctuations will be different from sample to sample. This feature of the fluctuations is often considered as the fingerprint of a given sample [17].

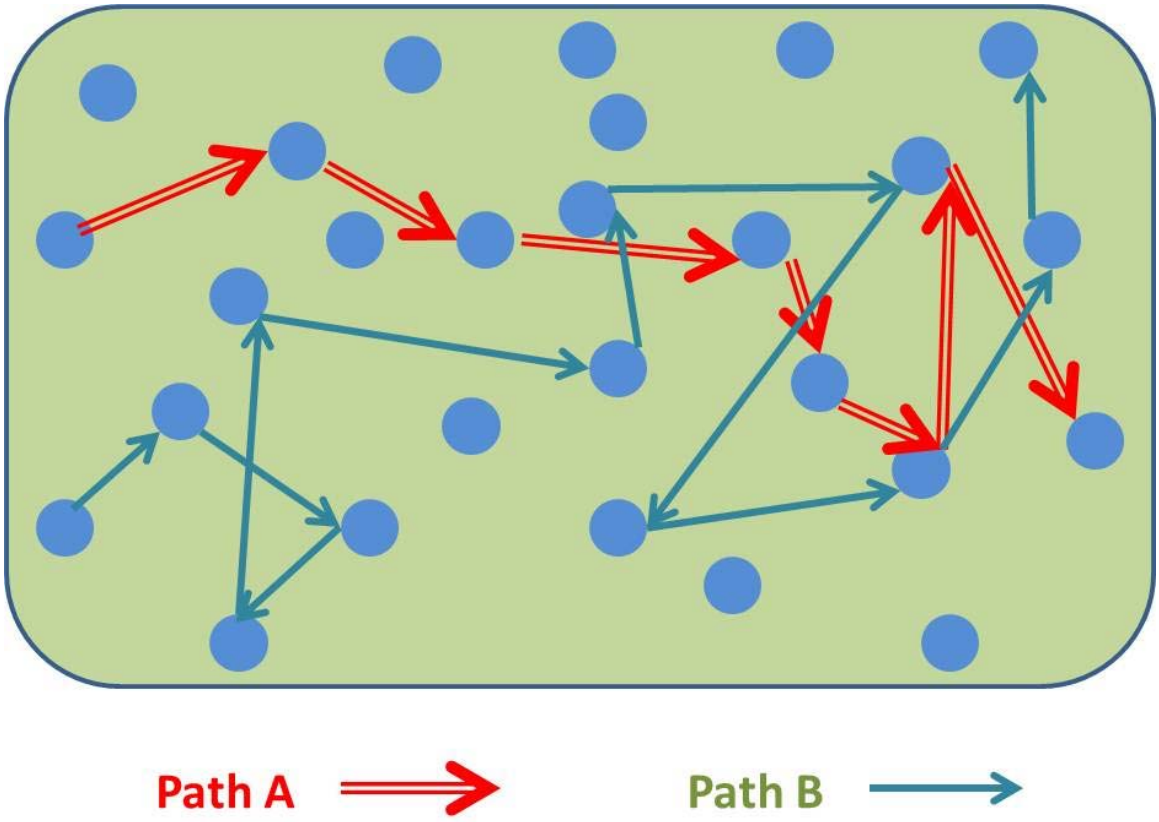

Fig. 1.4 Two paths that electrons travel along in the disordered sample [17].

Here, I briefly summarize the calculations of universal value of conductance fluctuations from C. W. J. Beenakker and H. van Houten [17, 20] at zero temperature. The calculation begins with the expression of the variance of conductance

$$Var(G) = \left\langle \left(G - \langle G \rangle \right)^2 \right\rangle . \tag{1.5}$$

Then the current conservation relation gives a relation between the transmission coefficient and reflection coefficient as

$$\sum_{i,j=1}^{N}\left|t_{ij}\right|^2 = N - \sum_{i,j=1}^{N}\left|r_{ij}\right|^2 \tag{1.6}$$

Assuming that there is no correlation between the reflection probabilities r_{ij} for different pairs (i and j) of incident and reflected channels, so the variance of conductance can be expressed using the variance of the reflection probabilities r_{ij} as

$$Var(G) = \left(\frac{e^2}{h}\right)^2 Var\left(\sum_{i,j=1}^{N}\left|r_{ij}\right|^2\right) = \left(\frac{e^2}{h}\right)^2 N^2 Var\left(\left|r_{ij}\right|^2\right). \tag{1.7}$$

Considering that there are M scattering sequences and the amplitude of contribution of each scattering sequence to the reflection probability amplitude is F (i) (i=1, 2,…, M), then the variance of the reflection probabilities r_{ij} can be simplified as follows

$$Var\left(\left|r_{ij}\right|^2\right) = \left\langle\left|r_{ij}\right|^4\right\rangle - \left\langle\left|r_{ij}\right|^2\right\rangle^2 \tag{1.8}$$

$$\begin{aligned}\left\langle\left|r_{ij}\right|^4\right\rangle &= \sum_{p,q,r,s=1}^{M}\left\langle F^*(p)F(q)F^*(r)F(s)\right\rangle \\ &= \sum_{p,q,r,s=1}^{M}\left\{\left\langle\left|F(p)\right|^2\right\rangle\left\langle\left|F(r)\right|^2\right\rangle\delta_{p,q}\delta_{r,s} + \left\langle\left|F(p)\right|^2\right\rangle\left\langle\left|F(q)\right|^2\right\rangle\delta_{p,s}\delta_{q,r}\right\} \\ &= 2\left\langle\left|r_{ij}\right|^2\right\rangle^2\end{aligned} \tag{1.9}$$

Thus, we obtain $Var\left(\left|r_{ij}\right|^2\right) = \left\langle\left|r_{ij}\right|^2\right\rangle^2$.

Combining $\sum_{i,j=1}^{N}\left|t_{ij}\right|^2 = N - \sum_{i,j=1}^{N}\left|r_{ij}\right|^2$ and $\left\langle\left|t_{ij}\right|^2\right\rangle = \pi l/2NL$, we get

$$\left\langle\left|r_{ij}\right|^2\right\rangle = N^{-1}\left(1 - order\left(l/L\right)\right) \quad , \tag{1.10}$$

where l is the mean free length , and L is the length of sample. Considering the lowest order, Eq. (1.10) becomes $\left\langle \left| r_{ij} \right|^2 \right\rangle \sim N^{-1}$. And the variance of the conductance can be further simplified as

$$Var(G) \sim \left(\frac{e^2}{h} \right)^2 N^2 Var\left(\left| r_{ij} \right|^2 \right) \sim \left(\frac{e^2}{h} \right)^2 N^2 \frac{1}{N^2} \sim \left(\frac{e^2}{h} \right)^2 . \tag{1.11}$$

Finally, we can get a general form for the amplitude of the fluctuations as [17, 20]

$$\delta G = \sqrt{Var(G)} = C \frac{1}{\sqrt{\beta}} \frac{g_s g_v}{2} \frac{e^2}{h} . \tag{1.12}$$

Here, g_s and g_v are spin and valley degeneracy factors. For a narrow channel, C=0.73. And for a wide channel, $C \sim \sqrt{W/L}$, where W is the width and L is the length of the channel. At zero magnetic field, β=1. When the magnetic field is not zero, β=2. At non-zero temperature, the amplitude of conductance fluctuations will be reduced due to the thermal averaging effect and the effect of the phase-breaking length [17, 20].

1.3 Ergodic hypothesis of conductance fluctuations

The properties of universal conductance fluctuations reviewed in section 1.2 can be observed in experimental metal samples under very low temperature. The patterns of the fluctuations depend on the microscopic impurity configurations in specific samples. To connect the statistical experimental results to the analytical theoretical calculations, P. A. Lee *et al*. [19] assume that there is an ergodic hypothesis of conductance fluctuations in metal samples, which suggests that the behavior of the conductance fluctuations in

specific samples by varying impurity configurations is the same as the statistical fluctuations obtained by changing the Fermi energy or magnetic field.

The ergodic hypothesis is supported by some low-temperature experimental results using metal samples as well as some numerical calculations and theoretical analysis using the impurity-averaged perturbation theory [19]. But whether this hypothesis holds in semiconductors and graphene is still an open question. In this thesis, I will use numerical approaches to examine the hypothesis of ergodicity in GaAs nanowires and graphene nanoribbons.

1.4 Conductance fluctuations in metals

In this section, the history of experimental observations or theoretical studies of conductance fluctuations in metals are summarized briefly.

(1) Au and $Au_{60}Pd_{40}$

Early in 1984, small rings made of Au and $Au_{60}Pd_{40}$ were measured under a perpendicular magnetic field from 0 to 1.2 T at very low temperature by Umbach *et al*. [21] When the temperature decreased, the amplitude of the fluctuation of resistance for magnetic field sweeps was observed to get larger. But, the structures of the fluctuations did not change with temperature. The fluctuations of resistance were believed to be related to the small sizes of the samples.

(2) Bi

The low-temperature resistance of small Bi wires and Bi films were measured by Beutler *et al*. in 1987 [22]. They measured the resistance fluctuations as a function of time. The magnitude of these fluctuations agreed with the prediction of universal

conductance fluctuations developed by Lee *et al.* [19]. The resistance fluctuations of the Bi wires and films were thought to come from the motion of small scattering centers inside the samples. The measurements were made up to 5K, and the resistance fluctuations were found to get smaller in amplitude as the temperature rose.

(3) Sb and Au

In 1988, Webb *et al.* [23] measured the conductance as a function of current in Sb and Au wires, and the reproducible conductance fluctuations were observed at low temperature. Again, there was a qualitative agreement between their measurements and theoretical calculations. There were also differences between the fluctuation spectrum for metal loops and wires.

(4) Cu

In 1992, Ralph *et al*. [24] reported experiments using Cu. They conducted measurements of the conductance fluctuations in both ballistic and disordered samples. In ballistic cases, the root-mean-square values of the magnitude of the conductance fluctuations were of the order of $0.02e^2/h$. In disordered samples, the conductance fluctuations for magnetic field sweeps were weak. It was also found that, within a phase coherent sample, the rms values of amplitude of fluctuations did not depend on voltage.

(5) Au films

In 1995, Schäfer *et al*. [25] used gold films to study the conductance fluctuations for bias voltage sweeps and magnetic field sweeps. The sample they used was small enough to be comparable to the elastic mean free path. The fluctuations were thought to mainly come from the diffusive motion of the conduction electrons. They argued that the fluctuations could be used to probe the impurity configurations within the gold samples.

They found that the results of conductance fluctuations for bias voltage sweeps and magnetic field sweeps agreed with the ergodic hypothesis developed by Lee and Stone [18].

(6) Au and Ag

In 1997, Scheer *et al*. [26] reported experiments which examined the dependence of conductance fluctuations in gold and silver wires on the angle between the magnetic field and the current in the wires at low temperature. The experimental data showed that, when varying the angle between the magnetic field and current, the rms amplitude of the conductance fluctuations did not change.

(7) Cu and Ag

In 2001, Haüssler *et al*. [27] studied the conductance fluctuations in the Aharonov-Bohm effect. They investigated the relation between the variations of the microscopic phases of electron waves and the phase of the conductance fluctuations in samples of Cu and Ag. They used dc bias current to tune the phase of the microscopic electron wave functions. They found a correlation between the electron wave function phase and the fluctuation phases. When the phase of electron wave function was changed continuously, the fluctuation phase changed in a quantized way.

(8) Li, Na and Au

In 2007, Chen *et al*. [28] reported a first-principle numerical investigation of conductance fluctuations in monatomic metal chains of Li, Na and Au using the non-equilibrium Green's function method and density functional theory. The conductance was calculated as a function of the magnetic field and different energy levels. The results showed that the amplitudes of the conductance fluctuations in the metal chains were

smaller than the theoretical predictions by Lee *et al*. [18], suggesting a failure of the ergodic hypothesis in their results.

(9) $Ni_{0.8}Fe_{0.2}$

Since many investigations on quantum coherence effects in normal metals had been made, in 2004, S Lee *et al.* [29] turned to the measurement of conductance fluctuations in ferromagnetic metals $Ni_{0.8}Fe_{0.2}$. The time-dependent fluctuations were measured at different temperatures and magnetic fields. It was found that the conductance fluctuations were enhanced by the domain wall motion, since the domain wall may be treated as a scattering center. It was felt that a two level system may be the dominant cause of the fluctuations.

1.5 Conductance fluctuations in semiconductors

In this section, I briefly review and summary some historical experimental or theoretical research work on conductance fluctuations in semiconductor devices.

(1) Silicon Field Effect Transistor

In 1964, Howard and Fang [30] reported an investigation on characteristics of silicon field effect transistor at low temperature. The silicon devices were cooled to liquid helium temperature, and transconductance fluctuations were observed.

In 1981, Fowler *et al.* [31] measured the conductance in metal-oxide-silicon field-effect transistors. The conductance as a function of gate voltage was studied at different temperatures. Strong and reproducible fluctuations of conductance were observed as a function of the gate voltage.

In 1983, Skocpol *et al*. [32] measured the conductance as function of gate voltage and magnetic field in silicon inversion layers at 2K. The pronounced fluctuations of conductance were observed as a function of electron density.

In 1984, Kwasnick *et al*. [33] measured the conductance of metal-oxide-silicon field-effect transistors below 15K. A large variation of conductance can be observed when the temperature drops below 15K. It was also found that the fluctuation pattern can be changed if the temperature is temporarily raised to higher than 200K or the gate voltage is temporarily increased to higher than threshold. They felt that this indicated that the random potential induced by diffusion of ions and electrons affected the conductance fluctuation patterns.

In 1985, Skocpol *et al*. [34] studied quantum transport in narrow MOSFET channels as quasi-one-dimensional electron systems. The conductance fluctuations were measured for both gate voltage sweeps and magnetic field sweeps at low temperatures. There was a strong dependence of conductance on the gate voltage and magnetic field. The conductance fluctuations observed in the experiments had a dependence on the temperature.

In 1986, Kaplan and Hartstein [35] studied the conductance fluctuations in narrow silicon accumulation layers in a Silicon MOSFET. The gate voltage, magnetic field and orientation of the magnetic field were varied to measure their effect on the conductance. It was found that there was a dependence of fluctuations on the perpendicular component of the magnetic field, and the amplitudes of the conductance fluctuations for gate voltage sweeps and magnetic fields sweeps were roughly same. The rms values of the amplitude of the fluctuations agreed with the theoretical predictions given by Lee *et al*. [19]. It was

felt that the conductance fluctuations came from quantum interference in the sample devices.

In 1987, Skocpol [36] reported further measurements of the conductance fluctuations in narrow silicon MOSFETs at low temperature. The reproducible conductance fluctuations were measured at different magnetic fields and gate voltages. He found that the fluctuation pattern had continuous and random variations over different gate voltage and magnetic fields, but the rms value of the amplitude of fluctuations was close to e^2/h, which agreed with the theory of universal conductance fluctuations.

In 1988, Kaplan [37] studied the conductance in silicon metal-oxide-semiconductor field-effect transistors with sub-micron size. The conductance was measured for different source-drain voltage, gate voltage, and magnetic fields, at liquid-helium temperatures for small source-drain voltages. It was felt that these fluctuations of conductance came from quantum interference effects in the samples.

(2) GaAs 2DEG

In 1987, Thornton *et al*. [38] studied the conductance fluctuations in a GaAs/$Al_{0.3}Ga_{0.7}As$ heterojunction 2DEG for magnetic field sweeps below 4.2K. The measurements were taken at different values of temperatures. The results showed that the conductance fluctuated very slowly at a temperature of 4.2K, but the fluctuation amplitude became larger as the temperature was decreased. The dependence of phase coherence length on temperature was also studied.

In 1989, Debray *et al*. [39] reported conductance fluctuations in modulation-doped GaAs/AlGaAs heterojunction that were studied using magnetic field sweeps and Fermi energy sweeps at low temperature of 1.3K. It was assumed that the spin-orbit

scattering was negligible in such samples. It was observed that there was a reduction by a factor 4 below the theory for the variance of the amplitude of the conductance fluctuations. This effect was explained by the breaking of spin degeneracy from Zeeman splitting.

In 1991, Klepper *et al*. [40] studied the sensitivity of conductance fluctuations in GaAs/AlGaAs heterostructures to the addition of single elastic scatterers. The configuration of the scatterers was controlled by a photoionizing technique. A difference trace technique was used to study the changes in the fluctuations. The dependence of the rms values of the conductance fluctuations on temperature was determined. The results obtained in their experiments agreed with theory.

In 1993, Brown *et al*. [41] reported measurements of conductance fluctuations in GaAs 2DEG wires. The results obtained in their experiments showed a disagreement with the theory of universal conductance fluctuations at high magnetic fields. The violation was attributed to the extended electron diffusion near the boundaries as edge states began to form.

1.6 Conductance fluctuations in graphene

In this section, some recent developments in experimental or theoretical research on conductance fluctuations in graphene are summarized.

(1) Monolayer graphene

In 2006, Morozov *et al*. [42] reported an experimental study of the conductance fluctuations and weak localization in single layer graphene flakes. They found that the amplitude of the conductance fluctuations agreed with theory (in order of e^2/h), with no

evidence of spin-flip scattering. The fluctuations also showed no dependence on magnetic field at different temperatures. At low concentrations of Dirac fermions, the conductance fluctuations were absent and in a metallic regime, the fluctuations recovered.

In 2009, Horsell *et al*. [43] also studied the conductance fluctuations and weak localization in graphene devices for both Fermi energy sweeps and magnetic field sweeps. The results showed that the conductance fluctuations have a dependence on both elastic and inelastic scattering mechanisms. And, the conductance fluctuations are suppressed by strong inter-valley scattering. Both the variation of conductance fluctuations and weak localization has a dependence on temperature.

In 2010, Chen *et al*. [44] measured weak localization and conductance fluctuations in single layer graphene at 250 mK. The phase coherence lengths obtained from weak localization and the autocorrelation of conductance fluctuations were comparable. It was also observed that, when the carrier density decreased, there was a reduction of the amplitude of the conductance fluctuations, which was explained as a mechanism of loss of phase coherence.

In 2011, Freitag *et al.* [45] reported an investigation of conductance fluctuations in monolayer graphene devices which had superconducting Al contacts for source and drain. It was found that conductance fluctuations are enhanced by the superconducting contacts. They also found that the conductance fluctuations have a weak dependence on the gate voltage. At the charge neutrality point, the conductance fluctuations exhibited a dependence on the series resistance.

In 2012, Bohra *et al.* [46] reported research on the conductance fluctuations in graphene which involved varying the gate voltage and the magnetic field. They found

that the amplitude of conductance fluctuations for magnetic fields sweeps is smaller than that of the Fermi energy sweeps. It was also observed that the amplitudes of conductance fluctuations for varying gate voltage are different for perpendicular and parallel magnetic fields. The rms values of the conductance fluctuations for varying gate voltage was suppressed by perpendicular magnetic fields, but did not have significant dependence on the parallel magnetic fields. These experimental results showed a failure of ergodicity in graphene.

(2) Bilayer graphene

In 2010, Liao *et al*. [47] reported an experimental study of conductance fluctuations in a bilayer graphene system. The dependence of conductance fluctuations on temperature, magnetic field and bias current were examined in their work. It was observed that the rms value of the conductance fluctuations was in inverse proportion to the bias current. This dependence is explained by the confinement of the charge impurity scattering. They also measured the temperature-dependent conductance fluctuations and found the rms amplitude of fluctuations decreased when the temperature was increased.

(3) Trilayer graphene

In 2014, El-Bana *et al*. [48] reported results on conductance fluctuations and weak localization in trilayer graphene a field effect transistor. They varied the gate voltage, magnetic field and temperature. The layer number and quality of the graphene flake were determined by atomic force microscopy and Raman spectroscopy. A weak localization correction of the conductance was observed. It was also found that aperiodic conductance fluctuations as a function of gate voltage showed an amplitude of e^2/h. This feature was explained using the interference of discrete carrier trajectories.

(4) Multilayer graphene

In 2010, Trbovic *et al*. [49] reported an investigation of the conductance fluctuations in few-layer graphene. The graphene flakes had two superconducting contacts of Ti/Al. Conductance fluctuations were observed when the gate voltage was swept. There was also a dependence of the conductance fluctuations on the source-drain voltage and the temperature. When the temperature was increased, the amplitude of the conductance fluctuations decreased. At zero bias and 230mK, the amplitude of the conductance fluctuations was of order of e^2/h.

In 2013, Chuang *et al*. [50] reported using multi-layer graphene flakes to study the magneto-conductance fluctuations. The dependence of the dephasing time on the temperature was examined. The results showed that the layers in the center can provide better transport properties, since the substrate impurities and the air molecules had less effect on the layers in the center. The multi-layer graphene had a shorter low-temperature saturation of dephasing time than the monolayer graphene.

1.7 Research objectives and thesis structure

Based on the historical review of the research work on conductance fluctuations in metals, semiconductor materials and graphene during the past few decades, whether the universality and hypothesis of ergodicity hold in semiconductors and graphene is still an open question. Thus, my thesis work aims to numerically investigate the characteristics of conductance fluctuations in GaAs nanowires and graphene nanoribbons at zero temperature to examine the universality and hypothesis of ergodicity in these two nanostructures.

Chapter 2 introduces the calculations of conductance fluctuations in GaAs nanowires using the finite difference method. Conductance fluctuations in Fermi energy sweeps and magnetic field sweeps are investigated in the presence of a disorder potential.

Chapter 3 focuses on the effect of magnetic field on the conductance fluctuations for Fermi energy sweeps in GaAs nanowires, since the formation of edge states under magnetic field will suppress the amplitude of conductance fluctuations.

Chapter 4 turns to the study of graphene nanoribbons. The building of the Hamiltonian for graphene nanoribbons with armchair edges, the incorporation of a magnetic field, and how to integrate the Hamiltonian into the transfer matrix equation will be presented.

Chapter 5 shows the results of conductance fluctuations in graphene nanoribbons in the presence of short-range disorder. The fluctuations are calculated as a function of Fermi energy and magnetic field. The rms values of the amplitudes of the fluctuations are also calculated for different random potential amplitudes.

Chapter 6 presents the conductance fluctuations in graphene nanoribbons due to remote charge long-range disorder. The building of the long-range impurity model is described in detail. I focus on the effect of magnetic field on the conductance fluctuations for Fermi energy sweeps and calculate the root-mean-square value of fluctuation amplitudes of Fermi energy sweeps at different magnetic fields.

Chapter 7 summarizes the conclusions of each chapter. The merit and issues of the thesis work will be discussed and suggestions for future research will be given.

CHAPTER 2

CONDUCTANCE FLUCTUATIONS IN GAAS NANOWIRES

2.1 Introduction

In this chapter, the conductance fluctuations in GaAs nanowires are studied using the finite difference approach. The 2D Schrödinger equation which describes the quantum states in GaAs 2DEG is discretized and mapped onto a rectangular finite difference lattice. Then the discretized Schrödinger equation can be converted into the transfer matrix equation. I use the recursive scattering matrix methods to solve the transfer equation and then the transmission matrix can be reached [51]. After this point, the conductance can be computed utilizing the Landauer-Büttiker formula. Meanwhile, the perpendicular magnetic field is incorporated into the calculation by inserting the Peierls phase factor to the hopping energy terms. I use the disorder potential to calculate the fluctuations for Fermi energy sweeps and magnetic field sweeps under different amplitudes of disorder potential. δG as function of the Fermi energy and magnetic field can be obtained by subtraction of the polynomial fit values from the original fluctuations. The root-mean-square values of δG can be found then [51].

This chapter is organized as follows. In section 2.2, the computational approach is introduced. The results of conductance of GaAs nanowires without disorder are shown in section 2.3. Section 2.4 gives the results of conductance of GaAs nanowires under disorder potential and the calculations of δG for Fermi energy sweeps and magnetic field sweeps are done in section 2.5. Finally, in section 2.6, the results of δG for different random potential amplitudes are presented and conclusions are also discussed here.

2.2 Computational techniques

The states of electrons in GaAs 2DEG are described by 2D Schrödinger equation [17]

$$-\frac{\hbar^2}{2m^*}\left(\frac{d^2}{dx^2}+\frac{d^2}{dy^2}\right)\Psi(x,y)+V(x,y)\Psi(x,y)=E\Psi(x,y). \tag{2.1}$$

By mapping the simulation domain onto a rectangular finite difference lattice with grid size of a shown in Fig. 2.1(a), I get the discrete form of the 2D Schrödinger equation as

$$-t\left(\Psi_{i+1,j}+\Psi_{i-1,j}+\Psi_{i,j+1}+\Psi_{i,j-1}\right)+\left(V_{i,j}+4t\right)\Psi_{i,j}=E\Psi_{i,j}, \tag{2.2}$$

in which, $\Psi_{i,j}$ is the wave function and $V_{i,j}$ is the potential at the site (i,j). Here $t=\frac{\hbar^2}{2m^*a^2}$ and $\hbar$ is the reduced Planck's constant [51].

The discrete Schrödinger equation can be converted to a matrix form

$$H_{0i}\vec{\Psi}_i-t\vec{\Psi}_{i+1}-t\vec{\Psi}_{i-1}=EI\vec{\Psi}_i, \tag{2.3}$$

in which

$$H_{0i}=\begin{bmatrix} \left(V_{i,M}+4t\right) & -t & 0 & \cdots & & & \\ -t & \left(V_{i,M-1}+4t\right) & -t & \cdots & & & \\ & & & \ddots & & & \\ & & & \cdots & -t & \left(V_{i,2}+4t\right) & -t \\ & & & \cdots & 0 & -t & \left(V_{i,1}+4t\right) \end{bmatrix}. \tag{2.4}$$

Here the term t can be explained as the perturbation on the slice Hamiltonian. Then, the transfer-matrix equation which represents the relationship between adjacent slices can be obtained as

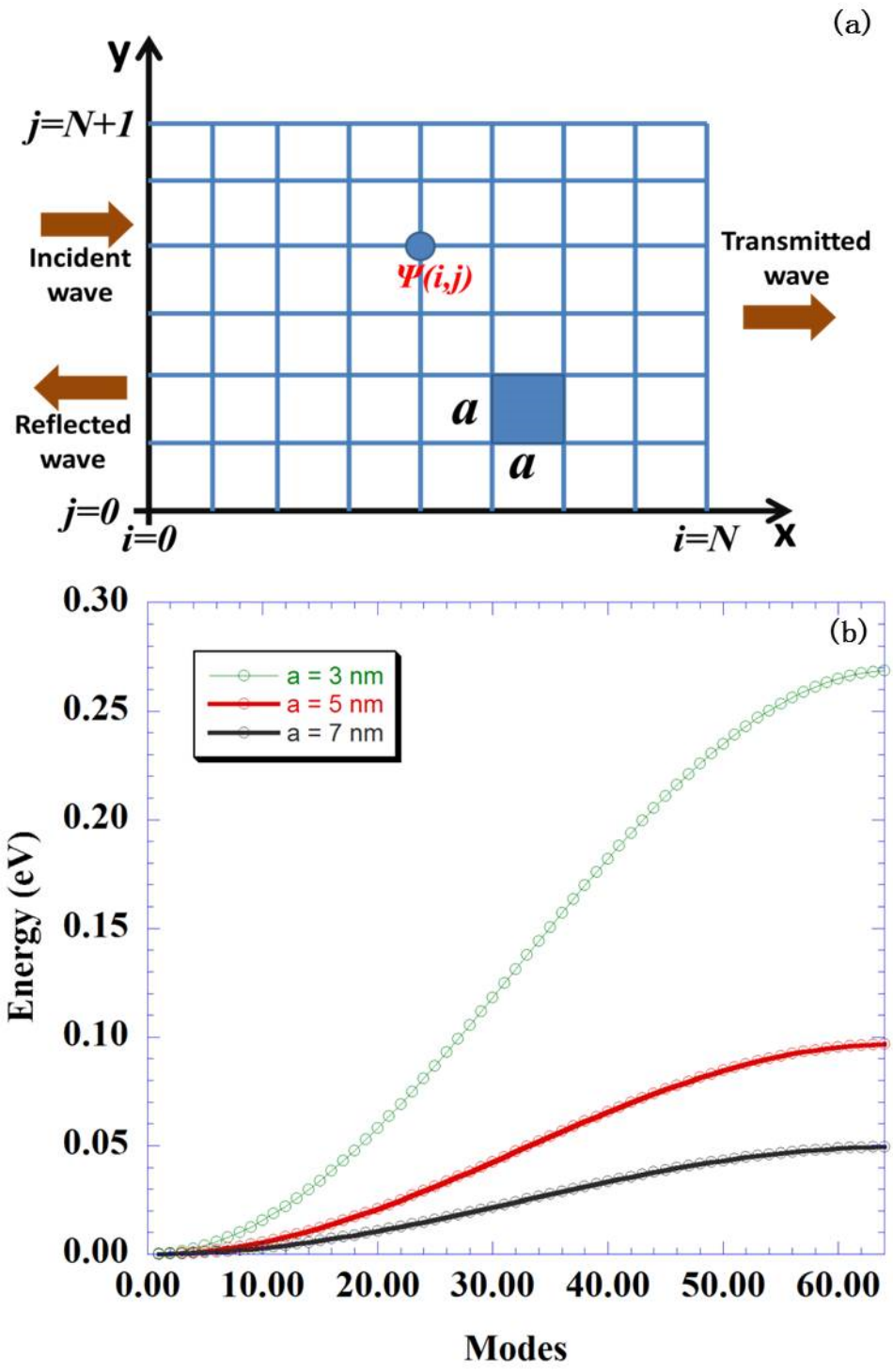

Fig. 2.1 (a) Finite difference grids for discretization of 2D Schrödinger equation. (b) Artificial energy band that arises from the discretized lattice used for simulations for grid size of 3nm, 5nm and 7nm. A quasi-linear energy region can be found in the middle of band.

$$\begin{bmatrix} \psi_i \\ \psi_{i+1} \end{bmatrix} = \begin{bmatrix} 0 & I \\ -I & \dfrac{H_{0i} - E}{t} \end{bmatrix} \begin{bmatrix} \psi_{i-1} \\ \psi_i \end{bmatrix} = T_i \begin{bmatrix} \psi_{i-1} \\ \psi_i \end{bmatrix}. \tag{2.5}$$

I solve the transfer matrix equation in the zeroth slice and the solution will be in the form

$$\begin{bmatrix} u_m(\pm) \\ \lambda_m(\pm) u_m(\pm) \end{bmatrix}. \tag{2.6}$$

The sign$(\pm)$ here means the direction of the modes and $(+)$ means propagating to the right and $(-)$ means propagating to the left. The transfer matrix equation for N slices has the form

$$\begin{bmatrix} t \\ 0 \end{bmatrix} = T_0^{-1} T_N T_{N-1} \ldots T_1 T_0 \begin{bmatrix} I \\ r \end{bmatrix}. \tag{2.7}$$

The problem of Eq. (2.7) is that it cannot be solved due to its numerical instability. One solution developed by Usuki *et al.* [52] is to convert it to an iterative scheme based on the scattering matrix as

$$\begin{bmatrix} C_1^{l+1} & C_2^{l+1} \\ 0 & I \end{bmatrix} = T_l \begin{bmatrix} C_1^l & C_2^l \\ 0 & I \end{bmatrix} \begin{bmatrix} I & 0 \\ P_{l1} & P_{l2} \end{bmatrix}, \tag{2.8}$$

with $P_{l1} = -P_{l2} T_{l21} C_1^l$ and $P_{l2} = \left(T_{l21} C_2^l + T_{l22} \right)^{-1}$ [17, 51, 53].

Starting with $C_1^0 = I$ and $C_2^0 = 0$, the final transmission matrix t is obtained as

$$t = -\left(U^+ \lambda^+ \right)^{-1} \left[C_2^{N+1} - U^+ \left(U^+ \lambda^+ \right)^{-1} \right]^{-1} C_1^{N+1}. \tag{2.9}$$

Here, P_{l1} and P_{l2} can be used to calculate the electron density by back propagating the wave function from right to left. Finally, the electron density at each site can be calculated using

$$n(x,y) = n(i,j) = \sum_{k=1}^{q} \left| \psi_{ijk} \right|^2 . \tag{2.10}$$

The incorporation of a perpendicular magnetic field can be realized by insertion of the Peierls phase into the 2D Schrödinger equation in the form

$$H_{0i}\vec{\Psi}_i - t_{R,i}\vec{\Psi}_{i+1} - t_{L,i}\vec{\Psi}_{i-1} = EI\vec{\Psi}_i , \tag{2.11}$$

in which $t_{R,i,j} = e^{i\theta_{R,i,j}} t\delta_{i,j}$, $t_{L,i,j} = e^{i\theta_{L,i,j}} t\delta_{i,j}$ and $\theta_{L,i,j} = \theta_{R,i,j} = -2\pi eBa^2/h$ [52]. The conductance G then can be calculated using the Landauer-Büttiker formula

$$G = \frac{2e^2}{h} \sum_{m,n} \frac{v_n}{v_m} \left| t_{n,m} \right|^2 . \tag{2.12}$$

Here, v_m and v_n are velocity of the two modes [17, 51, 52].

I begin by calculating the eigenvalues of the discretized 1D wave Schrödinger function $-\frac{\hbar^2}{2m^*}\frac{d^2}{dx^2}\Psi(x,y) = E\Psi(x)$ for the zeroth slice in the simulation domain. The eigenvalues of the equation with grid size of 3nm, 5nm and 7nm are plotted in Fig. 2.1(b). The hopping energies for each size are 67.2meV, 24.2meV and 12.3eV, respectively. These are obtained from $t_{hop} = \frac{\hbar^2}{2m^*}\frac{1}{a^2}\frac{1}{e}(eV)$. In the band structure for grid size of 5nm, I use the parabolic band in the regime from 5meV to 20meV and a quasi-linear band between 30meV and 60meV to study the conductance fluctuations in the following sections. Since there is also a linear dispersion spectrum at low energy in the graphene band structure, the artificial quasi-linear band here in GaAs helps to study the conductance fluctuations related to a linear band [46, 54].

2.3 Conductance of GaAs nanowire

In this investigation, several samples of GaAs 2DEG nanowires with different sizes are studied. I calculate the conductance of the GaAs 2DEG nanowire for both a Fermi energy sweep and a magnetic field sweep. The conductance in parabolic band and quasi-linear band are both considered [51].

Figure 2.2 (a) shows the conductance for a Fermi energy sweep in the parabolic band over the range 5meV to 25meV, for a GaAs nanowire with a width of 29 cells and a length of 39 cells, at different perpendicular magnetic fields of 0T, 0.5T, and 1T. The depopulation of modes due to magnetic field increment can be observed. Fig. 2.2 (b) shows the conductance of a Fermi energy sweep in the quasi-linear band from 30meV to 60meV for a GaAs nanowire, with a width of 29 cells and a length of 39 cells at perpendicular magnetic fields of 0T, 0.5T, and 1T. There are more modes propagating in the wire since the Fermi energy in the quasi-linear band is higher than the energy in a parabolic band.

Results of magnetic field sweeps are presented in Fig. 2.3. The conductance as function of magnetic field is plotted in Fig. 2.3(a) at Fermi energies of 5meV, 15meV and 25meV, in a parabolic band for a GaAs nanowire with a width of 29 cells and a length of 39 cells. The conductance as function of the magnetic field is plotted in Fig. 2.3(b) for a quasi-linear band at Fermi energies of 30meV, 45meV, and 60meV, for a GaAs nanowire with width of 29 cells and length of 39 cells. The number of modes clearly is reduced as the magnetic field increases from 0T to 2T.

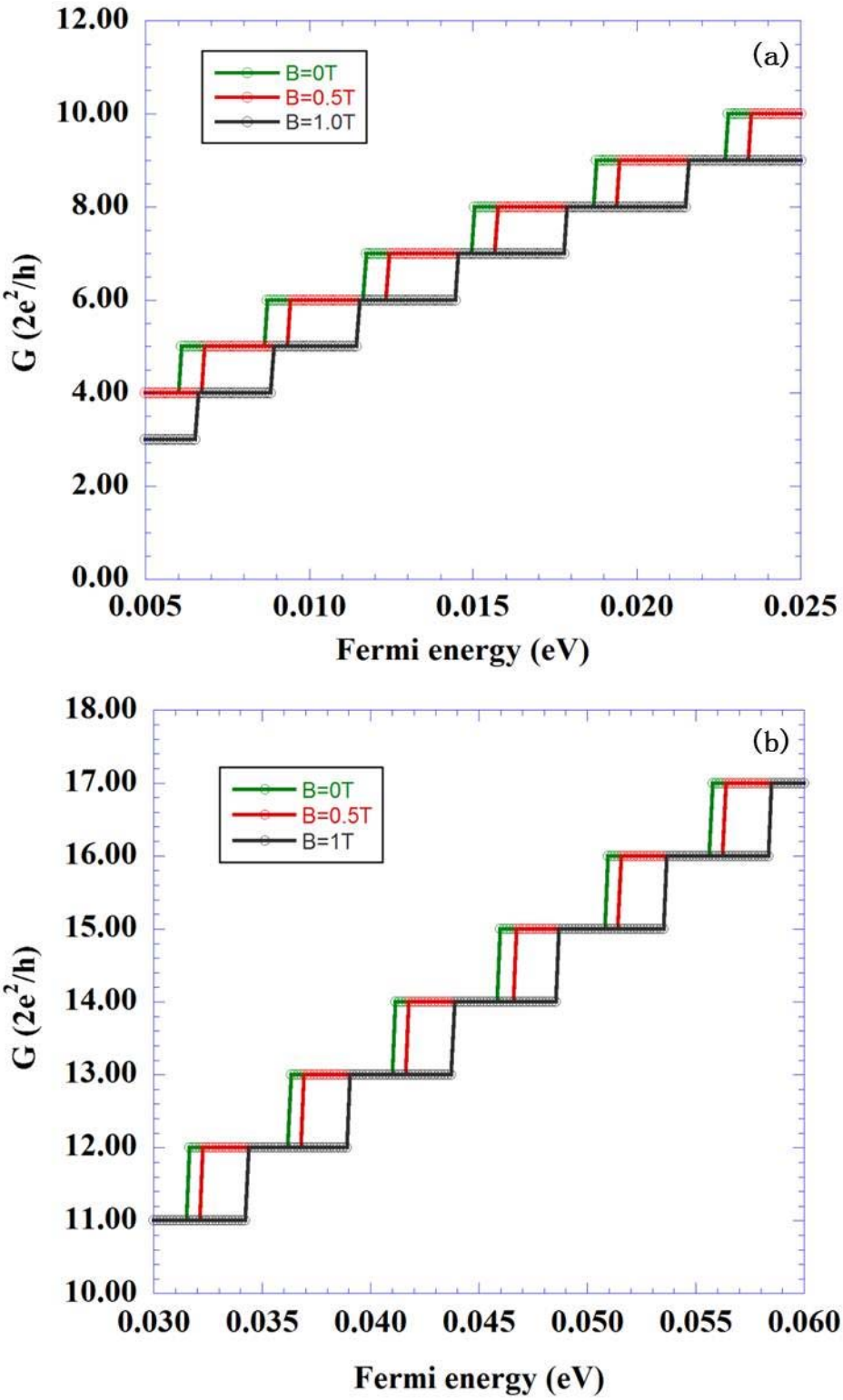

Fig. 2.2 Conductance of GaAs nanowire for Fermi energy sweeps in (a) parabolic band and (b) quasi-linear band at a magnetic field of 0T, 0.5T and 1T.

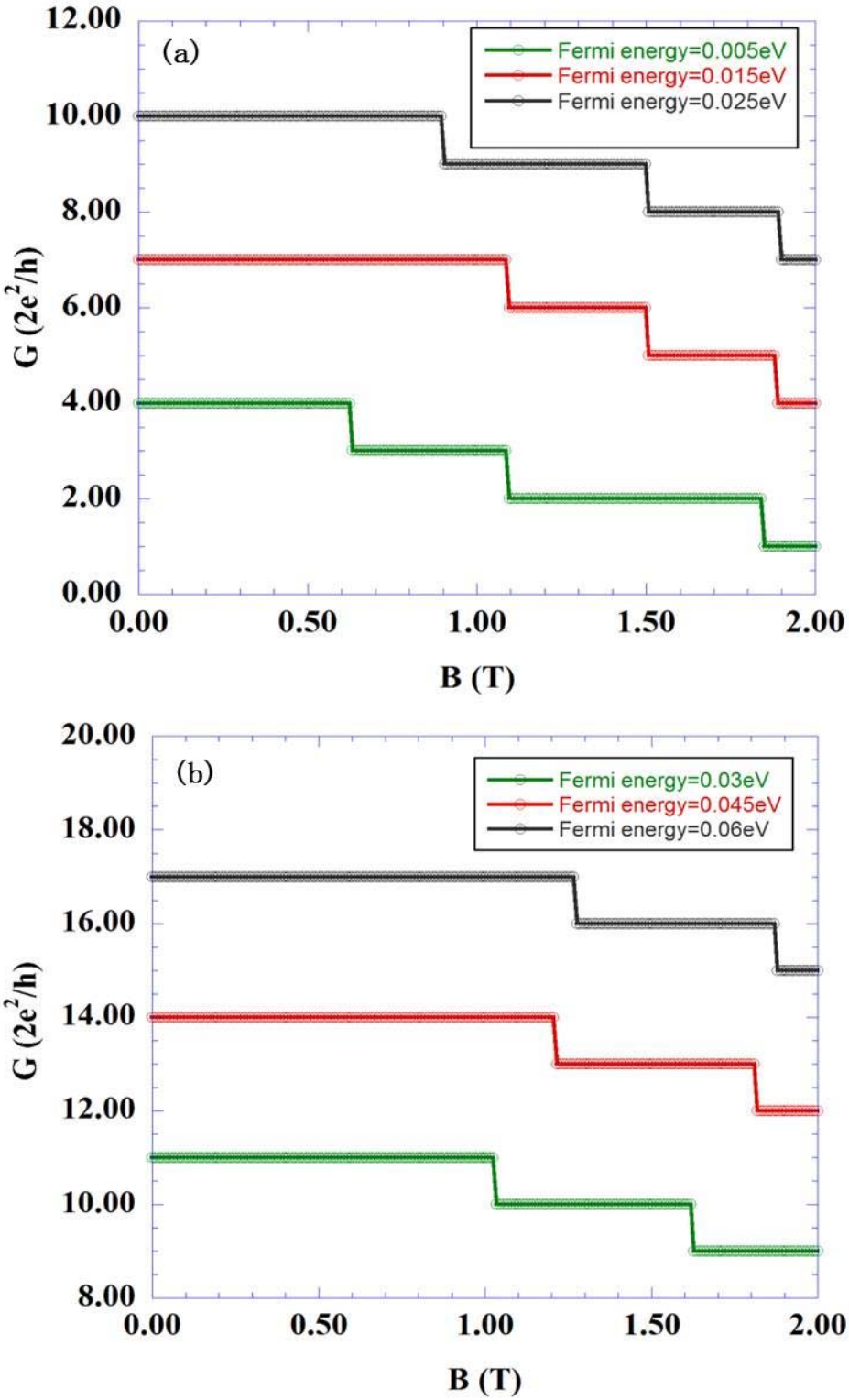

Fig. 2.3 Conductance of GaAs nanowire for magnetic field sweeps in (a) parabolic band at a Fermi energy of 5, 15 and 25meV, and (b) a quasi-linear band at Fermi energies of 30, 45 and 60meV.

2.4 Conductance fluctuations of GaAs nanowire

The conductance fluctuations can be calculated by introducing a random disorder potential based on the Anderson model [55]. In Fig.2.4 (a), I show the finite difference grids in the simulation domain. The random potential is created on each grid point, and an example of the disorder potential is given in Fig.2.4 (b) for the nanowire in panel (a). Since the cell size is 5nm×5nm, the area of the nanowire is 3×10^{-10} cm^{-2} and there are around 1200 grid points, so the density of impurities is around 4.0×10^{12} cm^{-2}. The peak-to-peak value of the random disorder potential is twice the hopping energy (24.2 meV), or 48.4 meV here.

I vary the amplitude of the disorder potential with multipliers from the set [0.1, 0.2, 0.5, 1.0, 1.5, 2.0, 3.0] × 24.2 meV, and calculate the conductance fluctuations in GaAs nanowires of various sizes. Fig. 2.5 shows the conductance for Fermi energy sweeps for the grid of Fig. 2.4 (a). Panel (a) presents the conductance in a parabolic band, while panel (b) shows the conductance in a quasi-linear band. When the amplitude of the disorder potential increases, it can be observed from the plots that the amplitude of fluctuations in the conductance get larger and the steps (as modes are added) are gradually masked by the random potential after the peak-to-peak amplitude of the random potential exceeds 0.5×24.2 meV. Fig. 2.6 presents conductance for magnetic field sweeps under the same set of potential for the device. Fig. 2.6 (a) is the conductance at a Fermi energy of 15meV in a parabolic band while Fig. 2.6 (b) is the conductance at a Fermi energy of 45meV in the quasi-linear band. The magnetic field sweep is from 0T to 2T in each case.

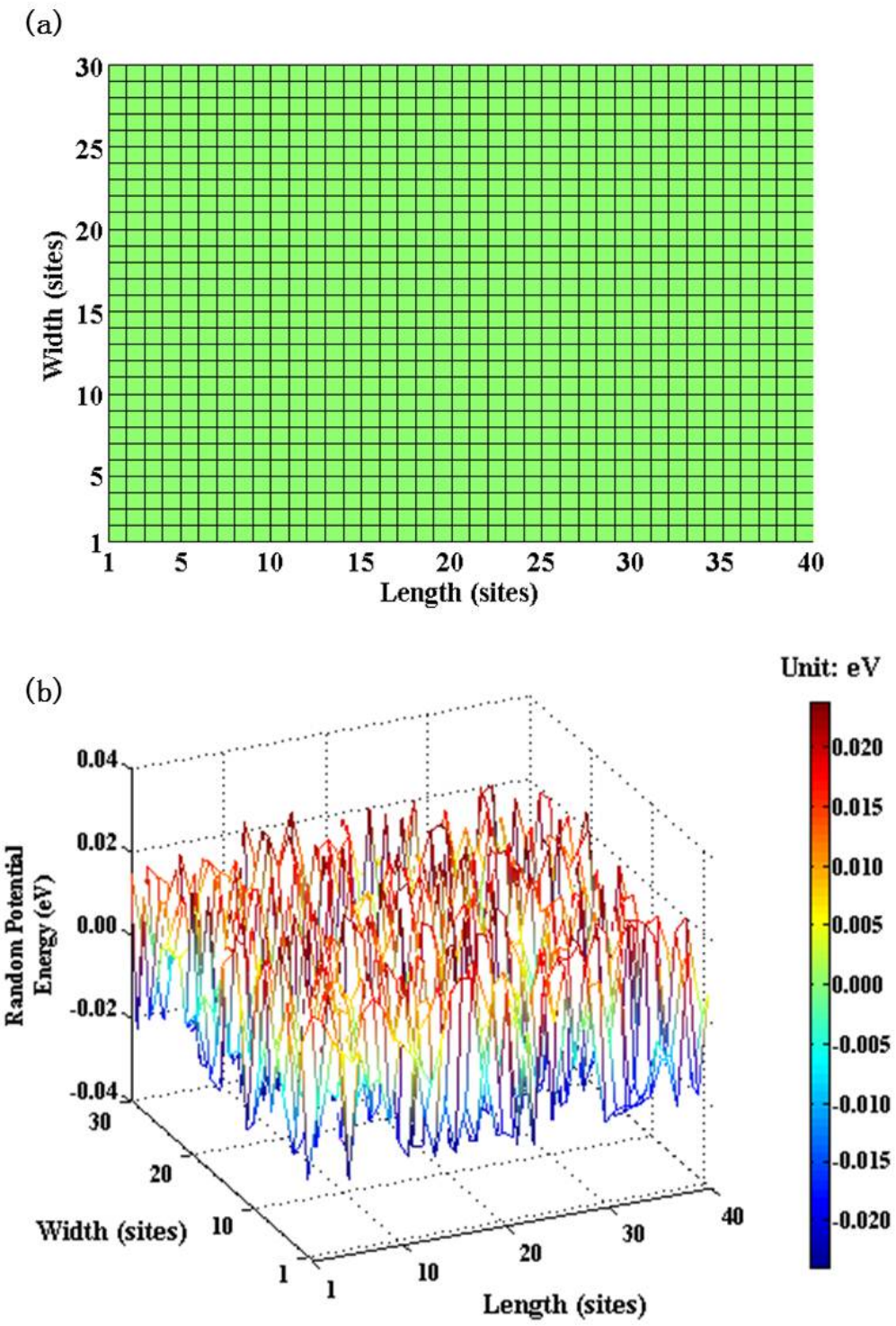

Fig. 2.4 (a) Finite difference grid of a GaAs nanowire with size of 39×29 cells, where the length of each cell is 5nm. (b) The random disorder potential energy in the GaAs nanowire with peak-to-peak value of 2.0×24.2meV.

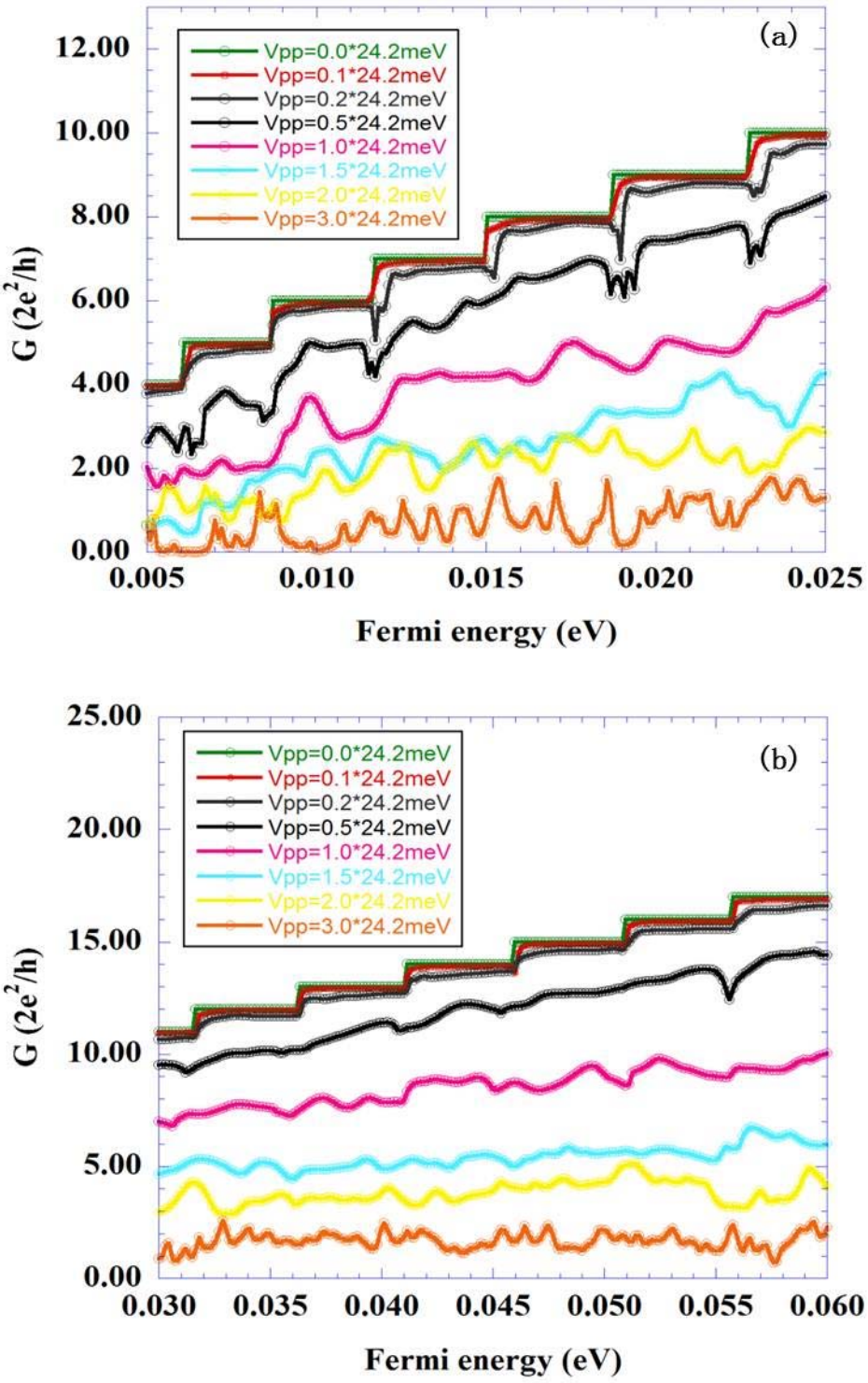

Fig. 2.5 Conductance for Fermi energy sweeps for (a) a parabolic band and (b) a quasi-linear band, for different random potential amplitude from 0.1×24.2meV to 3.0×24.2meV.

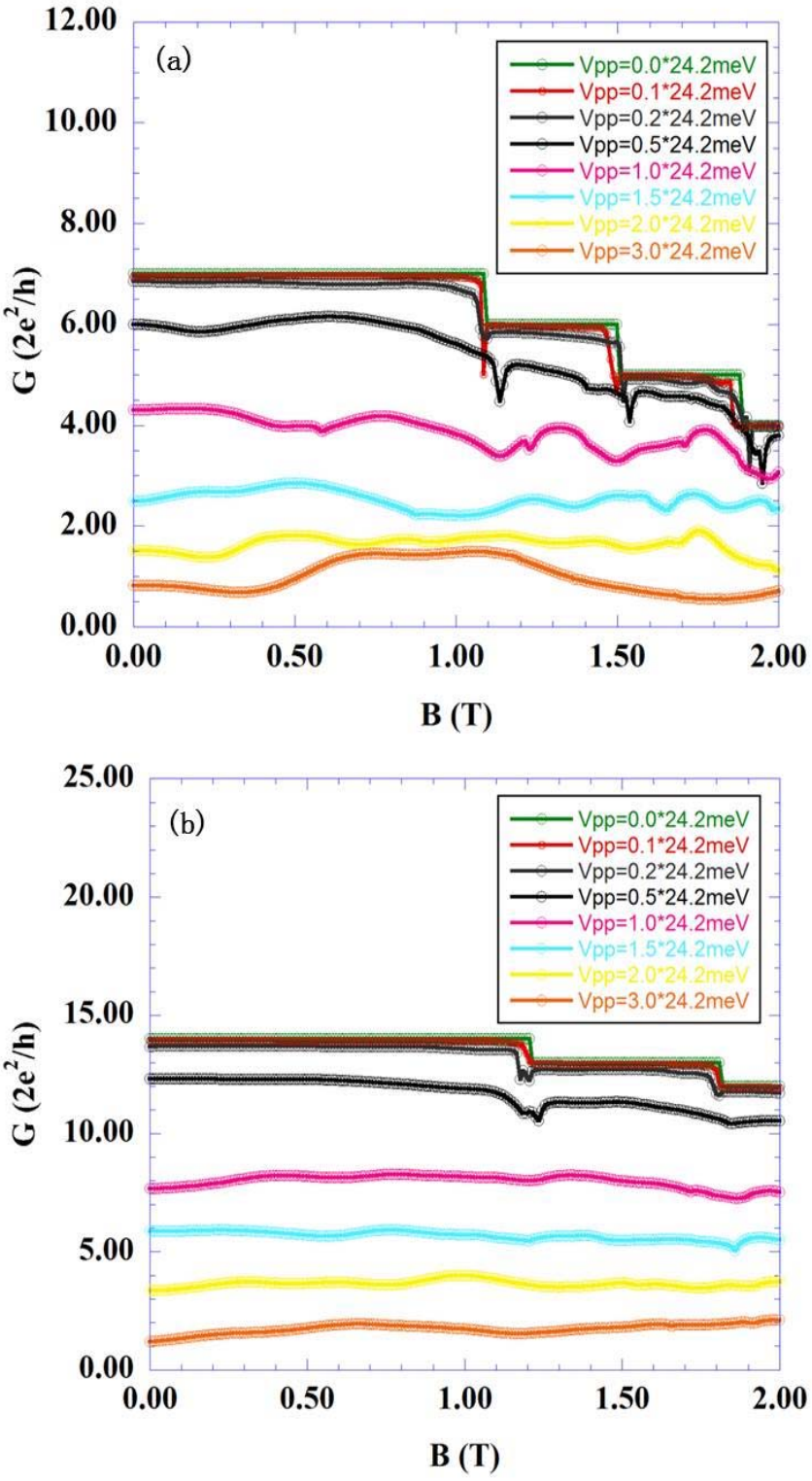

Fig. 2.6 Conductance for magnetic field sweeps for (a) a parabolic band, and (b) a quasi-linear band, for different random potential amplitude from 0.1×24.2meV to 3.0×24.2meV.

2.5 δG vs Fermi energy and magnetic field

I use a polynomial fit to each curve in Figs 2.5 and 2.6 to get the background value of conductance. This is subtracted from the conductance to determine the δG values. The values of δG for a Fermi energy sweep in the parabolic band from 5meV to 25meV are in Fig. 2.7 (a) and results from a quasi-linear band from 30meV to 60meV are in Fig. 2.7 (b). The peak-to-peak amplitude of the random potential here is 2.0×24.2 meV. The value of δG as a function of magnetic field is given in Fig. 2.8. Panel (a) is the plot of δG for a magnetic field sweep in a parabolic band, at a Fermi energy of 15meV, and panel (b) is the plot of δG for a magnetic field sweep in a quasi-linear band at a Fermi energy of 45meV. The peak-to-peak amplitude of the random potential for the magnetic field sweep is also 2.0×24.2 meV. By comparing the amplitudes of δG for a Fermi energy sweep and a magnetic field sweep, it is obvious that the amplitude of δG for the magnetic field sweep is smaller than the amplitude of δG for the Fermi energy sweep, at the same random potential amplitude of 2.0×24.2 meV.

To evaluate the conductance fluctuation obtained above, I also calculate the correlation functions of the conductance fluctuation for both Fermi energy sweep and magnetic field sweep. One typical example in a parabolic band, for random potential amplitude of 0.5×24.2 meV in a nanowire with size of 65×165 cells, is given in Fig. 2.9. Panel (a) is the correlation function for a Fermi energy sweep and panel (b) is the correlation function for a magnetic field sweep. The correlation length ΔE_c and ΔB_c are defined to be the point where the correlation function reduces to one-half of its initial values [51].

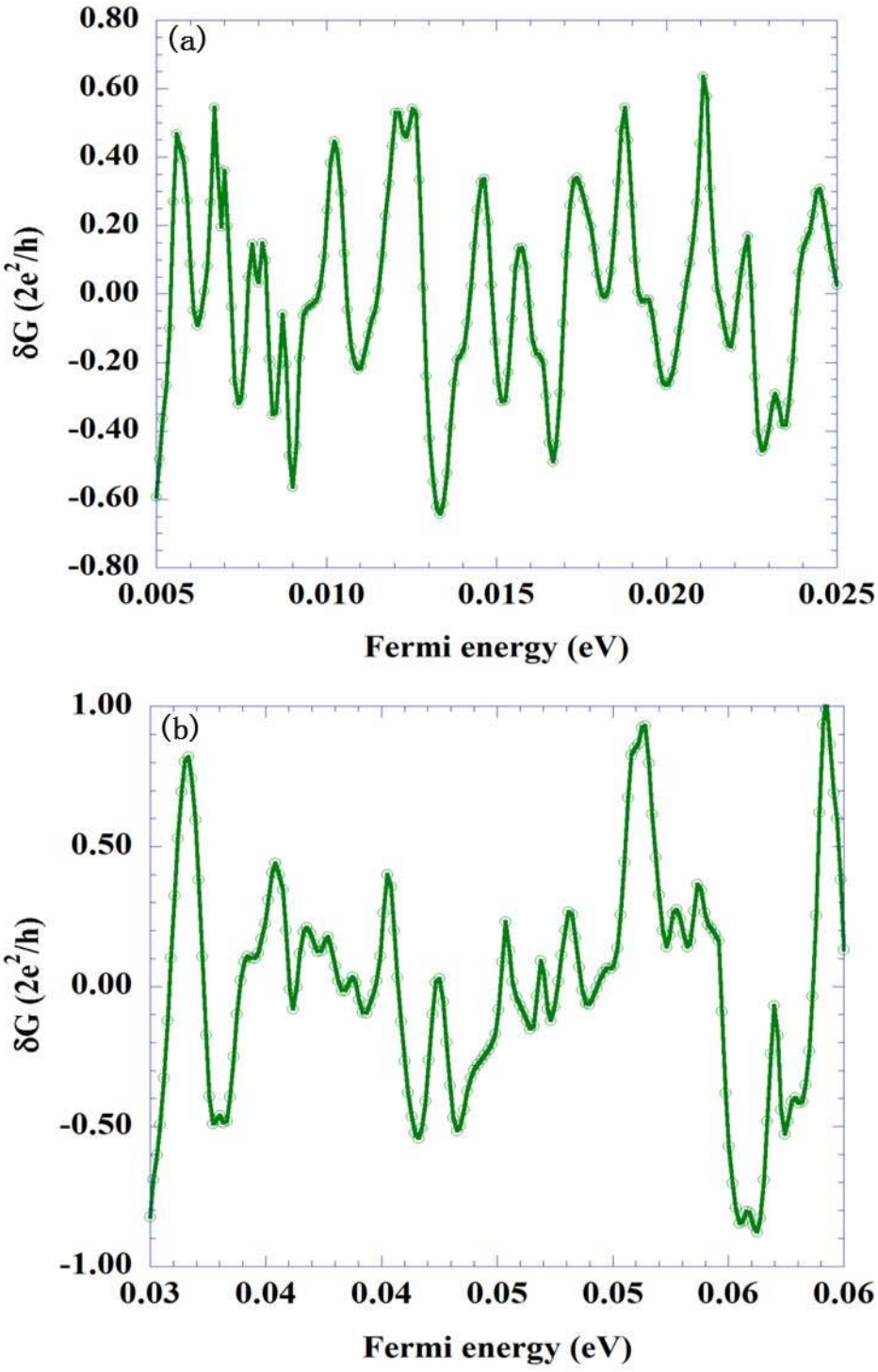

Fig. 2.7 δG of a Fermi energy sweep in (a) a parabolic band from 5meV to 25meV and (b) a quasi-linear band from 30meV to 60meV, at random potential amplitude of 2.0×24.2meV (peak-to-peak value).

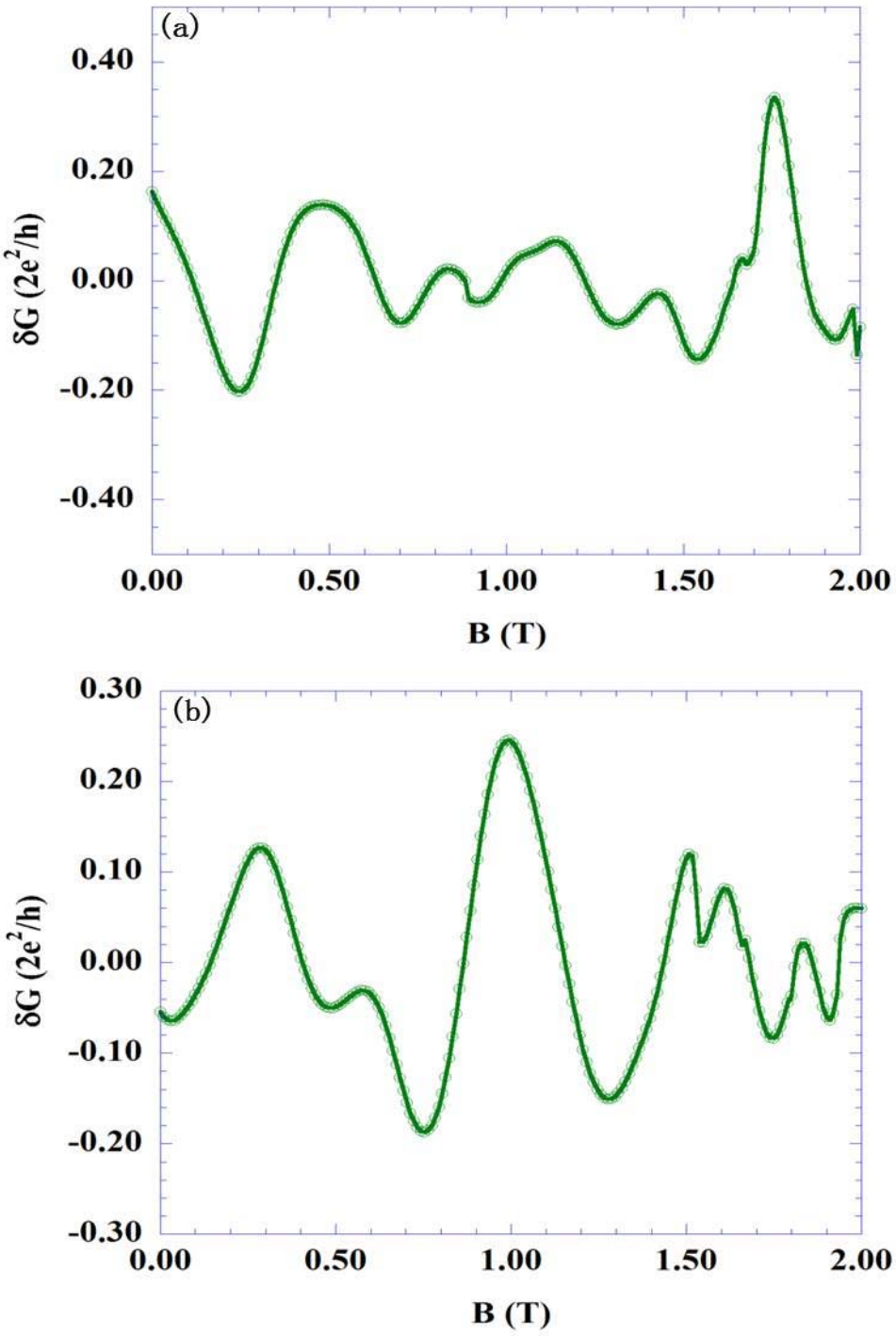

Fig. 2.8 δG for a magnetic field sweep in (a) a parabolic band, at a Fermi energy of 15meV, and (b) a quasi-linear band, at a Fermi energy of 45meV, for random potential amplitude of 2.0×24.2meV (peak-to-peak value).

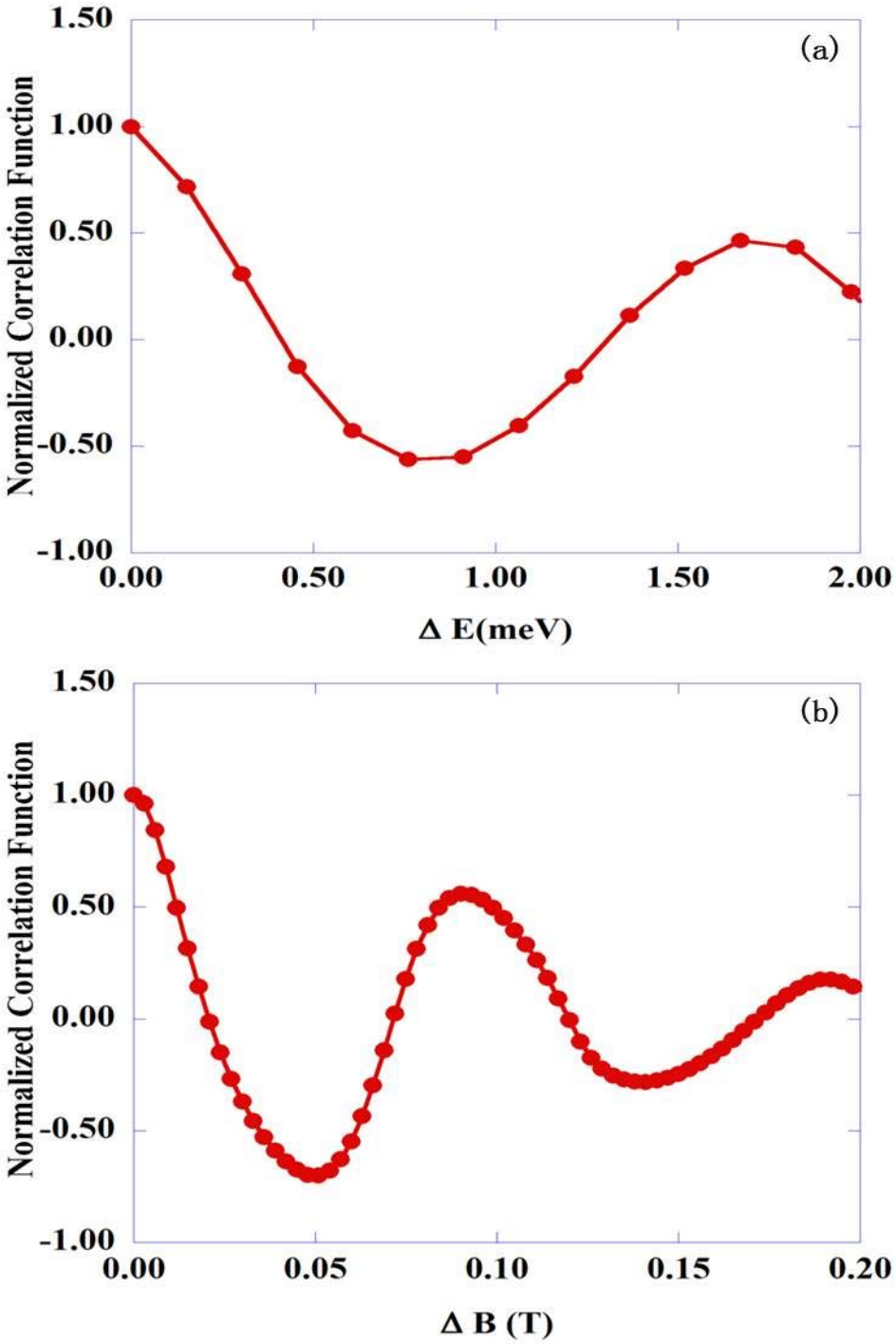

Fig. 2.9 Correlation functions in a parabolic band for a random potential amplitude of 0.5×24.2meV in a nanowire with size of 65×165 cells for (a) a Fermi energy sweep at B=0T and (b) a magnetic field sweep at a Fermi energy of 15meV.

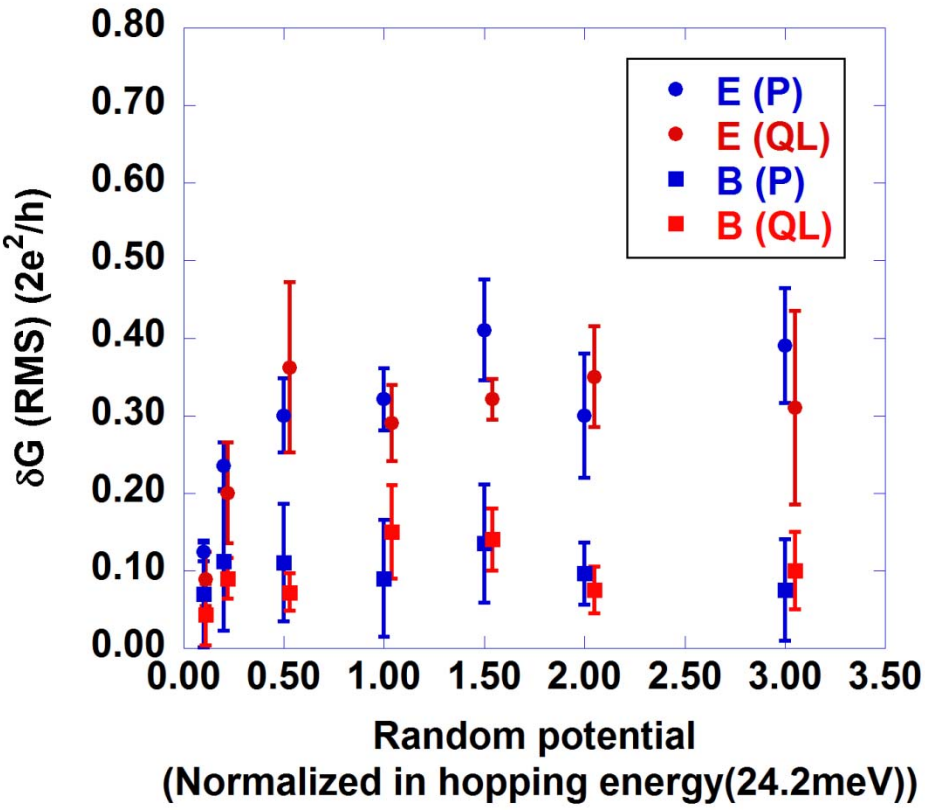

Fig. 2.10 The root-mean-square values of δG for Fermi energy sweeps (filled circles) and magnetic field sweeps (filled squares) in a parabolic band (blue color) and a quasi-linear band (red color). These values are averaged over many samples with many different sizes.

2.6 Conclusions

The conductance fluctuations are calculated using many samples with different sizes. The root-mean-square values of δG as function of the peak-to-peak amplitudes of the random potential are all collected together in Fig. 2.10. Here, the magnetic field sweeps are indicated by filled squares with blue colors for the parabolic band results and red colors for the quasi-linear band results. The Fermi energy sweeps are shown by filled circles with blue colors for the parabolic band results and red colors for the quasi-linear band results. Within the statistical errors, there are no significant differences between results from the parabolic band and the quasi-linear band. When the amplitude of the

random potential increases, the RMS value of δG increases to a maximum value of about 0.35 for the Fermi energy sweeps and about 0.15 for the magnetic field sweeps. The magnetic field sweep results are approximately 3 times smaller than the Fermi energy sweep results when the peak-to-peak values of the random potential energies are larger than 1.0 × 24.2 meV. The features of δG(RMS) for conductance fluctuations summarized in Fig. 2.10 indicate that the hypothesis of ergodicity does not hold in GaAs nanowires [18, 19].

CHAPTER 3

EFFECT OF MAGNETIC FIELD ON CONDUCTANCE FLUCTUATIONS IN GAAS NANOWIRES

3.1 Introduction

Since the formation of edge states in GaAs 2DEG due to perpendicular magnetic fields will change the electron wave interference patterns, so the characteristics of conductance fluctuations for Fermi energy sweeps may show new features when the magnetic field is increased [46]. In this chapter, I investigate the effect of a perpendicular magnetic field on the amplitude of the conductance fluctuations for Fermi energy sweeps within the GaAs nanowires [51].

The Fermi energy sweeps run from 5meV to 25meV and at magnetic fields from 0T to 5T. The step size of magnetic field increment is as small as 0.025T, so we can examine the details of variation of fluctuation amplitudes for Fermi energy sweeps at each value of magnetic field. The size of the GaAs samples used in the calculation is 145 nm (width) × 195 nm (length). Here, a 5 nm grid is used for the finite difference cells. I consider two different peak-to-peak values of amplitudes of random potential energy that are 0.5×24.2meV (hopping energy) and 2.0 ×24.2meV (hopping energy).

This chapter is organized as follows. The calculation of conductance for Fermi energy sweeps at magnetic field from 0T to 5T for peak-to-peak values of random potential of 0.5×24.2meV (hopping energy) is given in section 3.2. The conductance fluctuations of Fermi energy sweeps for different magnetic fields for peak-to-peak values of random potential of 2.0 × 24.2meV (hopping energy) is given in section 3.3. And the conclusion will be discussed in section 3.4.

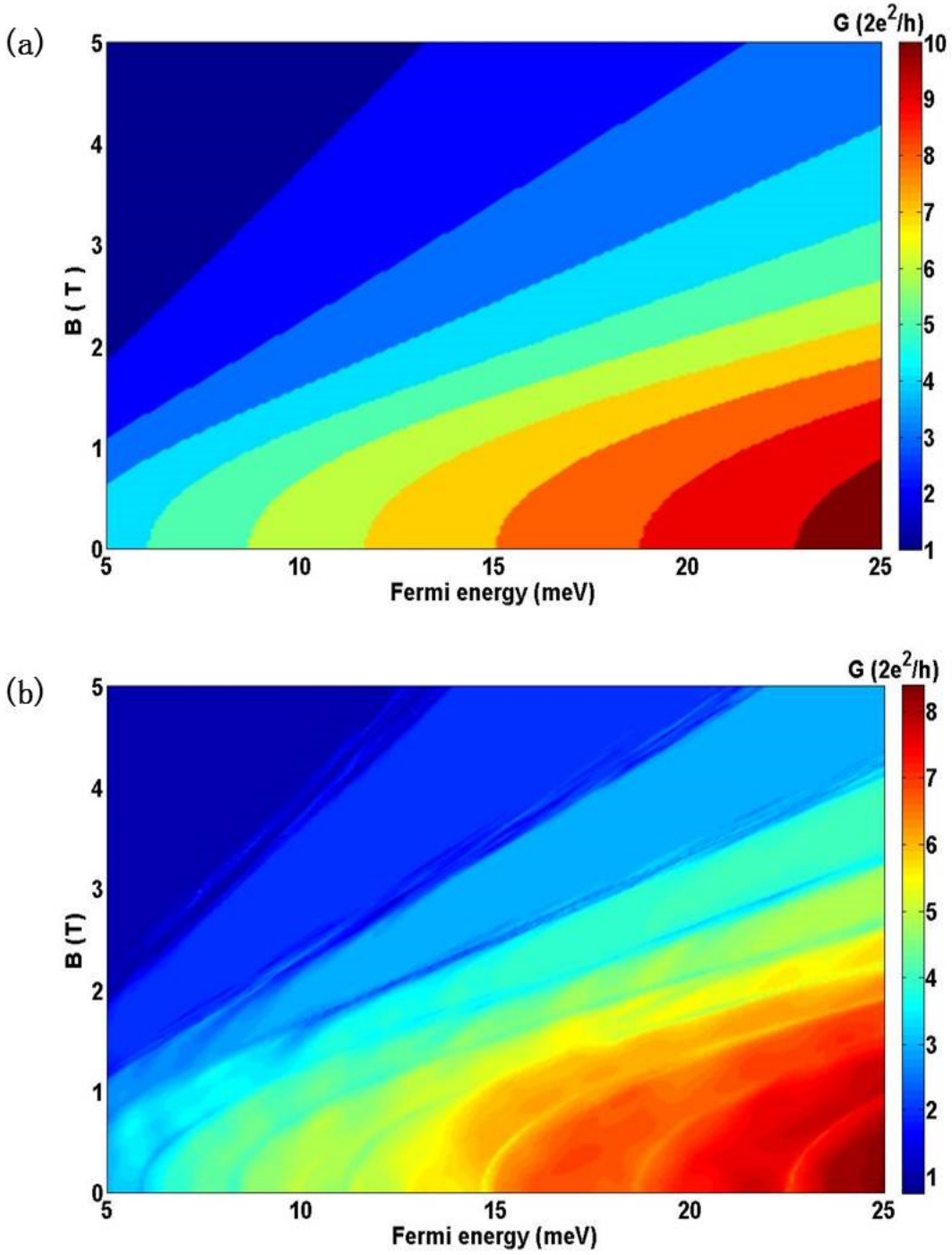

Fig. 3.1 Plots of conductance as a function of Fermi energies and magnetic fields for GaAs nanowires with size of 30 sites × 40 sites. (a) Peak-to-peak value of random potential energy is zero, (b) Peak-to-peak value of random potential energy is 12.1 meV.

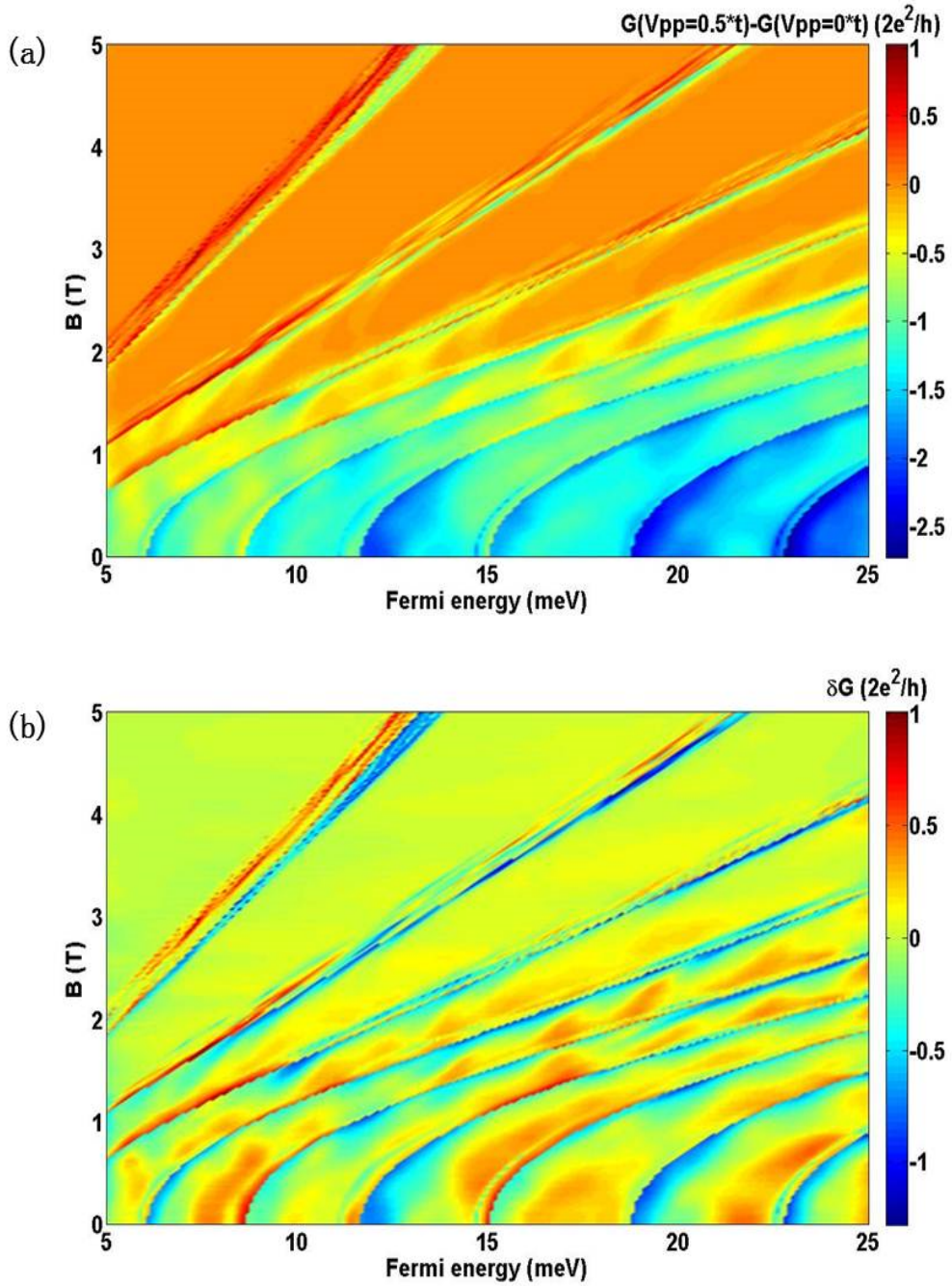

Fig. 3.2 (a) Plot of the conductance (random potential V_{pp} = 12.1 meV) after a background smooth fit is (for no random potential) subtracted as a function of Fermi energy and magnetic field for GaAs nanowires with size of 30 sites × 40 sites. (b) Plot of δG (random potential V_{pp} = 12.1 meV) after a polynomial fit is subtracted as a function of Fermi energy and magnetic field for GaAs nanowires with size of 30 sites × 40 sites.

3.2 Conductance fluctuations for weak disorder

At first, I calculate the conductance of Fermi energy sweeps from 5meV to 25meV for different magnetic field, ranging from 0T to 5T, without a disorder potential. These results are given in Fig. 3.1(a). It is clear that the conductance increases with Fermi energy, but at a fixed Fermi energy, the conductance drops as transverse modes are depopulated as the magnetic field gets larger. When a weak disorder potential is added, where the peak-to-peak value is 12.1 meV, the conductance begins to show fluctuations. This is shown in Fig. 3.1(b) as function of Fermi energy and magnetic field. This shows that the fluctuations mainly arise, for this low level, as the conductance increases at a mode transition. To calculate the fluctuations accurately, it is necessary to subtract the conductance with no disorder from the conductance with weak disorder to eliminate the influence of the mode transitions in conductance that may be seen in Fig. 3.1 (a). Fig. 3.2(a) gives the results after this subtraction. Then, a polynomial fit is used to determine the smoothed conductance and this is subtracted from the results in Fig. 3.2(a). The results for this δG as a function of Fermi energy and magnetic field are plotted in Fig. 3.2(b).

To clearly observe how the conductance fluctuations that arise in a Fermi energy sweep change as the magnetic fields increases, I plot them with and without the disorder potential at various magnetic fields in Fig. 3.3. There is a general reduction in the amplitude of the conductance fluctuations that can be observed as the magnetic field increases. When the magnetic field is larger than 3T, the conductance fluctuations basically disappear in the region of the conductance plateaus. There are some local fluctuations around the Fermi energy points where the mode number increases abruptly.

To quantitatively examine the fluctuation amplitude changes, I calculate the root-mean-square values of δG for Fermi energy sweeps at various magnetic fields. The results are given in Fig. 3.4(a). I consider 8 samples in my calculations and the mean values of root-mean-square of δG are averaged over these samples. It is clear that the value of δG (RMS) decreases from 0.35 to around 0.2 as the magnetic field increases from 0T to 5T. Fig. 3.4(b) gives the statistical error for discrete magnetic field values.

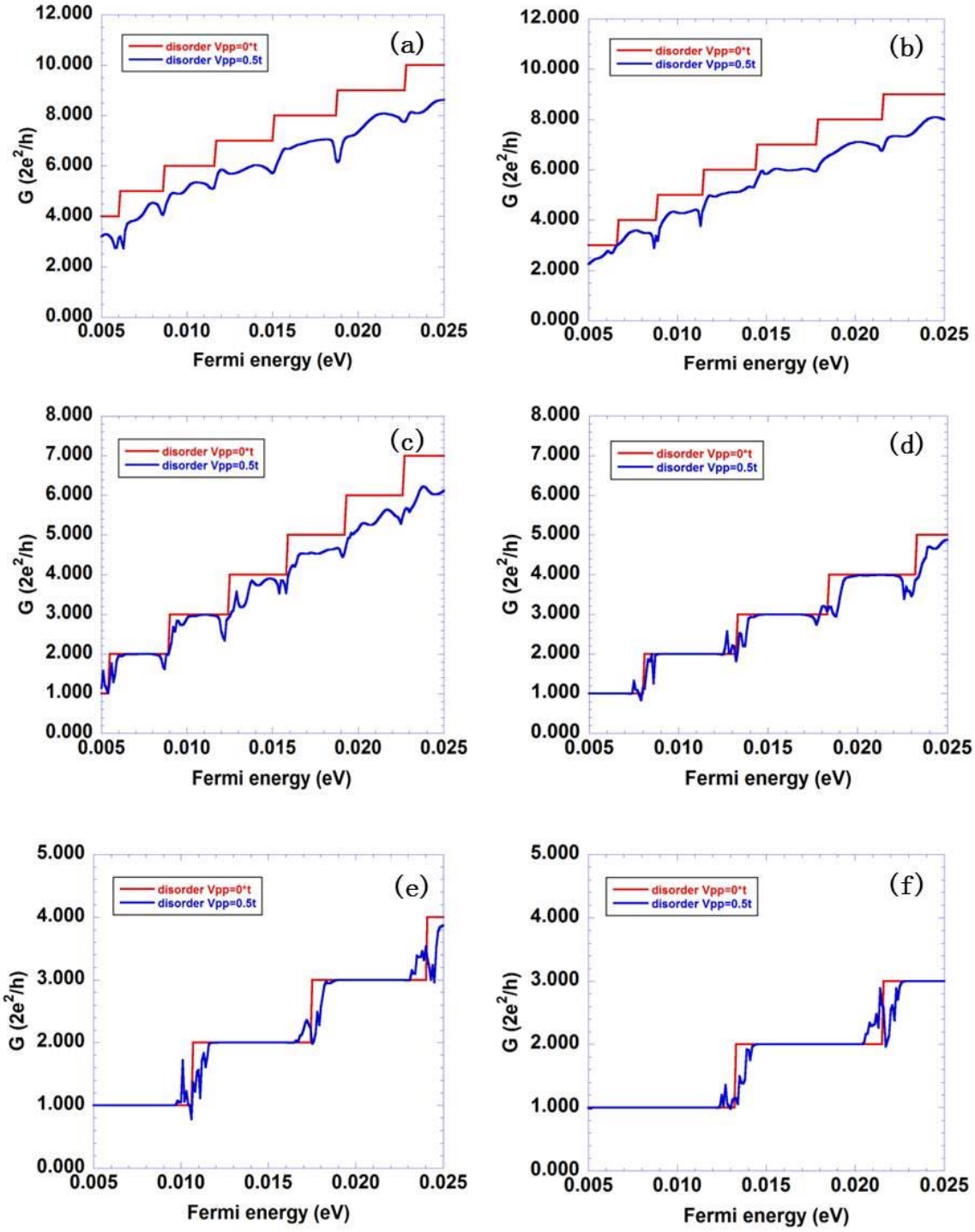

Fig. 3.3 Conductance for Fermi energy for a random potential with $V_{pp} = 0$ and $V_{pp} =$ 12.1 meV at a magnetic field of (a) 0 T (b) 1 T (c) 2 T (d) 3 T (e) 4 T (f) 5 T. Here, t = 24.2 meV.

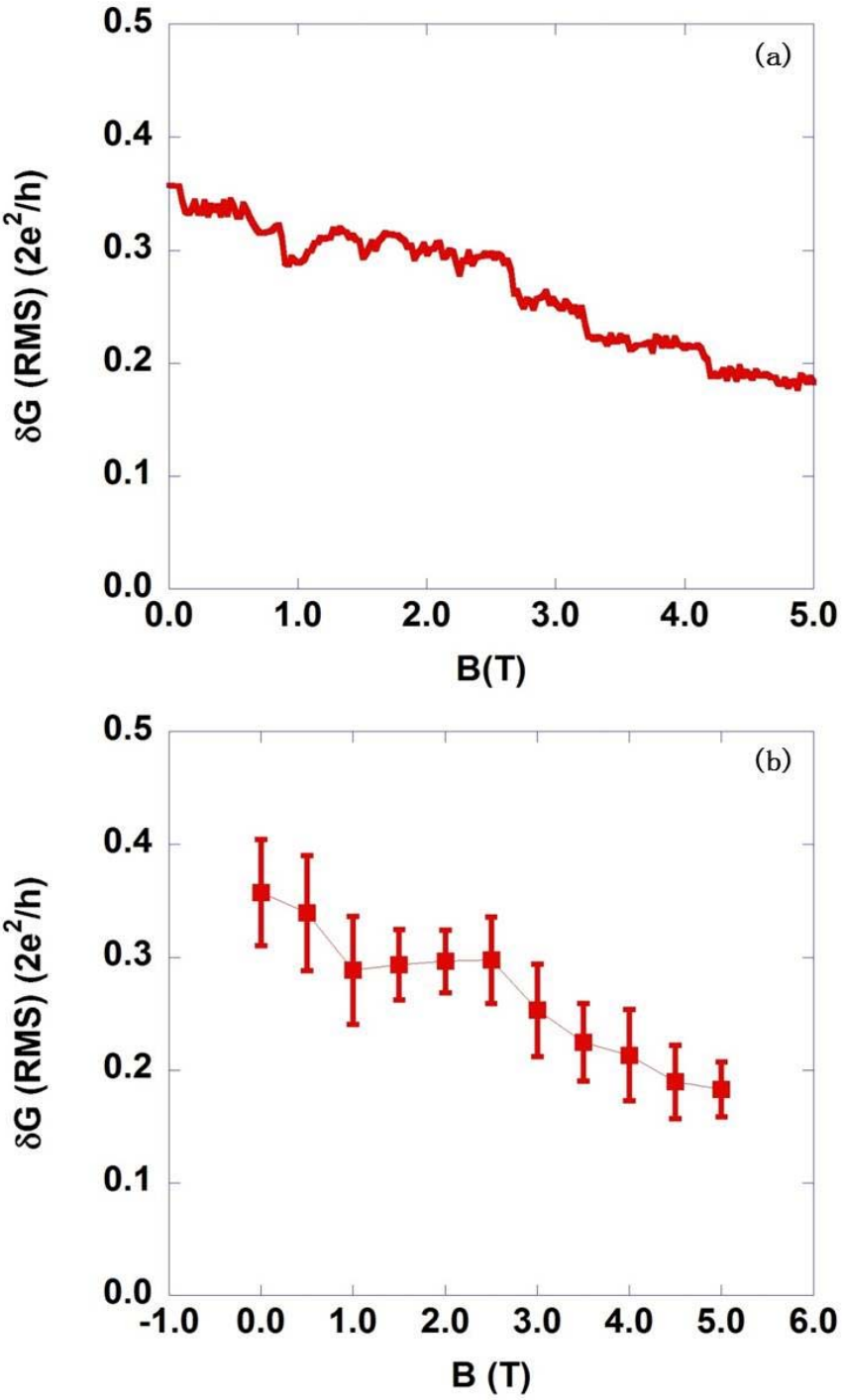

Fig. 3.4 (a) Mean of the root-mean-square values of δG for Fermi energy sweeps as a function of magnetic field for 8 samples. (b) Mean of the root-mean-square values of δG for Fermi energy sweeps as a function of magnetic fields with error bars shown for the 8 samples.

3.3 Conductance fluctuations for strong disorder

I consider a stronger disorder potential in this section. The peak-to-peak value of the random potential energy is 48.4 meV here. The conductance as function of Fermi energies and magnetic fields is plotted in Fig. 3.5(a). It shows that the conductance fluctuations appear at every value of Fermi energy from 5meV to 25meV. As before, the polynomial fits are determined and subtracted from the results in Fig. 3.5(a). This gives the values of δG as a function of Fermi energy and magnetic field and they are plotted in Fig. 3.5(b).

To clearly observe how the conductance fluctuations for Fermi energy sweeps changes as the magnetic fields increases, I plot the values determined, with and without the disorder potential, at magnetic fields of 0, 1, 2, 3, 4 and 5 T in Fig. 3.6. The tendency for a reduction of the amplitude of the fluctuations can be observed initially as the magnetic field increases, but this does not seem to be the case over the entire range of magnetic field.

To quantitatively examine the amplitude changes, I calculate the root-mean-square values of δG of the Fermi energy sweeps for each magnetic field. The results are given in Fig. 3.7(a). Again, I consider 8 samples in order to gather statistical properties, and the mean values of the root-mean-square δG are presented in Fig. 3.7(a). It is clear that the value of δG (RMS) decreases from 0.3 to around 0.2 as the magnetic field increases. Fig. 3.7(b) gives the statistical error for a few magnetic field values.

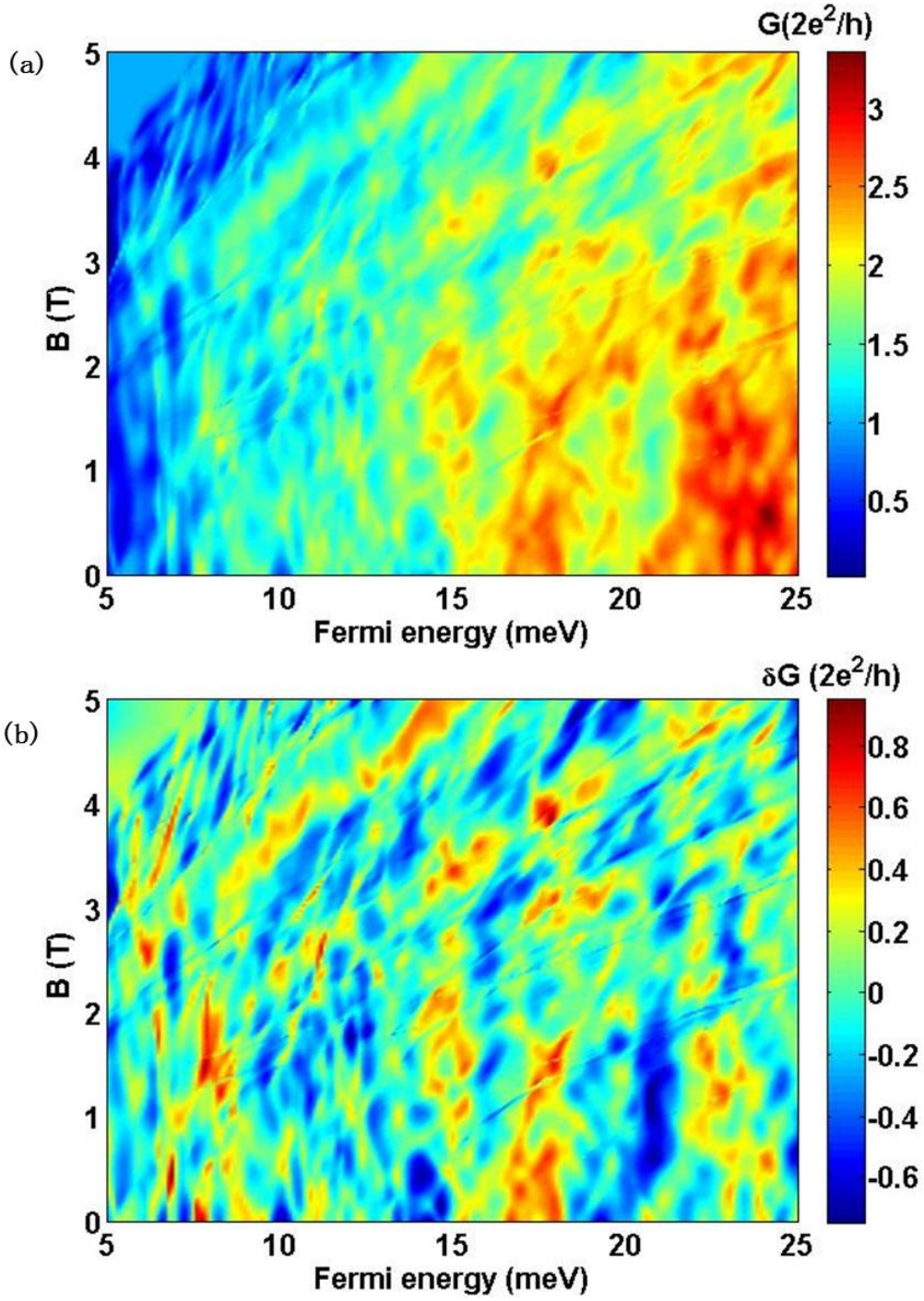

Fig. 3.5 (a) Plot of conductance as a function of Fermi energy and magnetic field for GaAs nanowires with size of 30 × 40 sites. Peak-to-peak value of the random potential energy is 48.4 meV. (b) Plot of conductance in (a) reduced by its polynomial fit as a function of Fermi energy and magnetic field.

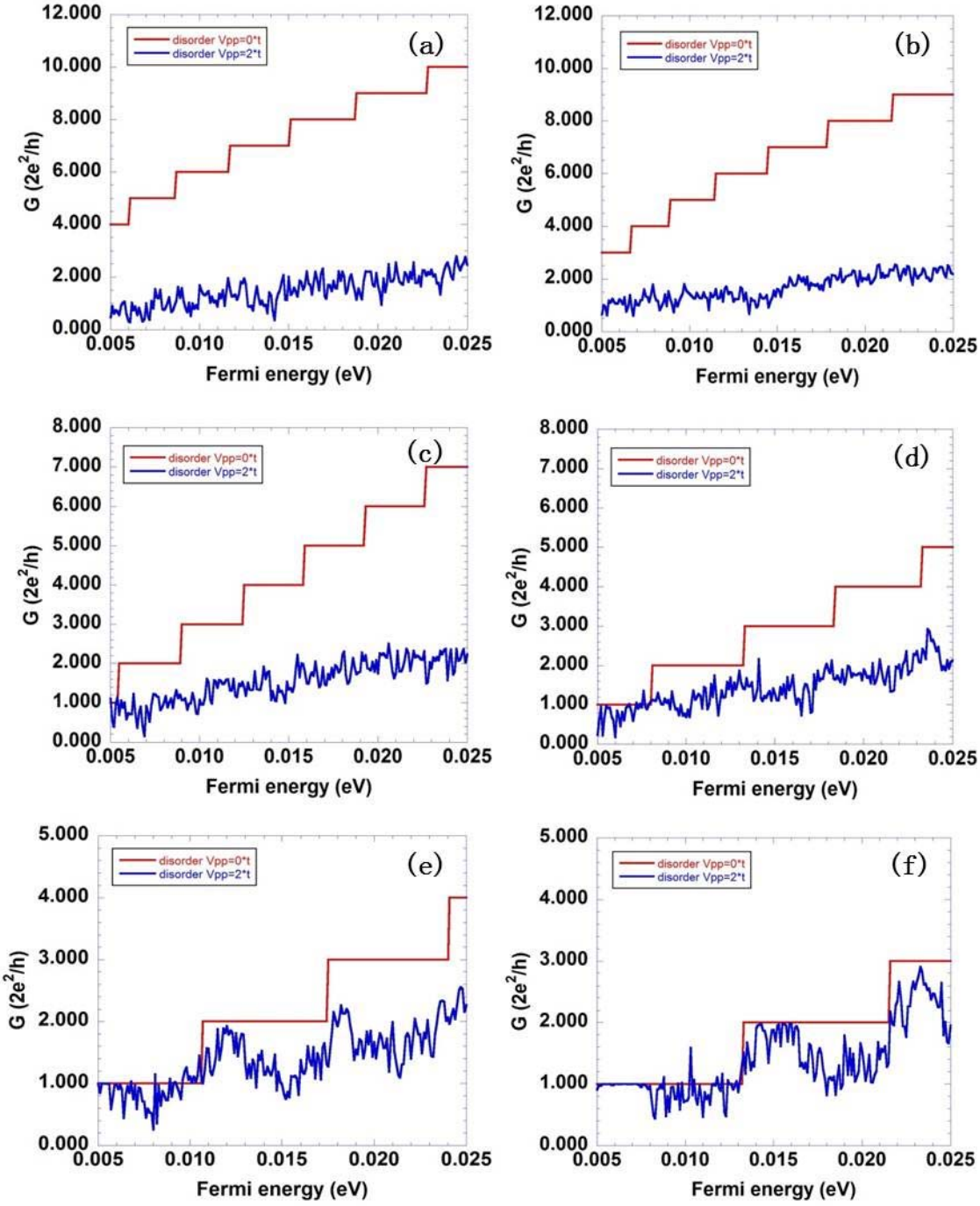

Fig. 3.6 Conductance as a funcntion of Fermi energy for no random potential and with V_{pp} =48.4 meV at (a) B=0T (b) 1 T (c) T (d) 3 T (e) 4 T (f) 5 T. Here, t = 24.2 meV.

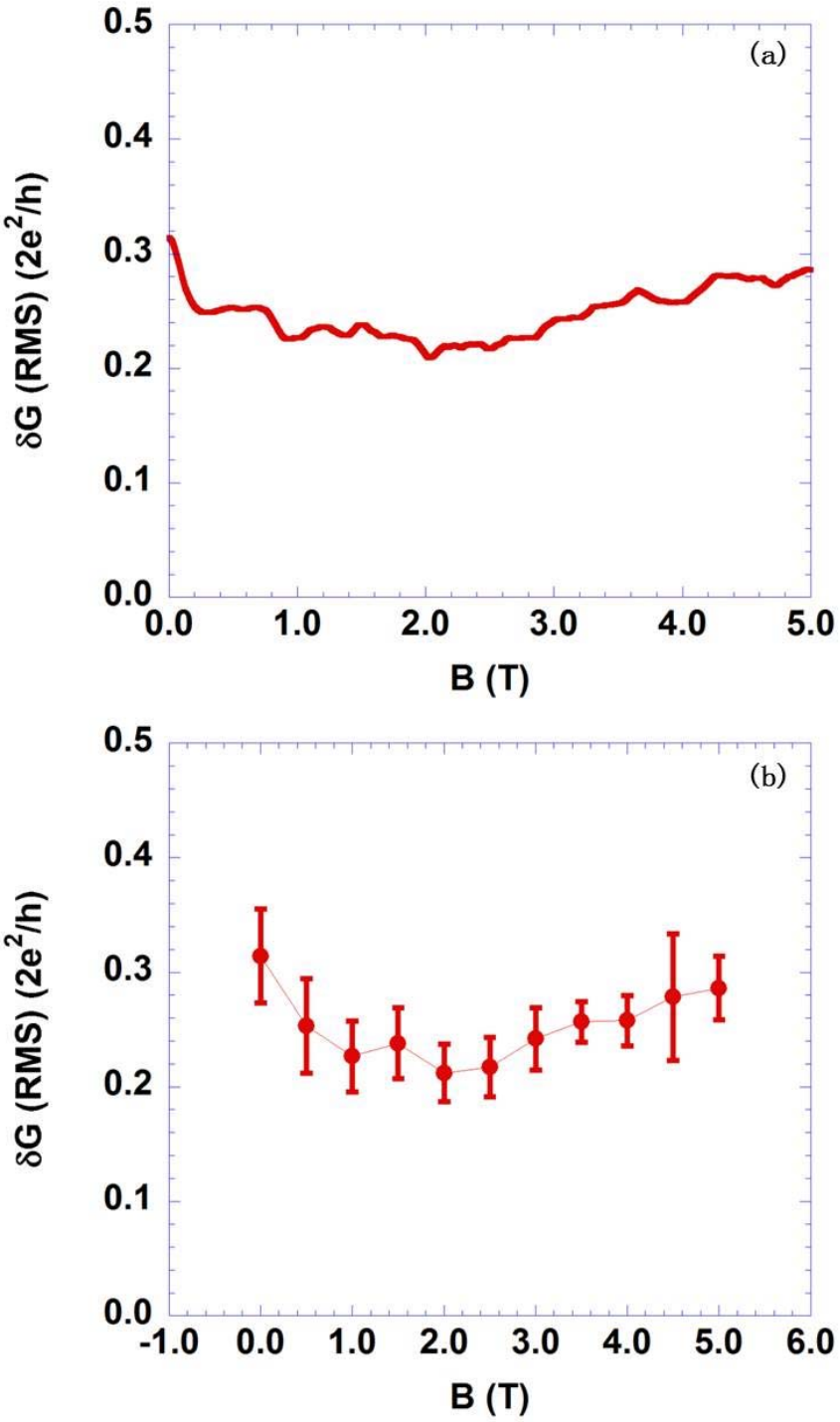

Fig. 3.7 (a) Mean of the root-mean-square values of δG for Fermi energy sweeps as a function of magnetic field. 8 samples are used to find the statistical averages. (b) Mean of the root-mean-square values of δG for Fermi energy sweeps as a function of magnetic field with error bars for the various samples.

3.4 Conclusions

In this chapter, I examine how the amplitude of conductance fluctuations for Fermi energy sweeps changes as the magnetic field is increased in GaAs nanowires. Both a weak amplitude of disorder (V_{pp} = 12.1 meV) and strong amplitude of disorder (V_{pp} = 48.4 meV) are considered in my investigation. The results indicate that the amplitude of conductance fluctuations for Fermi energy sweeps decrease as the magnetic field is increased from zero. This can be explained by the formation of edge states near the edges of the GaAs 2DEG induced by the external perpendicular magnetic field. Since for edge states, the scattering processes of electron waves with impurities mainly take place around the edge of the nanowires, the fluctuations under such cases will be weaker compared with the cases without magnetic fields, in which, scattering processes take place both inside the nanowires and near the edge.

CHAPTER 4

ATOMISTIC BASIS TECHNIQUES FOR GRAPHENE NANORIBBONS

4.1 Introduction

In the following chapters, I turn to graphene and study the conductance fluctuations in a graphene strip using the atomistic tight-binding model to further examine the dependence of variation of conductance for Fermi energy sweeps and magnetic field sweeps at different amplitudes of disorder. I will present the computational method in this chapter. The technique used here is based on the recursive scattering matrix approach that has been applied successfully in simulation of conductance fluctuations in GaAs-AlGaAs heterostructure 2DEG in chapter 2 [51, 56]. The Landauer-Büttiker formula is utilized to compute the conductance

$$G = \left(4e^2/h\right) \cdot \sum_{m,n} \frac{v_n}{v_m} \left|t_{n,m}\right|^2 , \tag{4.1}$$

in which, v_m and v_n are the velocities of different modes and the factor of 4 comes from and spin and valley degeneracy [17]. The Hamiltonian of the graphene atomic basis will be much different from that in finite difference method because graphene has a hexagonal lattice. The coupling Hamiltonian between slices will also have a generalized form which makes the transfer matrix equation more complicated. The Peierls phase factors will have different forms for different positions of hopping energies when the magnetic field is considered [51, 56].

This chapter is organized as follows. The slice Hamiltonian and the coupling Hamiltonian between slices will be given in section 4.2. The recursive scattering matrix

technique is presented in section 4.3. And in section 4.4, the magnetic field will be considered. Finally, the conclusion will be briefly discussed in section 4.5.

4.2 Slice Hamiltonian

I focus on the graphene ribbon with an armchair edge. Fig. 4.1 illustrates a typical graphene quantum wire scheme with two leads on left and right sides. There are two columns of carbon atoms in each slice, which makes the slice Hamiltonian have a dimension that is twice the number of atoms in each column. What is worth mentioning here is that, the reason of such a slicing scheme is to meet the requirement for construction of a transfer matrix for recursive scattering matrix approach. If I put one column of atoms into each slice, adjacent slices will have a different arrangement and orientation of atomic bond and Hamiltonian matrix, which brings difficulty to the construction of the transfer matrix [51, 56].

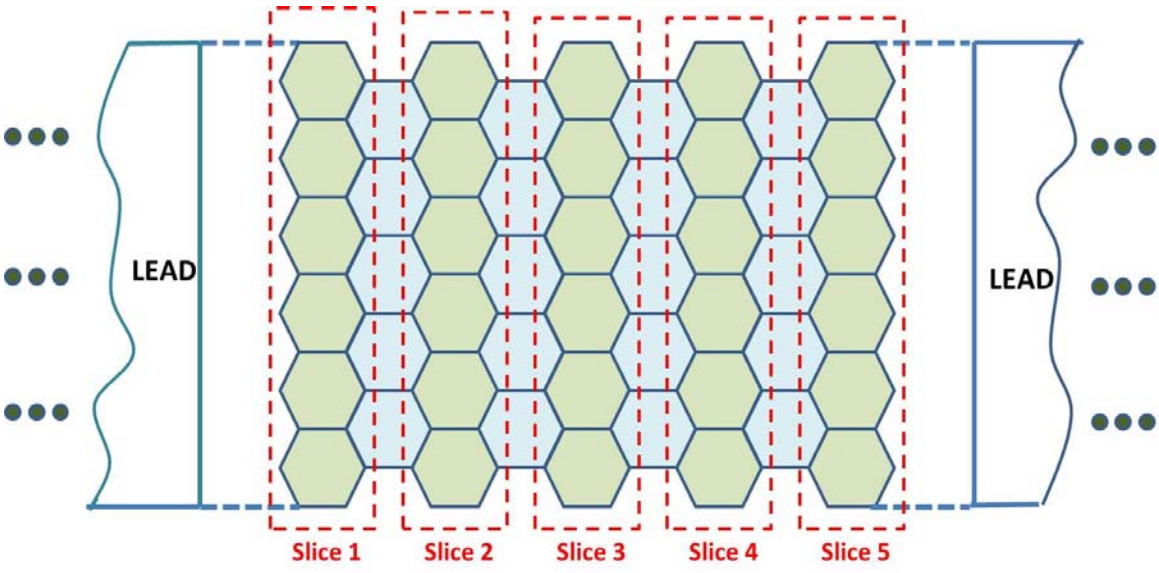

Fig. 4.1 Graphene nanoribbon with armchair edge and two probes on left and right sides and each slice contains two columns of carbon atoms [51, 56].

There can be many ways of writing the slice Hamiltonian and coupling Hamiltonian. What is common for different ways is that they all reflect the nature of graphene atomic lattice and hexagonal structure. For simplicity, I use three atoms in a column to show one of procedures of constructing the slice Hamiltonian which can be integrated into the transfer matrix conveniently [51, 56].

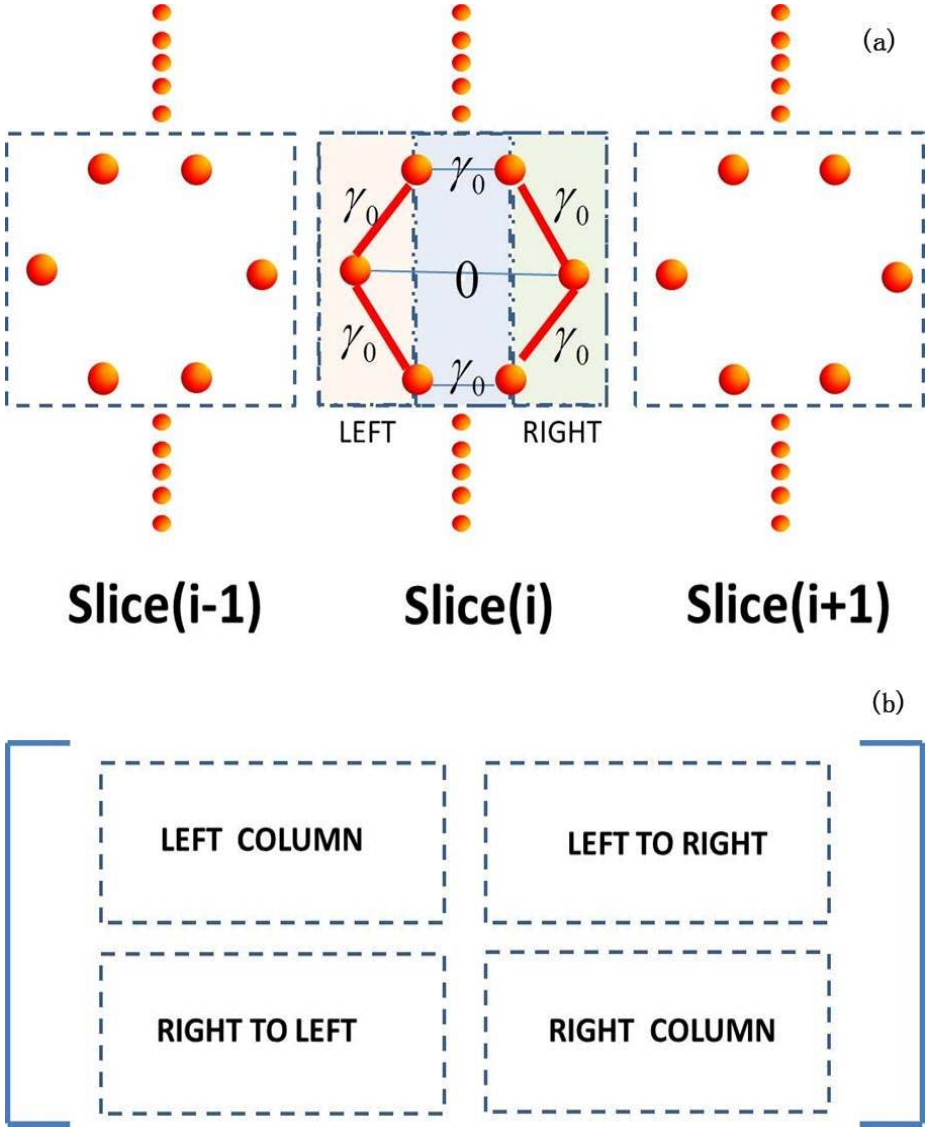

Fig. 4.2 (a) A graphical representation of Hamiltonian in a slice including 2 columns of atoms (b) The meaning of sub-matrices of slice Hamiltonian [56].

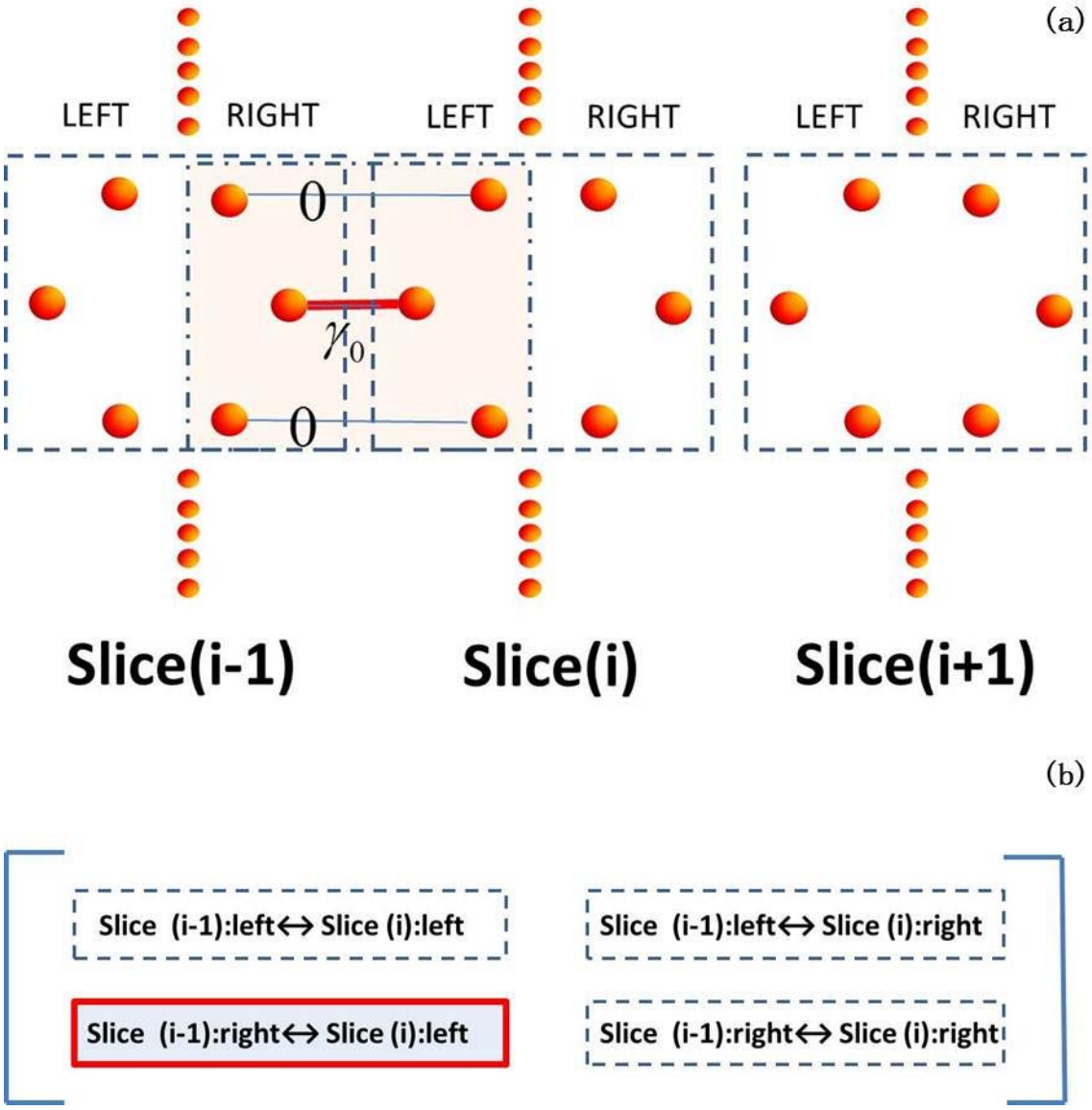

Fig. 4.3 (a) A graphical representation of coupling Hamiltonian for slice (i) and slice (i-1) (b) The meaning of sub-matrices in the slice coupling Hamiltonian [56].

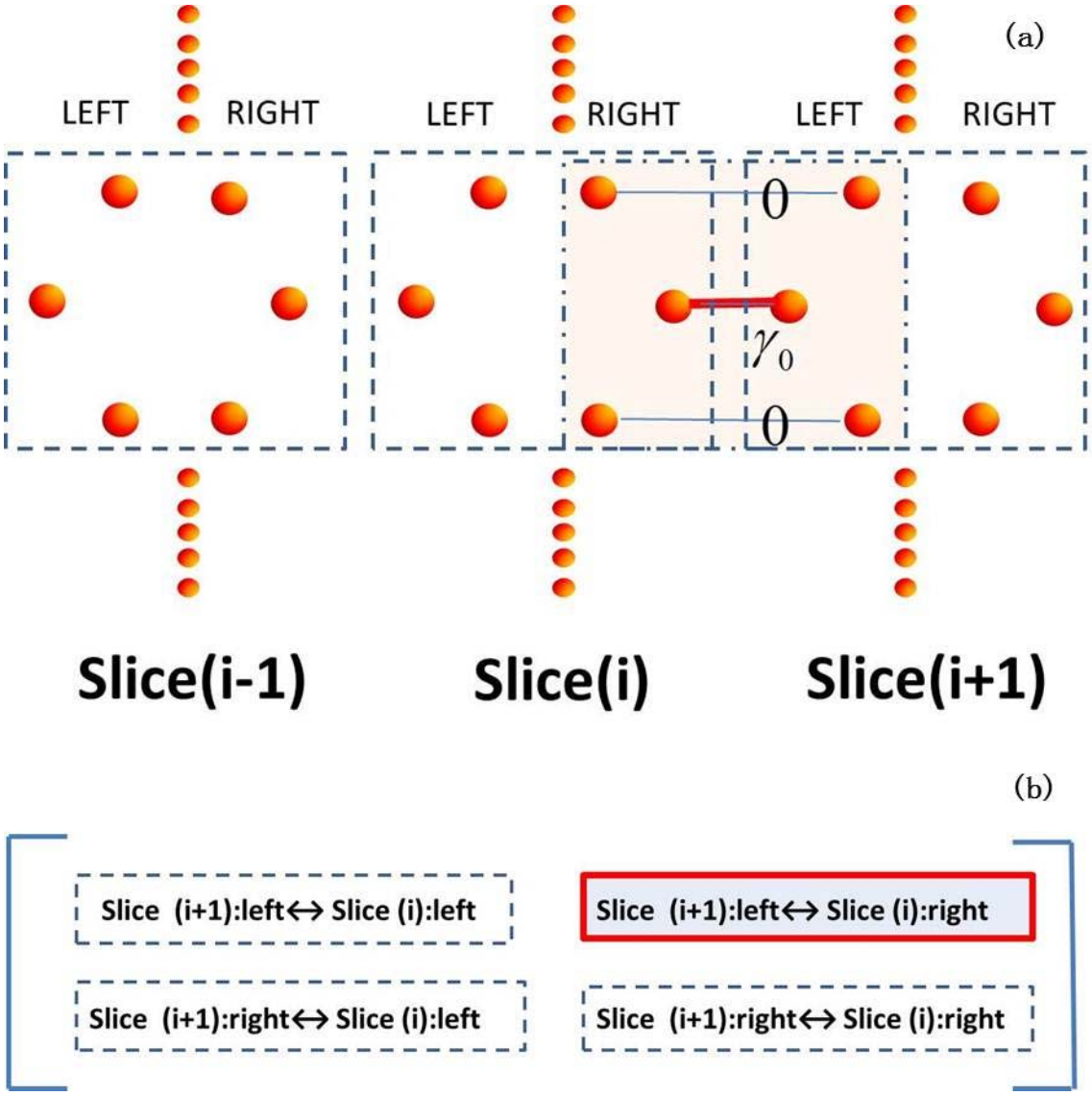

Fig. 4.4 (a) A graphical representation of coupling Hamiltonian for slice (i) and slice (i+1) (b) The meaning of sub-matrices in the slice coupling Hamiltonian [56].

As presented in Fig. 4.2, I consider the first nearest-neighbor hopping energy between neighboring carbon atoms, $\gamma_0 = 2.8eV$, which is the value of the overlap integral for two adjacent atoms wave function. I can write the slice Hamiltonian in the form

$$H_i = \begin{bmatrix} 0 & \gamma_0 & 0 & \gamma_0 & 0 & 0 \\ \gamma_0 & 0 & \gamma_0 & 0 & 0 & 0 \\ 0 & \gamma_0 & 0 & 0 & 0 & \gamma_0 \\ \gamma_0 & 0 & 0 & 0 & \gamma_0 & 0 \\ 0 & 0 & 0 & \gamma_0 & 0 & \gamma_0 \\ 0 & 0 & \gamma_0 & 0 & \gamma_0 & 0 \end{bmatrix}. \tag{4.2}$$

The Hamiltonians for left column atoms and right column atoms in slice *i*, placed in the left top and right down positions of H_i, are zero with the exception of the first off-diagonal terms. These two matrices represent the first nearest-neighbor coupling between adjacent atoms inside a column. The Hamiltonian which couples the two columns of atoms inside a slice is placed in the right up and left down parts of matrix H_i [56].

Now I turn to the Hamiltonians that couple slice i to its left neighbor slice i-1 and right neighbor slice i+1. Fig. 4.3 gives the meaning of the four parts in coupling matrix that connects slice i-1 and i. As I only consider the first nearest hopping energy, the left down part of H_L is not zero. Similarly, Fig. 4.4 tells how the coupling matrix for slice i and i+1 is obtained. There is a nonzero sub-matrix in the right top part of the Hamiltonian H_R. And the inter-slice coupling matrix for the left and right neighboring matrices are given as [56]

$$H_L = \begin{bmatrix} 0 & 0 & 0 & 0 & 0 & 0 \\ 0 & 0 & 0 & 0 & 0 & 0 \\ 0 & 0 & 0 & 0 & 0 & 0 \\ 0 & 0 & 0 & 0 & 0 & 0 \\ 0 & \gamma_0 & 0 & 0 & 0 & 0 \\ 0 & 0 & 0 & 0 & 0 & 0 \end{bmatrix}, \tag{4.3}$$

and

$$H_R = \begin{bmatrix} 0 & 0 & 0 & 0 & 0 & 0 \\ 0 & 0 & 0 & 0 & \gamma_0 & 0 \\ 0 & 0 & 0 & 0 & 0 & 0 \\ 0 & 0 & 0 & 0 & 0 & 0 \\ 0 & 0 & 0 & 0 & 0 & 0 \\ 0 & 0 & 0 & 0 & 0 & 0 \end{bmatrix}. \tag{4.4}$$

By now, the slice Hamiltonian for this simple armchair edge graphene ribbon has been established, where only three atoms exist in a column. This method can be very easily extended to larger sizes of graphene ribbons, which can contain more atoms in a column and more slices. And undoubtedly, the dimension of the corresponding Hamiltonian will be much larger. Overall, the purpose of building Hamiltonians in this manner is to get them integrated into the transfer matrix for recursive calculation, which will be told in the next section.

4.3 Recursive scattering matrix techniques

Considering the matrix form of 2D Schrödinger equation of GaAs 2DEG, I can write a generalized version of matrix form of the Schrödinger equation

$$H_i\vec{\psi}_i - H_L\vec{\psi}_{i-1} - H_R\vec{\psi}_{i+1} = EI\vec{\psi}_i. \tag{4.5}$$

H_i is the matrix representing the Hamiltonian for the individual isolated slice i and H_L and H_R are the inter-slice coupling matrices. E is the Fermi energy and I is the unit matrix [52, 53].

Next the transfer-matrix equation which couples adjacent slices can be written as

$$\begin{bmatrix} \vec{\psi}_i \\ \vec{\psi}_{i+1} \end{bmatrix} = \begin{bmatrix} 0 & I \\ -H_L/H_R & \left(H_i - EI\right)/H_R \end{bmatrix} \begin{bmatrix} \vec{\psi}_{i-1} \\ \vec{\psi}_i \end{bmatrix} = T_i \begin{bmatrix} \vec{\psi}_{i-1} \\ \vec{\psi}_i \end{bmatrix}. \tag{4.6}$$

A problem in the above transfer matrix is that H_R is not invertible. To overcome this problem, I put a very small number η in the diagonal of both H_L and H_R [56].

$$H_L = \begin{bmatrix} \eta & 0 & 0 & 0 & 0 & 0 \\ 0 & \eta & 0 & 0 & 0 & 0 \\ 0 & 0 & \eta & 0 & 0 & 0 \\ 0 & 0 & 0 & \eta & 0 & 0 \\ 0 & \gamma_0 & 0 & 0 & \eta & 0 \\ 0 & 0 & 0 & 0 & 0 & \eta \end{bmatrix} \tag{4.7a}$$

and

$$H_R = \begin{bmatrix} \eta & 0 & 0 & 0 & 0 & 0 \\ 0 & \eta & 0 & 0 & \gamma_0 & 0 \\ 0 & 0 & \eta & 0 & 0 & 0 \\ 0 & 0 & 0 & \eta & 0 & 0 \\ 0 & 0 & 0 & 0 & \eta & 0 \\ 0 & 0 & 0 & 0 & 0 & \eta \end{bmatrix}. \tag{4.7b}$$

Here η plays a role of very weak coupling between third nearest neighboring atoms in different slices.

Using the Bloch's theorem, I calculate the eigenvalue and eigenfunction for the zeroth slice and the wavefunction in the form

$$\begin{bmatrix} u_m(\pm) \\ \lambda_m(\pm) u_m(\pm) \end{bmatrix}. \tag{4.8}$$

Here, the symbol $(\pm)$ gives the mode propagation directions with $(+)$ for right and $(-)$ for left. And the actual current in the quantum wire is carried by the propagating modes. The transfer equation for a graphene ribbon with N slices turns to be

$$\begin{bmatrix} t \\ 0 \end{bmatrix} = T_0^{-1} T_N T_{N-1} \ldots T_1 T_0 \begin{bmatrix} I \\ r \end{bmatrix}. \tag{4.9}$$

The main difficulty in solving the above equation is the numerical instability. It can be overcome by rewriting it into the scattering matrix form, which was developed early by Usuki *et al*. [52]. The iterative scheme relates adjacent slices as

$$\begin{bmatrix} C_1^{l+1} & C_2^{l+1} \\ 0 & I \end{bmatrix} = T_l \begin{bmatrix} C_1^{l} & C_2^{l} \\ 0 & I \end{bmatrix} \begin{bmatrix} I & 0 \\ P_{l1} & P_{l2} \end{bmatrix}. \tag{4.10}$$

with $P_{l1} = -P_{l2} T_{l21} C_1^l$ and $P_{l2} = \left(T_{l21} C_2^l + T_{l22} \right)^{-1}$. [51, 52, 53, 56] Starting by $C_1^0 = I$ and $C_2^0 = 0$, the final transmission matrix t is obtained

$$t = -\left(U^+ \lambda^+ \right)^{-1} \left[C_2^{N+1} - U^+ \left(U^+ \lambda^+ \right)^{-1} \right]^{-1} C_1^{N+1} \ . \tag{4.11}$$

Finally, the conductance of the graphene nanoribbon can be computed using Eq. (4.1).

4.4 Incorporation of magnetic field

The incorporation of magnetic field is performed via the insertion of the Peierls phase factors to the nearest-neighbor hopping energy terms in the matrices of the slice Hamiltonian and the coupling Hamiltonian. Using the Landau gauge, the vector potential of a perpendicular magnetic field $\vec{B} = (0, 0, B)$ is in a form of $\vec{A} = (-By, 0, 0)$. The Peierls phase factor can be obtained by the path integral over the vector potential between two nearest carbon atoms. Due to the hexagonal honeycomb structure in graphene and the different positions of hopping energy terms in slice Hamiltonian and coupling Hamiltonian, the Peierls phase needs to be calculated separately [56].

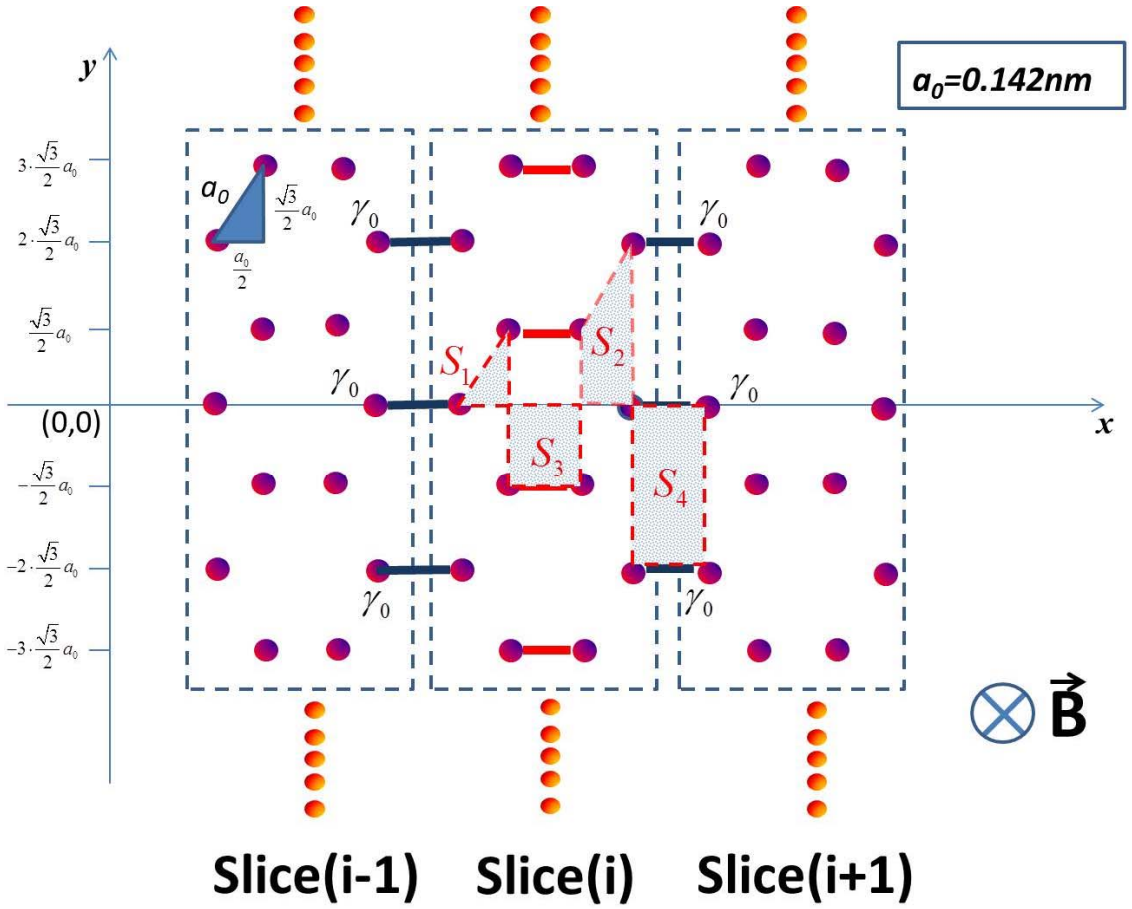

Fig. 4.5 A graphical representation of magnetic flux cross section between adjacent hopping terms near the center of ribbon (y=0) [56].

In Fig. 4.5, the different types of magnetic flux cross section shapes are illustrated and I use a rectangular plane coordinate and set the center of slice at the position of y=0. Such a symmetric placement of the slice along y axis avoids the shifting the dispersion relation. The Peierls phase can be written into the form

$$\theta = 2\pi\frac{\phi}{\phi_0} = \frac{2\pi e}{h}\int \vec{A}\cdot d\vec{l} = \frac{2\pi e}{h}\int(-By)\cdot dx = -\frac{2\pi eB}{h}\int y\cdot dx = -\frac{2\pi eB}{h}\cdot S\,. \qquad (4.12)$$

Here $\phi_0 = \frac{h}{e}$ is the flux quantum and it is found that the value of Peierls phase factor depends on the magnetic flux cross section area S, which is shown in Fig. 4.5. The phase factor can be calculated along the y axis for different carbon atoms in the slices. The values of the phase factor in Fig. 4.5 are

$$\begin{aligned}
\theta_1 &= \left(-\frac{2\pi eB}{h}\right)\cdot S_1 = \left(-\frac{2\pi eB}{h}\right)\cdot\frac{1}{2}\cdot\frac{a_0}{2}\cdot\frac{\sqrt{3}a_0}{2} = \left(-\frac{2\pi eB}{h}\right)\cdot\frac{\sqrt{3}a_0{}^2}{8} \\
\theta_2 &= \left(-\frac{2\pi eB}{h}\right)\cdot S_2 = \left(-\frac{2\pi eB}{h}\right)\cdot 3\cdot S_1 = \left(-\frac{2\pi eB}{h}\right)\cdot\frac{3\sqrt{3}a_0{}^2}{8} \\
\theta_3 &= \left(-\frac{2\pi eB}{h}\right)\cdot S_3 = \left(-\frac{2\pi eB}{h}\right)\cdot\frac{\sqrt{3}a_0}{2}\cdot a_0 = \left(-\frac{2\pi eB}{h}\right)\cdot\frac{\sqrt{3}a_0{}^2}{2} \\
\theta_4 &= \left(-\frac{2\pi eB}{h}\right)\cdot S_4 = \left(-\frac{2\pi eB}{h}\right)\cdot 2\cdot S_3 = \left(-\frac{2\pi eB}{h}\right)\cdot\sqrt{3}a_0{}^2
\end{aligned} \quad . \tag{4.13}$$

Then the Peierls phase factor can be inserted into slice Hamiltonian H_i, which becomes

$$H_i = \begin{bmatrix}
0 & \gamma_0 e^{-i\theta_1} & 0 & \gamma_0 e^{i\theta_3} & 0 & 0 \\
\gamma_0 e^{i\theta_1} & 0 & \gamma_0 e^{-i\theta_1} & 0 & 0 & 0 \\
0 & \gamma_0 e^{i\theta_1} & 0 & 0 & 0 & \gamma_0 e^{-i\theta_3} \\
\gamma_0 e^{-i\theta_3} & 0 & 0 & 0 & \gamma_0 e^{i\theta_1} & 0 \\
0 & 0 & 0 & \gamma_0 e^{-i\theta_1} & 0 & \gamma_0 e^{i\theta_1} \\
0 & 0 & \gamma_0 e^{i\theta_3} & 0 & \gamma_0 e^{-i\theta_1} & 0
\end{bmatrix}. \tag{4.14}$$

And the coupling matrix H_L and H_R will also have a new form. Suppose that each column contains 5 atoms, then the H_L and H_R matrices have dimensions of 10×10. Hence, $\left(H_L\right)_{6,1} = \gamma_0 e^{i\theta_4}$, $\left(H_L\right)_{10,5} = \gamma_0 e^{-i\theta_4}$, $\left(H_R\right)_{1,6} = \gamma_0 e^{-i\theta_4}$ and $\left(H_R\right)_{5,10} = \gamma_0 e^{i\theta_4}$ [56].

The basic calculation methods and structure are introduced above through an example with 3 atoms in each column and the number of atoms can be easily increased to study a larger size of sample. The Hamiltonian with a magnetic field can be integrated

into the transfer matrix in a same way as that without a magnetic field. The conductance of the wire can be calculated through the recursive approach that has been presented in section 4.3.

4.5 Conclusion

The details of the computational techniques using the atomistic basis tight-binding model to compute the conductance in graphene nanoribbons are presented in this section. 3 atoms are used in each column to explain the meaning the sub-matrix in slice Hamiltonian and coupling Hamiltonian. The Hamiltonian can be integrated into a generalized transfer matrix and the conductance can be calculated using the recursive scattering matrix techniques. The method of incorporating the magnetic field into the Peierls phase factor is also given in this chapter [56].

CHAPTER 5

CONDUCTANCE FLUCTUATIONS IN GRAPHENE NANORIBBONS IN THE PRESENCE OF SHORT-RANGE DISORDER

5.1 Introduction

In this chapter, the conductance fluctuations in graphene nanoribbons, in the presence of short-range disorder, are studied [17, 55]. The bandstructure of graphene nanoribbons with armchair edges is calculated in the beginning for both metallic and semiconducting cases [54]. Landau levels can be observed when a magnetic field is applied. The computational techniques introduced in chapter 4 are used to calculate the conductance of graphene nanoribbons. The short-range disorder potential is incorporated at each carbon atom site [56]. The conductance fluctuations are calculated for both Fermi energy sweeps and magnetic field sweeps. The root-mean-square values of conductance fluctuations are computed at different amplitudes of the disorder potential to examine the universality of fluctuations in graphene nanoribbons [19]. I also compare the root-mean-square values of conductance fluctuations for Fermi energy sweeps and magnetic field sweeps as well as the rms values of amplitudes of fluctuations for Fermi energy sweeps under different magnetic fields.

This chapter is organized as follows. The band structure of graphene nanoribbons for both metallic and semiconducting cases is discussed in section 5.2. The calculation of conductance for Fermi energy sweeps and magnetic field sweeps is given in section 5.3. Then the conductance fluctuations for short-range disorder potential are introduced in section 5.4. Finally, the rms values of the amplitude of fluctuations for Fermi energy sweeps and magnetic fields sweeps are summarized in section 5.5.

5.2 Band structure

In this section, I turn to the calculation of the band structure of the graphene ribbon with finite width and armchair edges. The slice Hamiltonian and coupling Hamiltonian obtained in chapter 4 can be written as block matrices with four sub-matrices as [54]

$$H_i = \begin{bmatrix} H_{iL} & H_{iLR} \\ H_{iRL} & H_{iR} \end{bmatrix}, H_L = \begin{bmatrix} 0 & 0 \\ H_{LD} & 0 \end{bmatrix} \text{and} \quad H_R = \begin{bmatrix} 0 & H_{RU} \\ 0 & 0 \end{bmatrix}. \tag{5.1}$$

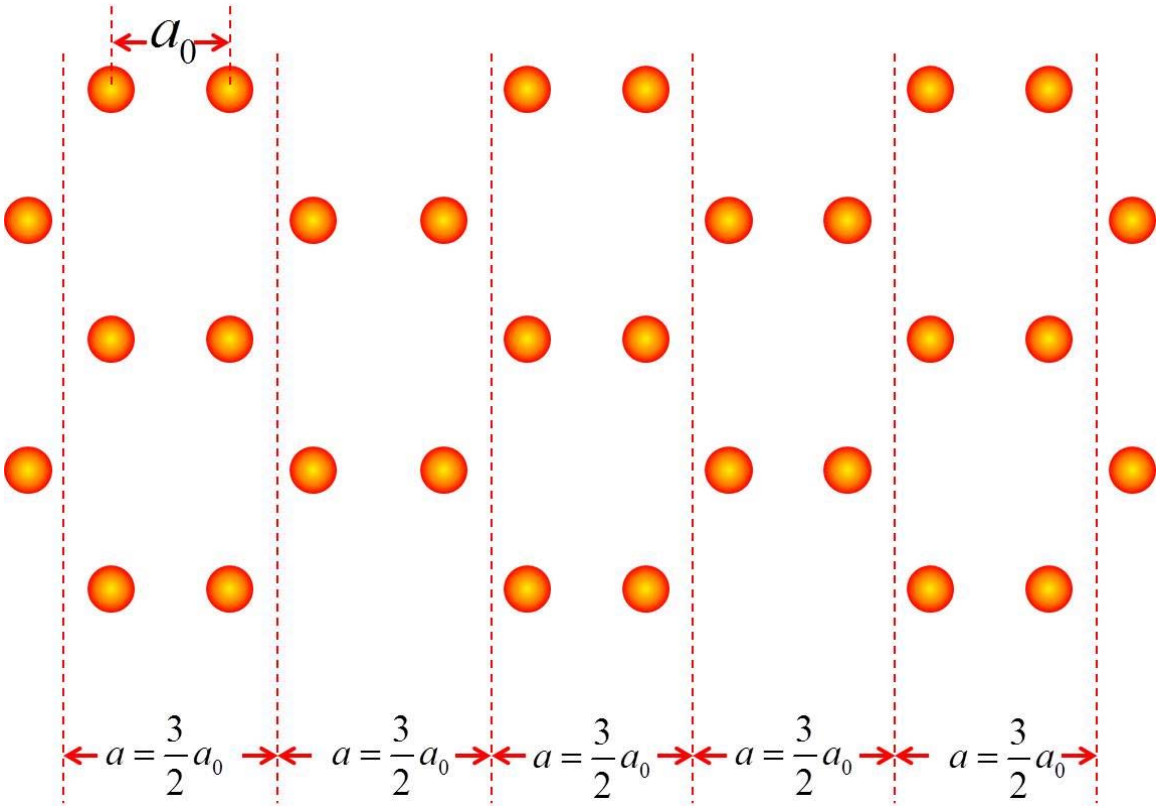

Fig. 5.1 The average distance between columns of atoms for monolayer graphene with armchair edge is *a* [54].

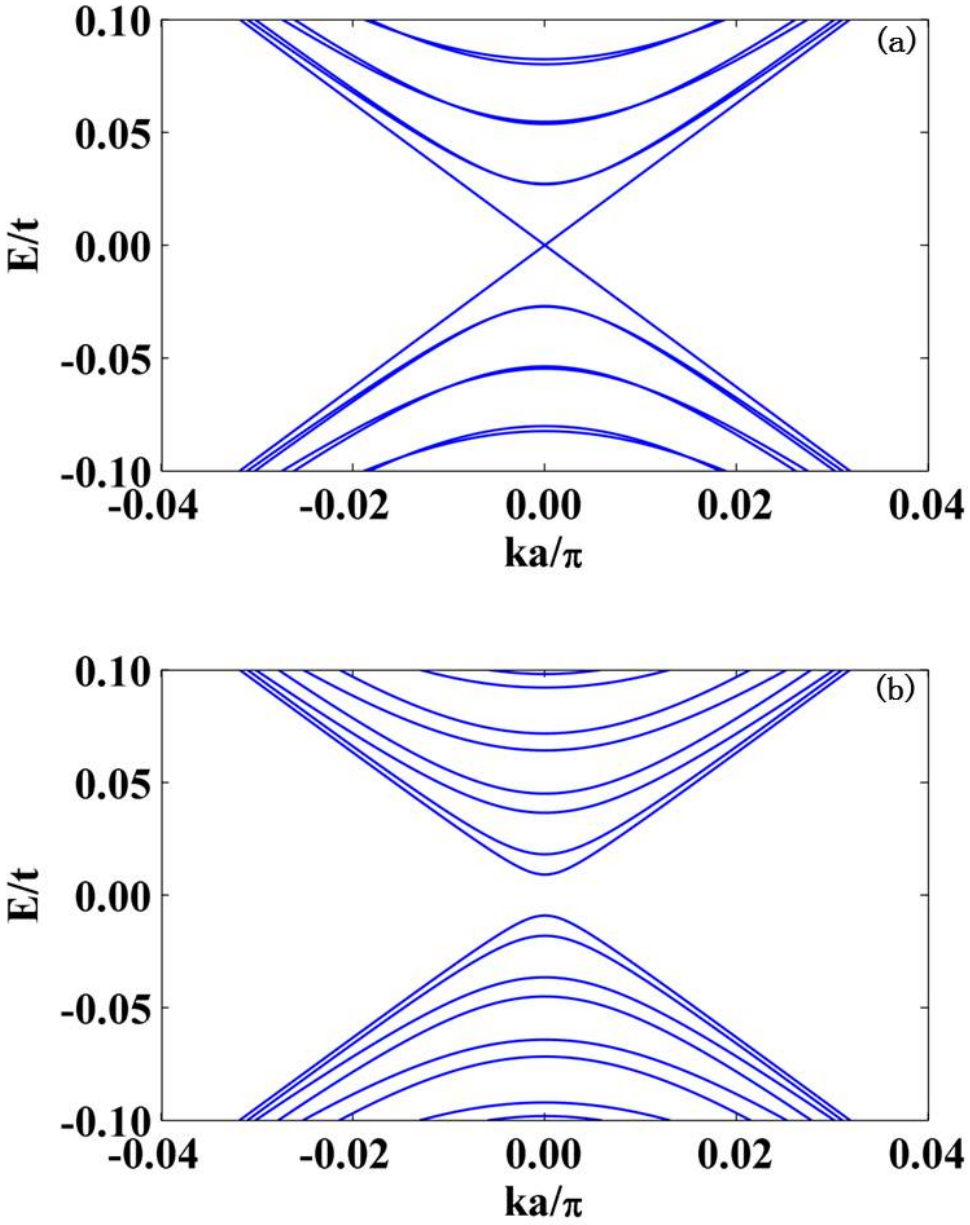

Fig. 5.2 (a) Bandstructure of graphene nanoribbon with width of 200 atoms at a magnetic field of 0T. (b) Bandstructure of graphene nanoribbon with width of 199 atoms at a magnetic field of 0T [56].

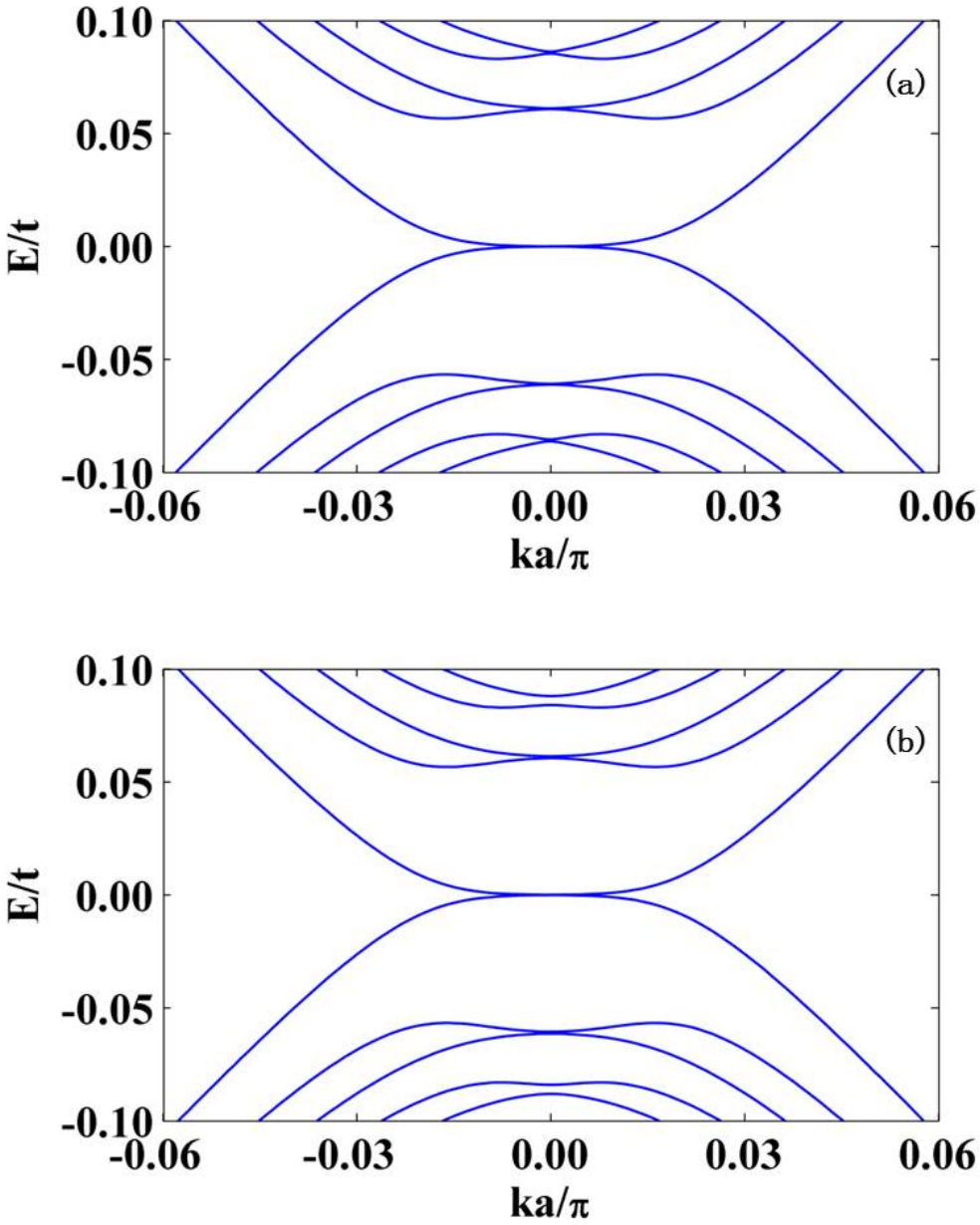

Fig. 5.3 (a) Bandstructure of graphene nanoribbon with width of 200 atoms at a magnetic field of 27T. (b) Bandstructure of graphene nanoribbon with width of 199 atoms at a magnetic field of 27T [56].

Then the band structure can be obtained by solving and sorting the eigenvalues of the following Hamiltonian which is the Bloch sum of the slice Hamiltonian [54]

$$H = \begin{bmatrix} 0 & 0 \\ H_{LD}\cdot\exp(ika) & 0 \end{bmatrix} + \begin{bmatrix} H_{iL} & H_{iLR}\cdot\exp(ika) \\ H_{iRL}\cdot\exp(-ika) & H_{iR} \end{bmatrix} + \begin{bmatrix} 0 & H_{RU}\cdot\exp(-ika) \\ 0 & 0 \end{bmatrix}. \quad (5.2)$$

Here, $a = \frac{3}{2}a_0$ is the average column interval distance, as shown in Fig. 5.1.

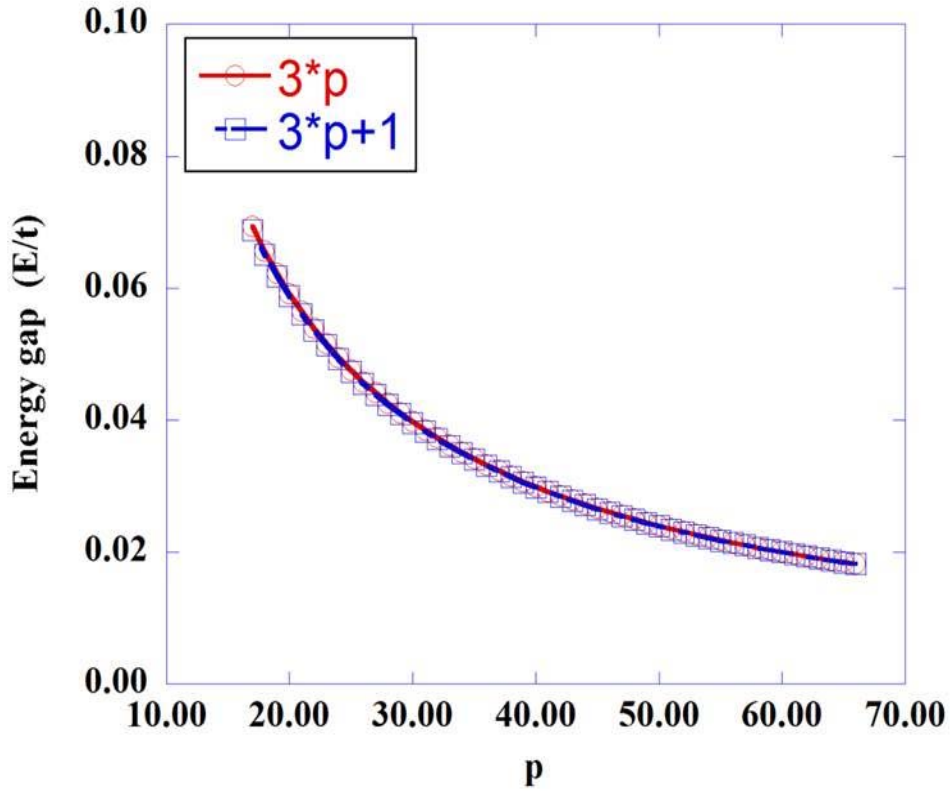

Fig. 5.4 The energy gap as a function of number p. The width of graphene nanoribbon are 3×p and 3×p+1 respectively.

The band structures for graphene nanoribbons with width of 199 and 200 atoms are presented in Fig. 5.2 [56]. There is no energy gap around the point E/t=0 for a nanoribbon with width of 200 atoms, which is metallic. Here, t is the nearest-neighbor hopping energy $t = \gamma_0 = 2.8eV$. But, for a ribbon width of 199 atoms, an energy gap exists

near E/t=0, showing that it is semiconducting. The band structure under a perpendicular magnetic field is computed and shown in Fig. 5.3 [56]. Under a magnetic field of 27 T, Landau levels can be observed in the band structure and neither metallic nor semiconducting cases do have an energy gap around the point E/t=0. To examine the dependence of the width of the energy gap for semiconducting case on the width of the graphene nanoribbon, the width of the energy gap is calculated for graphene nanoribbon with width of 3×p and 3×p+1 in Fig. 5.4. As the value of p increases from 17 to 66, the width of energy gap drops from 0.07×t to 0.02×t. The energy gaps for widths of 3×p and 3×p+1 are very close to one another at all widths of the nanoribbons.

5.3 Conductance

The sample in my calculation is a rectangular graphene ribbon with armchair edges. It breaks into 100 slices and two vertical columns of carbon atoms are in each slice. The Transverse width of the graphene nanoribbon is 24.348nm for 199 atoms in each column and 24.471nm for 200 atoms in each column. Using the computing approach presented in chapter 4 [51, 52, 53, 56], I obtain here the conductance for a sweep of the Fermi energy over the range of 50meV – 250meV. Both the metallic and semiconducting ribbons are considered and the results are shown in Fig. 5.5 [56]. The unit of conductance is $4e^2/h$ and the factor of 4 comes from the spin degeneracy of electrons and valley degeneracy of graphene. Fig. 5.5 (a) shows the conductance for Fermi energy sweeps at a magnetic field of 0T, 10T, 27T, 50T and 100T for a metallic nanoribbon, while the conductance for the semiconducting nanoribbon is given in Fig. 5.5 (b) [56]. The

depopulation of conductance can be observed in Fig. 5.5 when the magnetic fields are increased [56].

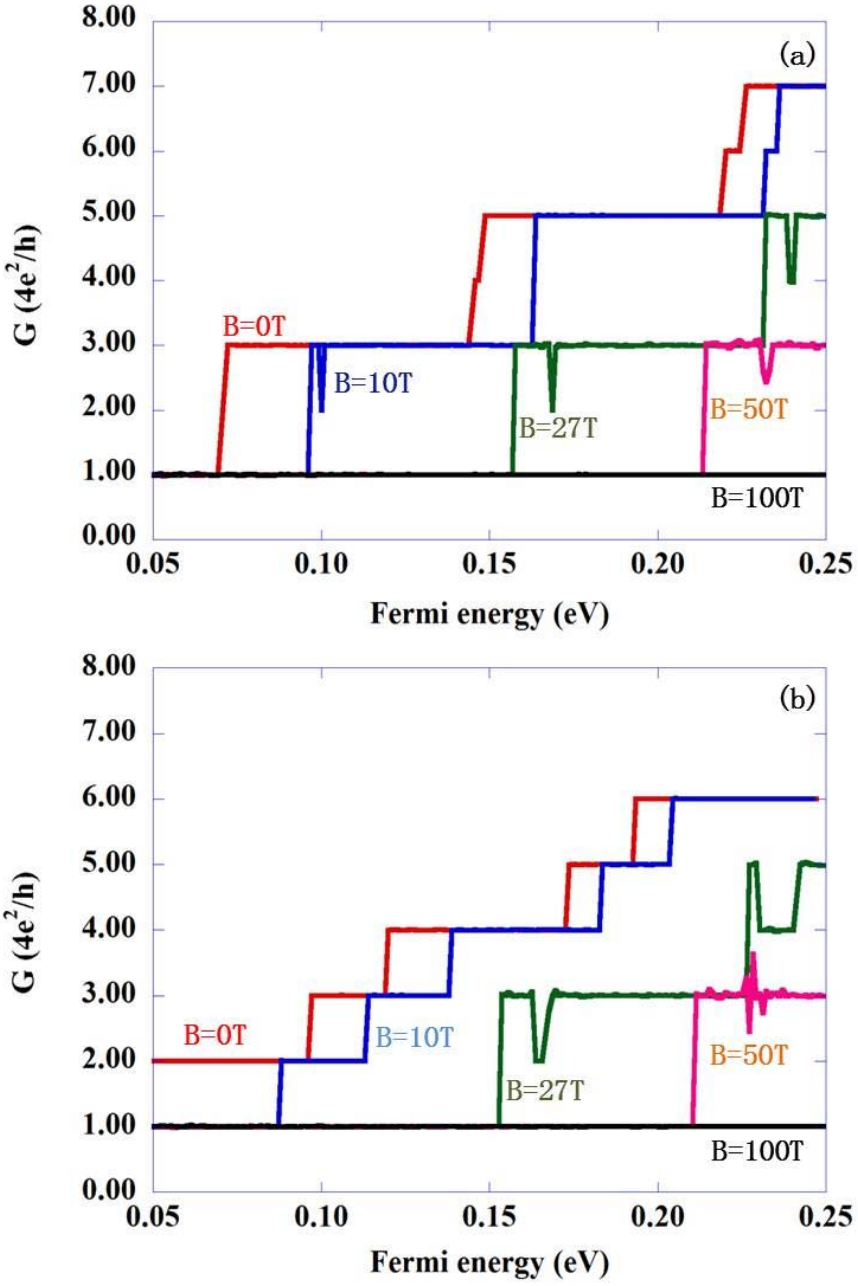

Fig. 5.5 Conductance for Fermi energy sweeps from 50meV to 250meV at B=0T, 10T, 27T, 50T and 100T for a graphene nanoribbon with width of (a) 200 atoms and (b) 199 atoms [56].

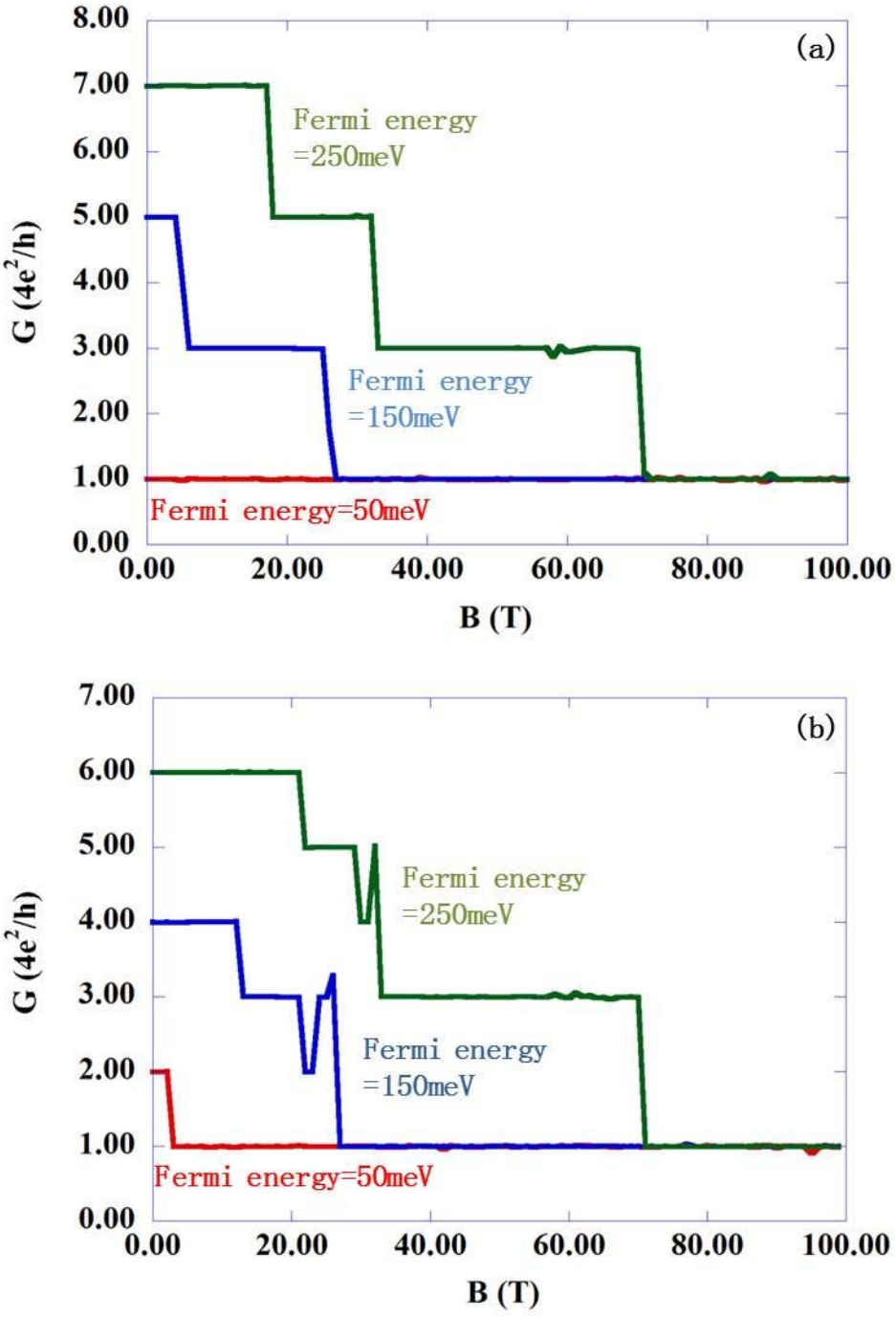

Fig. 5.6 Conductance for magnetic field sweeps from 0T to 100T at Fermi energies of 50meV, 150meV and 250meV for a graphene nanoribbon with width of (a) 200 atoms and (b) 199 atoms [56].

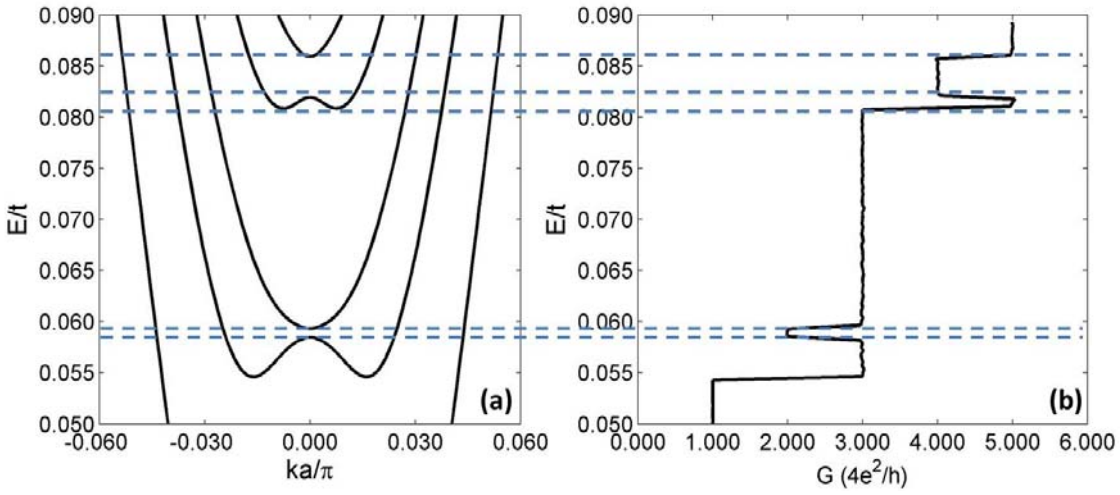

Fig. 5.7 The relation between the energy gap in the band structure (a) and the drop of conductance (b). Here, the number of atoms is 199 in each column [56].

The conductance for magnetic field sweeps is given for Fermi energies of 50meV, 150meV and 250meV in a graphene ribbon with width of both 200 atoms in Fig. 5.6 (a) and 199 atoms in Fig. 5.6 (b). As the magnetic field is increased, the space between Landau levels gets larger. Thus, for a fixed Fermi energy, the number of energy levels that can be occupied by electrons decreases and correspondingly, the number of propagating modes is reduced, which leads to a reduction in the conductance [56].

Another interesting point in Fig. 5.5 and Fig. 5.6 is that there are some dips in the conductance in the plateaus for specific values of the magnetic field. The reason is explained in Fig. 5.7, using a zoom of the band structure for a graphene ribbon with a width of 199 atoms in a magnetic field of 27T [56]. It shows that a gap exists near E/t=0.058 for ka=0, which reduces the mode number from 3 to 2. After the Fermi energy passes across the gap, the mode number turns back to 3 from 2 again. The variation of the conductance in Fig. 5.7 (b) agrees with the variation of modes in Fig. 5.7 (a) [56].

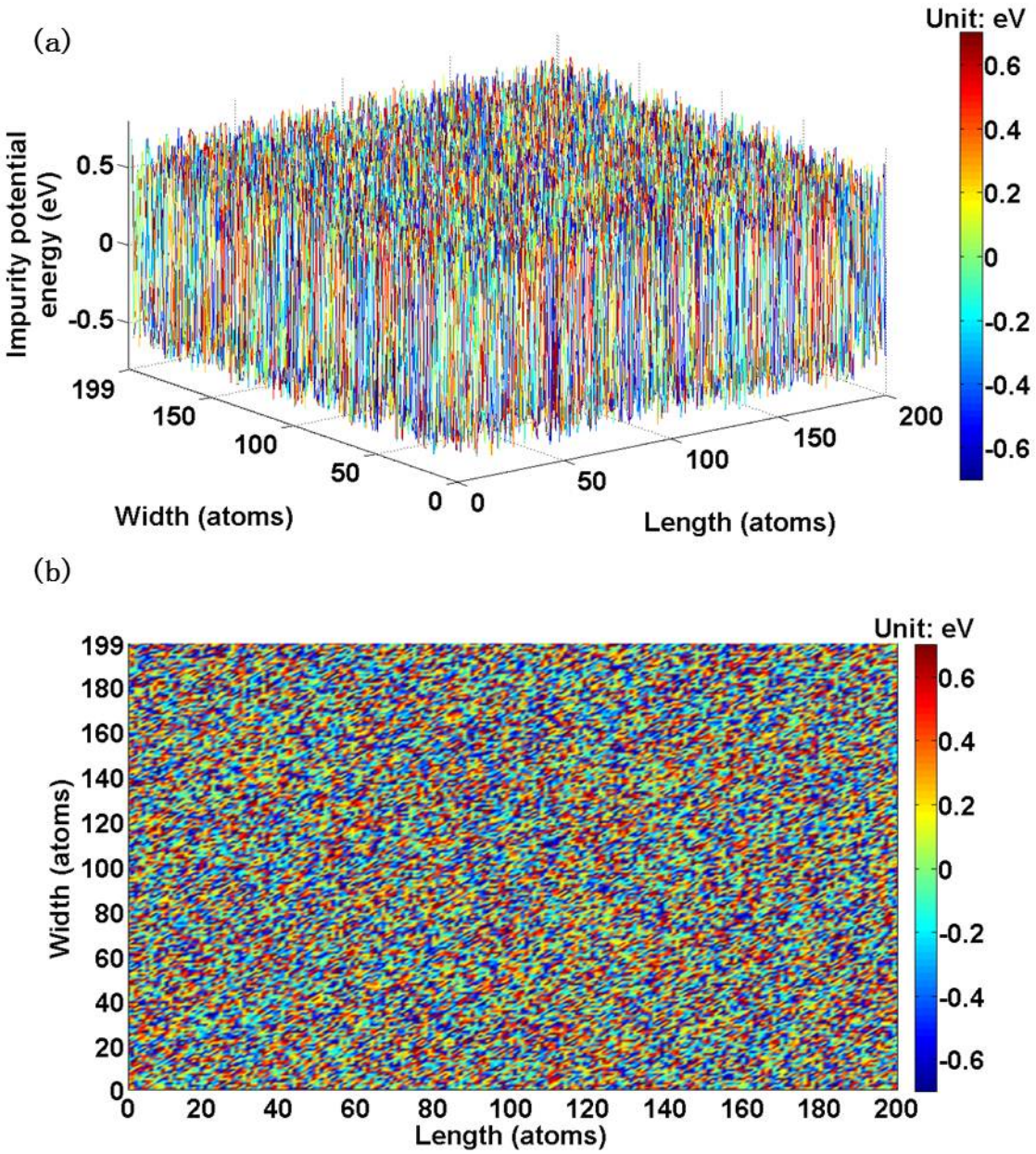

Fig. 5.8 (a) 3D plot of the short-range disorder potential. (b) 2D plot of the short-range disorder potential [55].

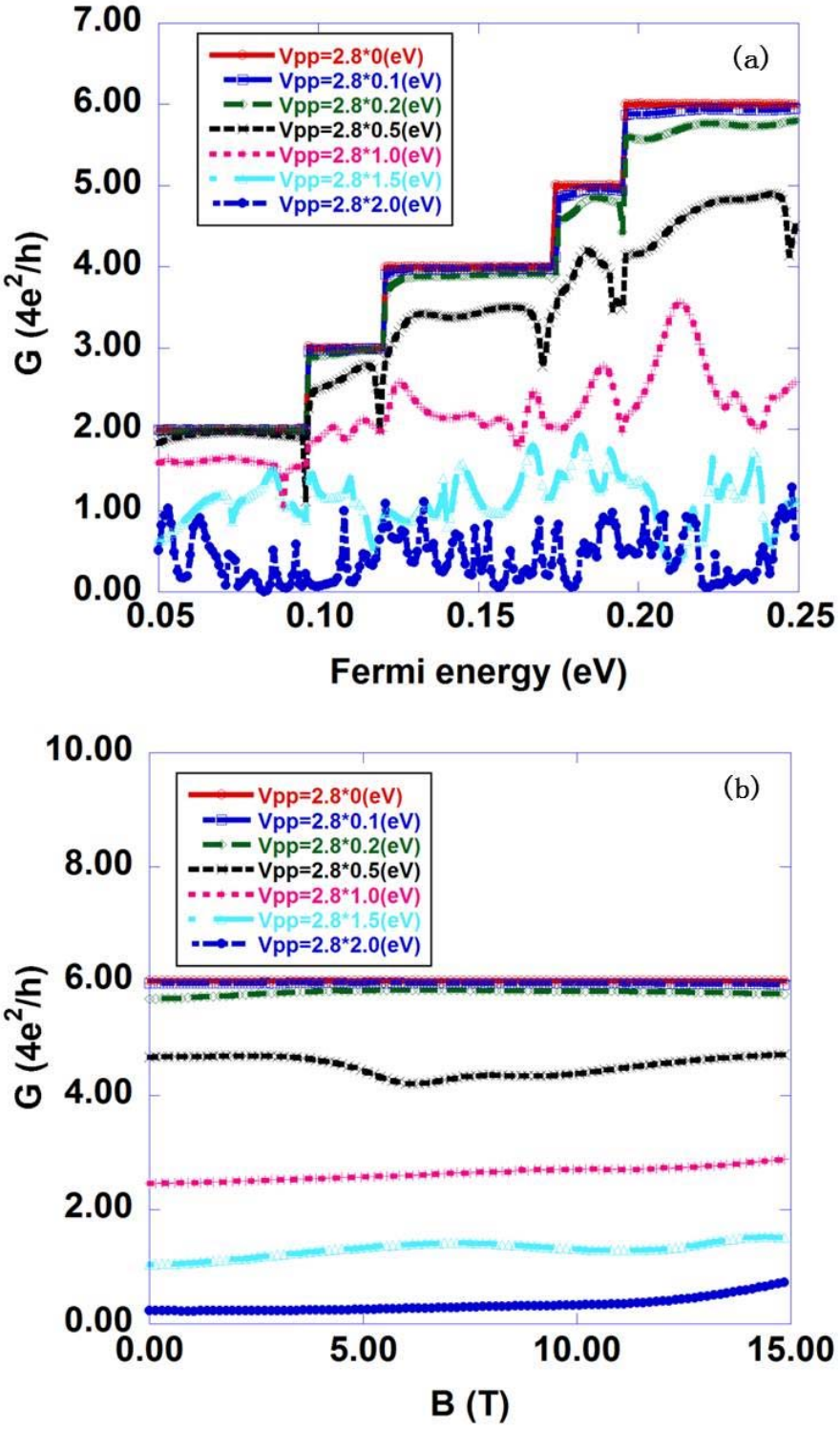

Fig. 5.9 Conductance fluctuations for (a) Fermi energy sweeps at B=0T and (b) magnetic field sweeps at a Fermi energy of 250meV for Vp-p=2.8eV × [0, 0.1, 0.2, 0.5, 1.0, 1.5, 2.0] [56].

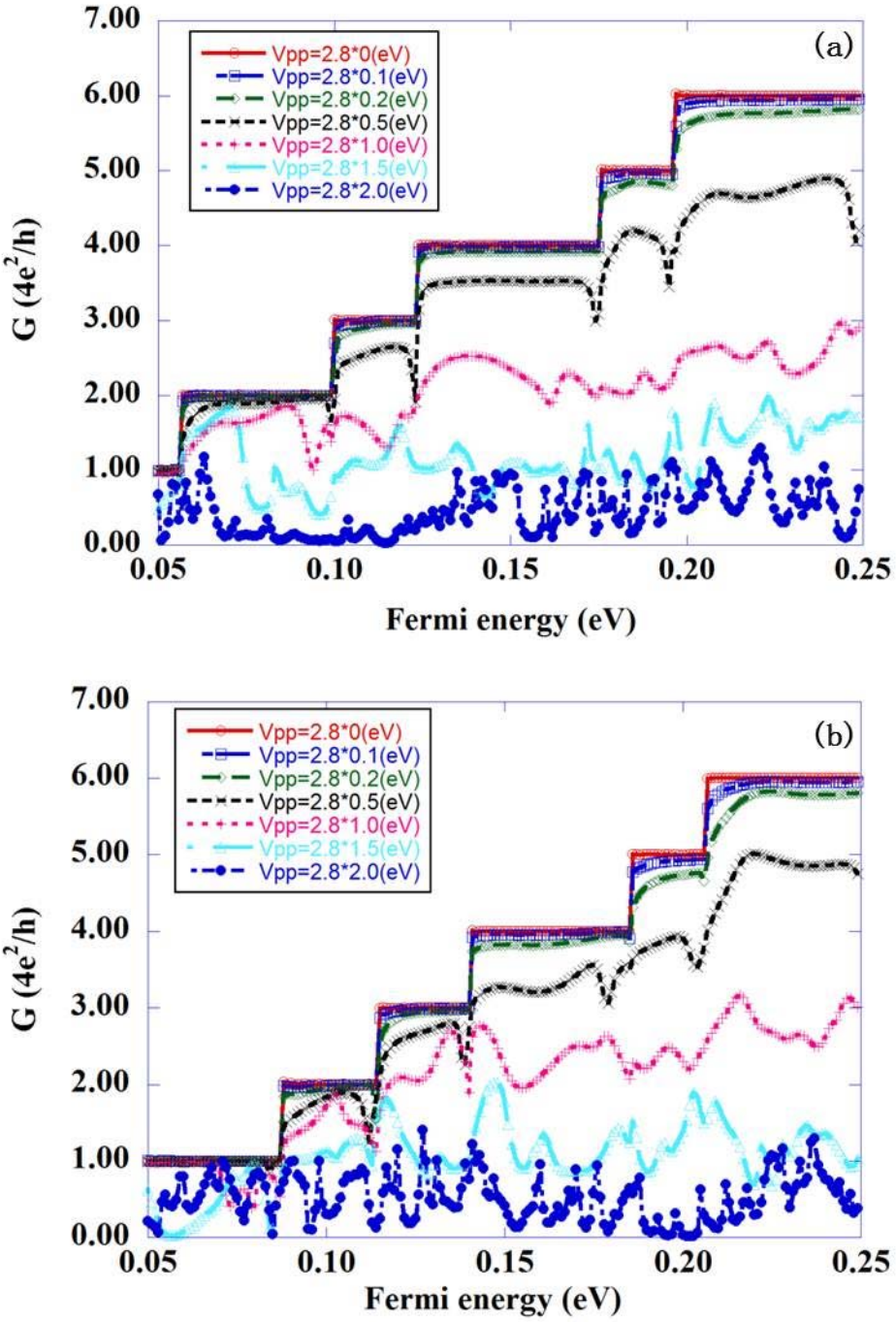

Fig. 5.10 Conductance fluctuations for Fermi energy sweeps at magnetic fields of (a) 4T and (b) 10T for Vp-p=2.8eV × [0, 0.1, 0.2, 0.5, 1.0, 1.5, 2.0] [56].

5.4 Conductance fluctuations

The short-range impurity disorder is introduced by adding a random potential δU at each atom site [17, 55]. The random potential δU is a uniformly distributed random number in the range [-ΔU/2, +ΔU/2]. In my calculation, I study seven distinct peak-to-peak values of random potential $\Delta U = \{0,\ 0.1,\ 0.2,\ 0.5,\ 1.0,\ 1.5,\ 2.0\} \times \gamma_0$. γ_0=2.8eV is the nearest-neighbor hopping energy for adjacent carbon atoms. Fig. 5.8 shows an example of short-range disorder potential with peak-to-peak value of ΔU=1.4eV [17, 55].

The conductance fluctuations are calculated for Fermi energy sweeps from 50meV to 250meV at a magnetic field of 0T in Fig. 5.9 (a) and magnetic field sweeps from 0T to 15T at a Fermi energy of 250meV in Fig. 5.9 (b) [56]. As the peak-to-peak values of short-range disorder potential energy increases from 0eV to 5.6eV, the depopulation of conductance can be observed. The conductance fluctuations for Fermi energy sweeps under a magnetic field of 4T are plotted in Fig. 5.10 (a) and the conductance fluctuations under a magnetic field of 10T are plotted in Fig. 5.10 (b) [56].

I use a polynomial fit to calculate the background conductance and then subtract this from the original conductance to obtain the δG values as a function of Fermi energy or of magnetic field [57]. An example of the δG values is given in Fig. 5.11 for a disorder potential with peak-to-peak value of 2.8eV [57]. Fig. 5.11 (a) shows the value of δG as a function of Fermi energy and Fig. 5.11 (b) shows the value of δG as a function of magnetic field [57]. It is obvious that the amplitude of fluctuations for Fermi energy sweeps is larger than that for magnetic field sweeps. The calculation of δG is performed for several different samples at different amplitudes of disorder potential, and these are averaged together [57].

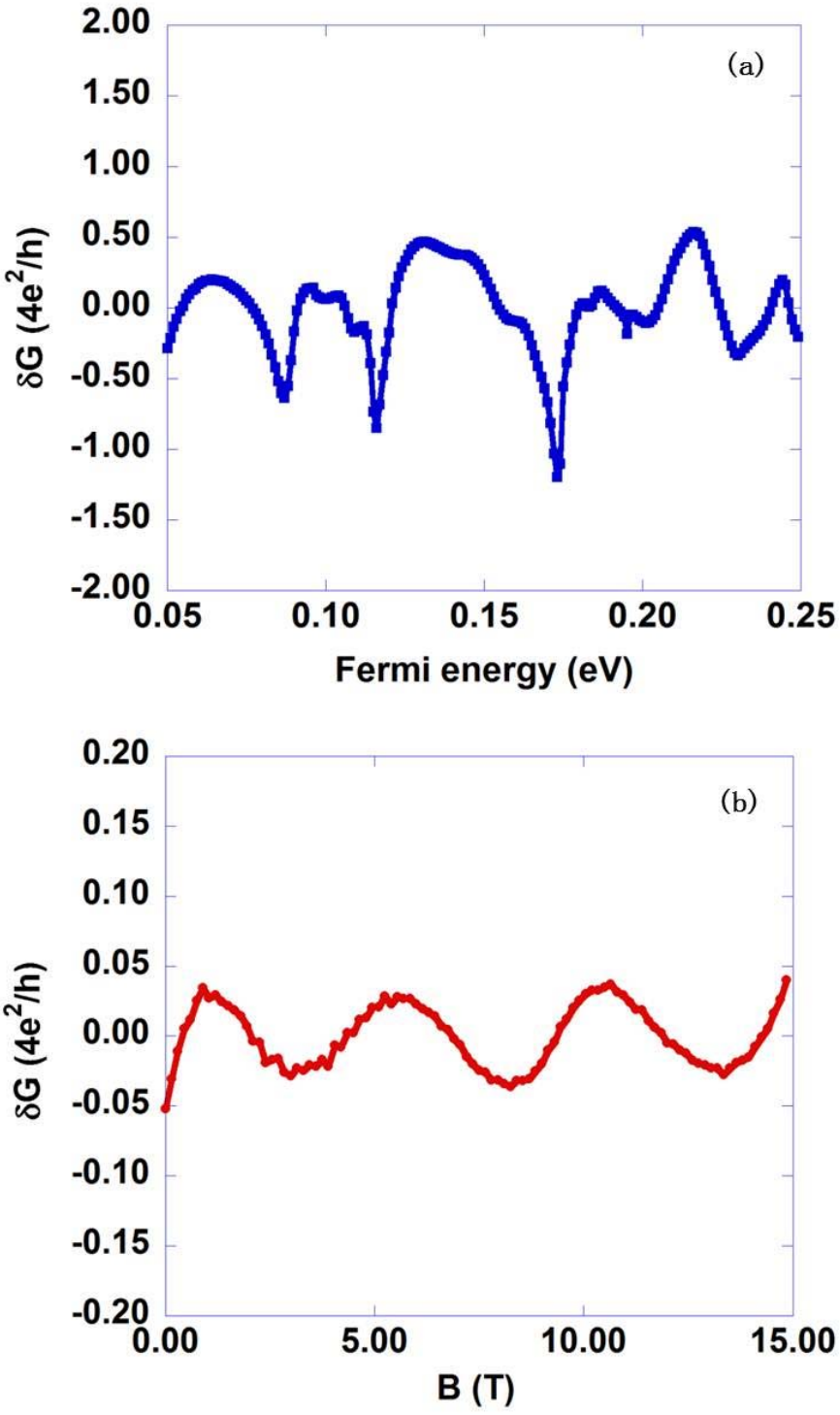

Fig. 5.11 (a) δG as a function of Fermi energy at B=0T for a peak-to-peak disorder amplitude Vpp of 2.8eV. (b) δG as a function of magnetic fields at Fermi energy of 250meV, for peak-to-peak disorder amplitude Vpp of 2.8eV[57].

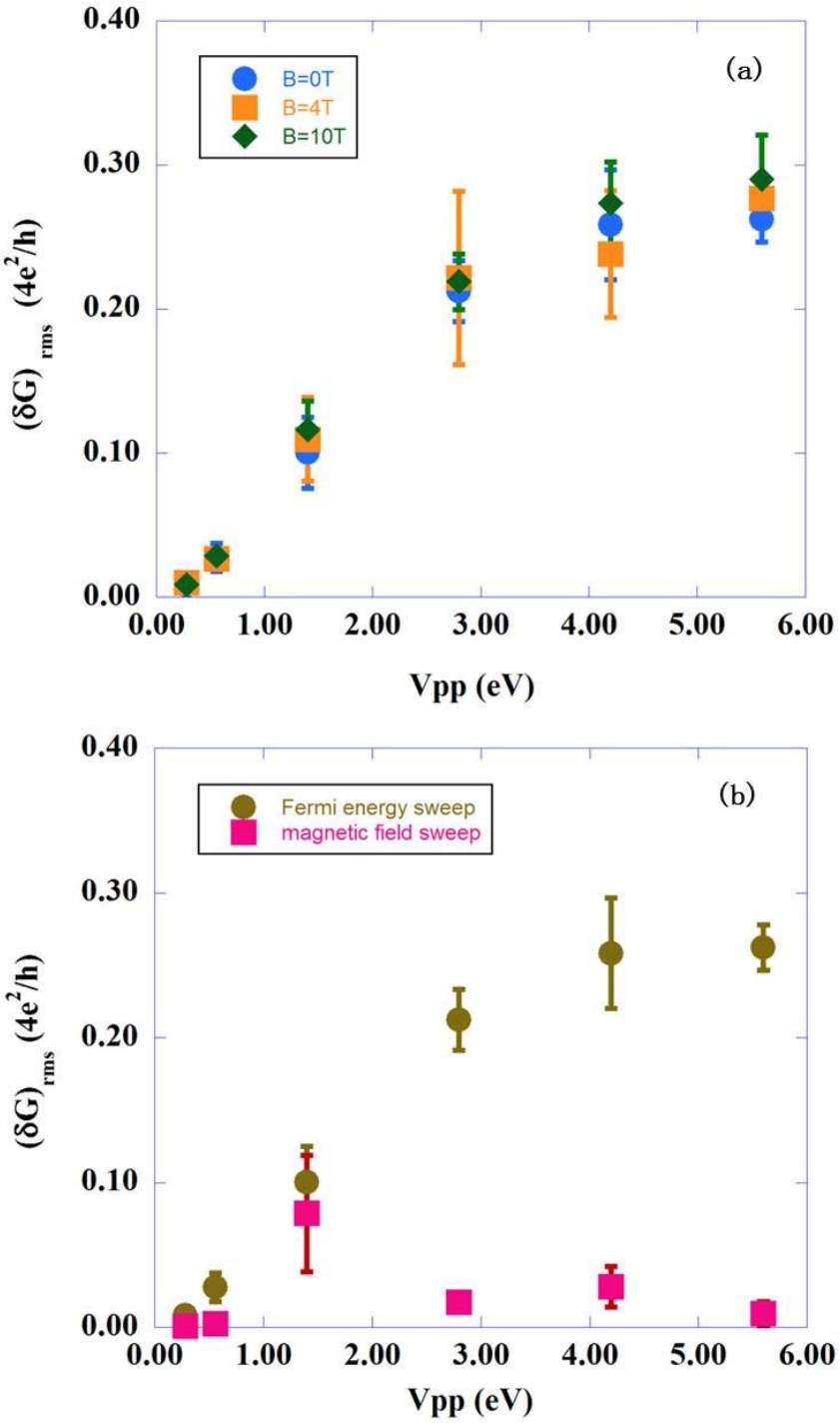

Fig. 5.12 (a) δG(rms) as a function of peak-to-peak disorder amplitude Vpp for Fermi energy sweeps at B=0T, 4T and 10T. (b) δG(rms) as a function of peak-to-peak disorder amplitude Vpp for Fermi energy sweeps (B=0T) and magnetic field sweeps (Fermi energy is 250meV) [57].

5.5 Conclusions

The RMS values of δG as a function of Fermi energy and magnetic field at different short-range disorder amplitude are calculated for several different samples and the statistical results are presented in Fig. 5.12 [57]. Fig. 5.12 (a) illustrates the dependence of RMS of δG on peak-to-peak values of random potential for Fermi energy sweeps at B=0T, 4T and 10T [57]. A maximum value of around $0.3(4e^2/h)$ is reached as the peak-to-peak value of disorder amplitudes increase to 5.6eV [57]. The overlapping of the 3 curves of 0, 4 and 10T implies that the magnetic field does not have any significant effect on the values of δG (RMS) in the presence of short-range disorder [57].

Fig. 5.12 (b) presents the comparison of δG (RMS) values for Fermi energy sweeps and magnetic field sweeps [57]. Once the peak-to-peak values of random potential amplitudes are larger than 1.4 eV, the values of δG (RMS) for Fermi energy sweeps are much higher than for magnetic field sweeps [57]. The results in Fig. 5.12 imply a violation of ergodicity in graphene nanoribbons [57]. Similar results were found for GaAs in Chapter 2.

In summary, the conductance fluctuations for several different graphene nanoribbon samples were investigated numerically in the presence of a short-range disorder potential. The statistical results indicate that the universality assumed earlier fails here because the amplitudes of fluctuations depend on the peak-to-peak values of random potential [57]. I will return to this discussion of universality in the final chapter. In addition, the results show that the amplitudes of fluctuations for Fermi energy sweeps are higher than the amplitudes of fluctuations for magnetic field sweeps [57]. This means that the hypothesis of ergodicity does not hold here. It is also found that the amplitudes of

fluctuations for Fermi energy sweeps at different magnetic fields do not have much difference in the case of short-range disorder [57]. This feature will be examined further in the next chapter using long-range disorder.

CHAPTER 6

GRAPHENE NANORIBBONS IN THE PRESENCE OF LONG-RANGE DISORDER

6.1 Introduction

In this chapter, the conductance fluctuations in graphene nanoribbons in the presence of long-range disorder are investigated [58,59]. The remote charge impurity induced long-range disorder model is presented in the first section. The long-range disorder potential landscape is mapped onto the simulation region and I use the computational techniques introduced in chapter 4 to calculate the conductance of graphene nanoribbons [51, 52, 53, 56]. The conductance fluctuations are computed for both Fermi energy sweeps and magnetic field sweeps. A polynomial fit is used to obtain the background conductance and this is subtracted from the conductance in order to isolate the fluctuations. The root-mean-square values of the conductance fluctuations are computed at different magnetic field for Fermi energy sweeps and at different Fermi energies for magnetic field sweeps. I use several samples with different distributions of impurities in order to obtain a statistical result for the root-mean-square values of conductance fluctuations [59].

This chapter is organized as follows. The remote-charge impurity disorder potential landscape is developed in section 6.2. The calculation of conductance for Fermi energy sweeps and magnetic field sweeps and the polynomial fit to conductance is given in section 6.3. Then the δG (RMS) values for Fermi energy sweeps and magnetic field sweeps are discussed in section 6.4. Finally, the conclusions of rms values of amplitude of fluctuations for Fermi energy sweeps and magnetic fields sweeps using several different samples are summarized in section 6.5.

6.2 The model of long-range disorder potential

The properties of conductance fluctuations in graphene nanoribbons with the presence of long-range impurities are discussed in this chapter. As we know, investigation of conductance fluctuations and scattering mechanisms in graphene nanoribbons with disorder potential is a fundamental physical topic in understanding how the long-range disorder affects the transport properties in Dirac materials [54, 58]. Generally speaking, the fluctuation of conductance arises from interference of electron waves scattered by the long-range disorder [17]. Here, I use an atomic-based tight-binding model to build the Hamiltonian and then use the recursive scattering matrix method to calculate the conductance of graphene nanoribbons with armchair edges in the presence of this long-range potential [56, 57, 59].

The building of a long-range remote charge impurity potential can be started with the introduction of the static Coulomb potential of a point impurity charge, which can be expressed as [15, 59]

$$V(r) = \frac{1}{4\pi\varepsilon_0\varepsilon_r}\frac{e}{r}. \tag{6.1}$$

Here, e is the elementary electric point charge, r is the distance between the point charge and the position where the electric potential $V(r)$ is calculated, ε_0 is the vacuum permittivity, and the relative permittivity is ε_r. If the screening effect of Debye form is involved, the screened potential of a point impurity charge will have a real-space expression [15, 59]

$$V(r) = \frac{1}{4\pi\varepsilon_0\varepsilon_r}\frac{e}{r}\exp(-\xi r). \tag{6.2}$$

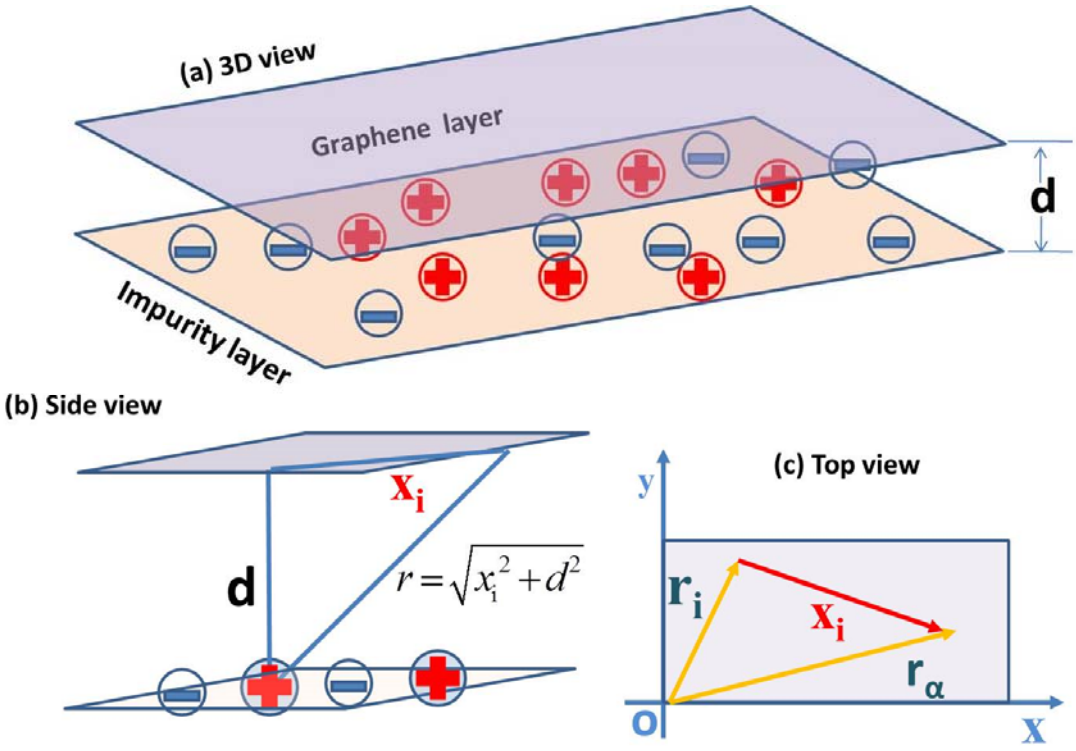

Fig. 6.1 (a) Typical 3D view of a remote charge impurity. The distance between the graphene layer and the impurity layer is *d* and the positive and negative impurity charges are randomly located within the impurity layer. (b) Side view. The distance between the impurity charge and the point where potential is calculated is *r*. (c) Top view. The distance between the impurity charge and the point where potential is calculated is obtained by r_i-r_α. [59]

The exponential term *exp(-ξr)* represents the modification of potential by the screening effect, and ξ is the screening coefficient [15, 58, 59].

As it is shown in Fig. 6.1, the distance between the point charge and the position where potential *V(r)* is calculated can be expressed as $r=\sqrt{x_i^2+d^2}$, in which $x_i=|r_\alpha-r_i|$. Considering the superposition principle, the total electric potential of all impurity charges is simply the sum of potentials due to individual impurity charges, which can be written in a form

$$V_\alpha = \sum_{i=1}^{N_i} \frac{1}{4\pi\varepsilon_0\varepsilon_r} \frac{e}{\sqrt{|r_\alpha - r_i|^2 + d^2}} \exp\left(-\xi \cdot \sqrt{|r_\alpha - r_i|^2 + d^2}\right). \tag{6.3}$$

Here, N_i is the number of the impurities. Other parameters in the above equations are indicated in Fig. 6.1 [15, 59].

Next, I introduce the physical parameters of the simulation. The graphene nanoribbon sample used in calculation has a width of 199 atoms and length of 200 columns (100 slices). So the area of the sample will be around 24.3 nm (wide) × 42.4 nm (long) = 1030.32 nm^2. I consider an impurity charge density of 3×10^{12} cm^{-2}. Then, the number of impurity charges in the area of the sample is approximately 31. By using the random number generator, a randomized distribution of impurity charges can be produced across the graphene nanoribbon. In addition, the distance between the graphene layer and the impurity charge layer is set to $d = a_0$ and the screening coefficient is taken to be $\xi = 1/(10 \times a_0)$, corresponding to a screening length of $10 \times a_0$. Here, $a_0 = 0.142$ nm is the distance between two carbon atoms in graphene [59].

Based on the parameters given above, a typical remote charge impurity random potential landscape is plotted in Fig. 6.2. Fig. 6.2 (a) is the 3D plot of remote charge impurity disorder potential and Fig. 6.2 (b) is the 2D plot of a remote charge impurity disorder potential. An approximate analytical calculation of the peak value of potential energy for one charge impurity is

$$\begin{aligned} \mathrm{E}_r(eV) &= \frac{1}{4\pi\varepsilon_0\varepsilon_r} \frac{e}{a_0} \exp\left(-\frac{1}{10a_0}\sqrt{a_0^2}\right) \\ &= \frac{3.7\times10^{-10} eV \cdot m}{1.42\times10^{-10} m} \exp(-0.1) = 2.3575 eV \end{aligned}. \tag{6.4}$$

It can be found that the value of E_r is very close to the peak values of potential energy shown in the plots in Fig. 6.2.

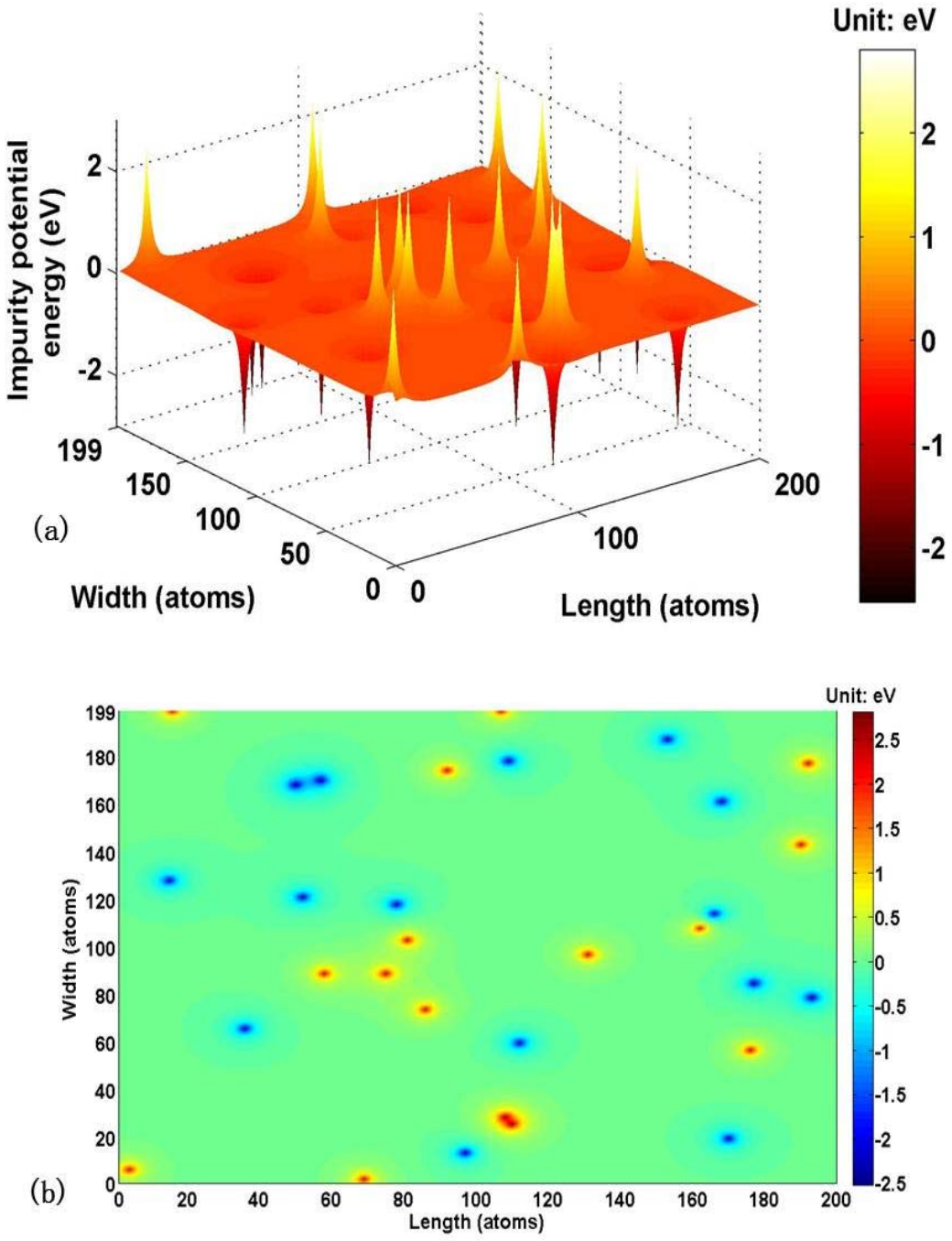

Fig. 6.2 (a) 3D plot of remote charge impurity disorder potential landscape. (b) 2D plot of remote charge impurity disorder potential landscape [59].

6.3 δG vs Fermi energy and magnetic field

Using the long-range impurity-induced potential described above, I study the conductance fluctuations in the disordered graphene nanoribbon for both Fermi energy sweeps and magnetic field sweeps. In Fig. 6.3(a), the conductance as function of Fermi energy is plotted for ballistic and disordered graphene nanoribbon over a range of Fermi energy at zero magnetic fields. The conductance as a function of magnetic field, with and without a disorder potential, is shown at a Fermi energy of 95 meV in Fig. 6.3(b). At this Fermi energy, there are 2 propagating modes for zero magnetic field, and the number of propagating modes drops to 1 when the magnetic field increases to about 12 T [59].

In order to calculate the RMS values of the conductance fluctuations, I use a polynomial fit to obtain the background conductance and this is subtracted from the fluctuations. The polynomial fitting curves are shown in Fig.6.4. The polynomial fitting curves are marked in each figure [59].

After the fit is subtracted, the net conductance δG as function of Fermi energy and magnetic field are plotted in Fig. 6.5. The RMS values of the conductance fluctuation for Fermi energy sweep and magnetic field sweep are both calculated, and found to be $0.317(4e^2/h)$ for the former and $0.085(4e^2/h)$ for the latter. It is obvious that the RMS values of the fluctuations for magnetic field sweeps is smaller than that of Fermi energy sweeps, although the latter are close to the results I obtained in calculations of fluctuations in short-range disordered graphene nanoribbons [57]. It indicates a failure of ergodicity in the conductance fluctuations in graphene nanoribbons in the presence of long-range impurity disorder [46, 59].

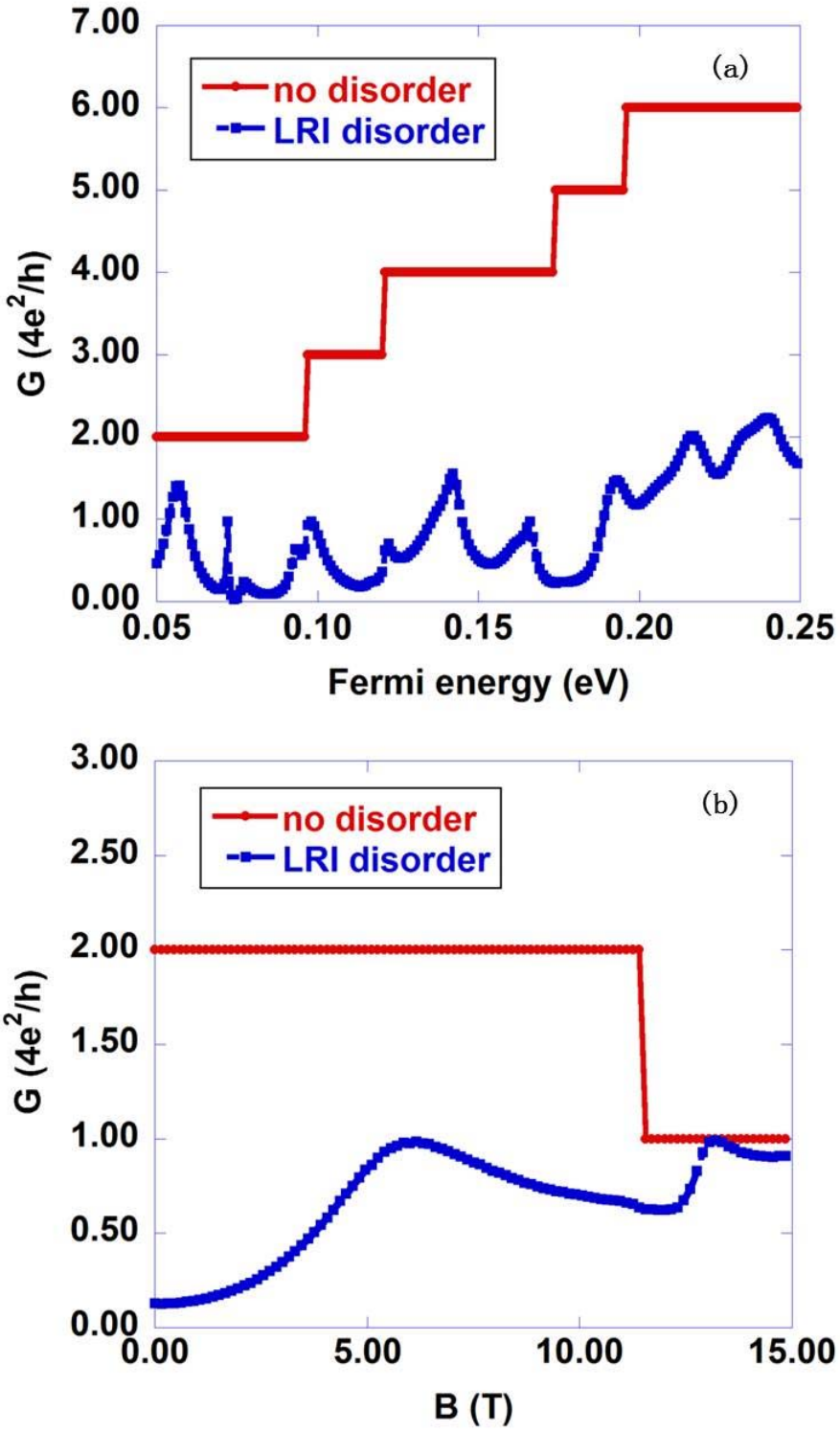

Fig. 6.3 (a) Conductance as a function of Fermi energy at a magnetic field of 0 T for clean nanoribbon and disordered nanoribbon. (b) Conductance as function of magnetic field from at a Fermi energy of 95 meV for clean nanoribbon and disordered nanoribbon [59].

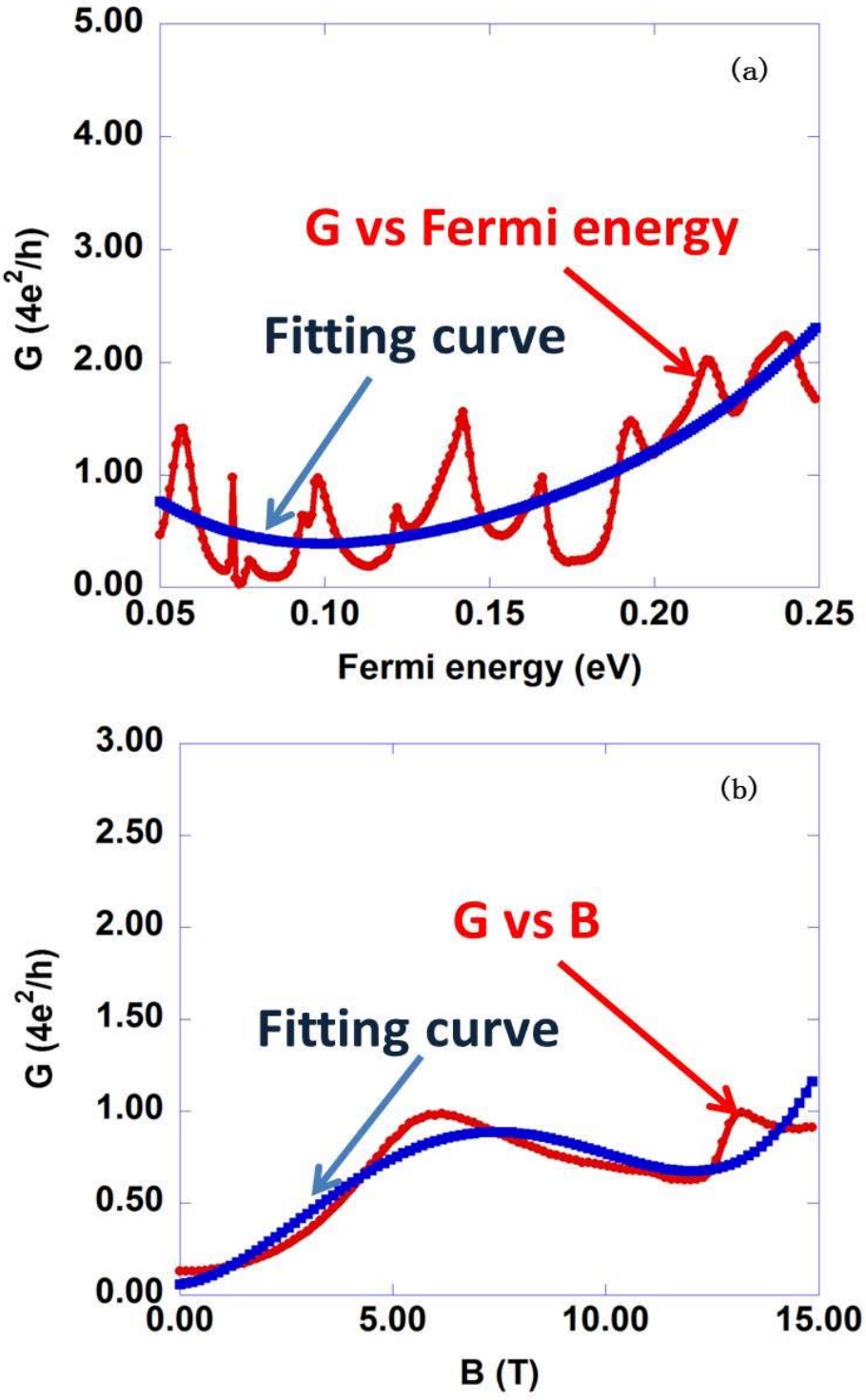

Fig. 6.4 (a) Conductance fluctuation as function of Fermi energy and its polynomial fitting curve. (b) Conductance fluctuation as function of magnetic field and its polynomial fitting curve [59].

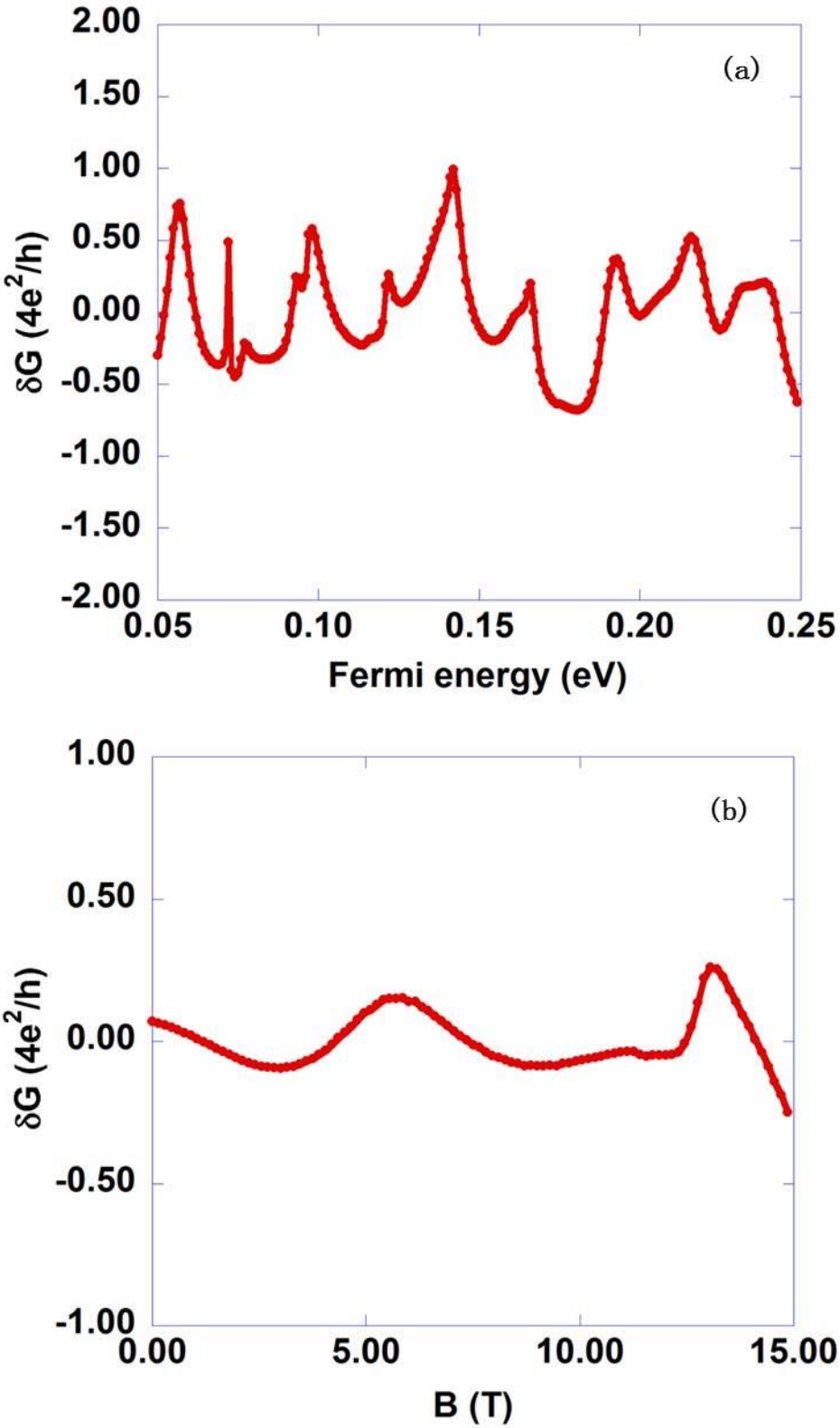

Fig. 6.5 (a) G as a function of Fermi energy at a magnetic field of 0 T. (b) δG as a function of magnetic field at a Fermi energy of 95 meV [59].

6.4 δG (RMS) vs magnetic field or Fermi energy

I now turn to investigate δG (RMS) for Fermi energy sweeps at different magnetic fields and δG (RMS) of magnetic field sweeps at different Fermi energies. The conductance fluctuation for a Fermi energy sweep is plotted for a range of magnetic fields in Fig. 6.6(a). The various conductances are shifted up a small increment for each magnetic field in order to avoid overlapping of the curves. The conductance fluctuations for magnetic field sweeps are plotted for a range of Fermi energies in Fig. 6.6(b). Again, the conductances are shifted up for each Fermi energy for clarity [59].

One remarkable feature that can be observed in Fig. 6.6(a) is that the fluctuations are getting weaker as the magnetic field increases. To examine this behavior quantitatively, I calculated the δG (RMS) values of each fluctuation curve in Fig.6.6. The results are plotted in Fig. 6.7. Fig. 6.7(a) shows the δG (RMS) values of the conductance fluctuations for Fermi energy sweeps as a function of the magnetic field. In, Fig. 6.7(b) the δG (RMS) values of conductance fluctuations for magnetic field sweeps are plotted as a function of the Fermi energy. It can be observed that, in Fig. 6.7(a), the value of δG (RMS) drops from 0.32 to 0.23 as magnetic field increases from 0T to 13T, which means that the fluctuation amplitude is compressed by magnetic field [46, 59].

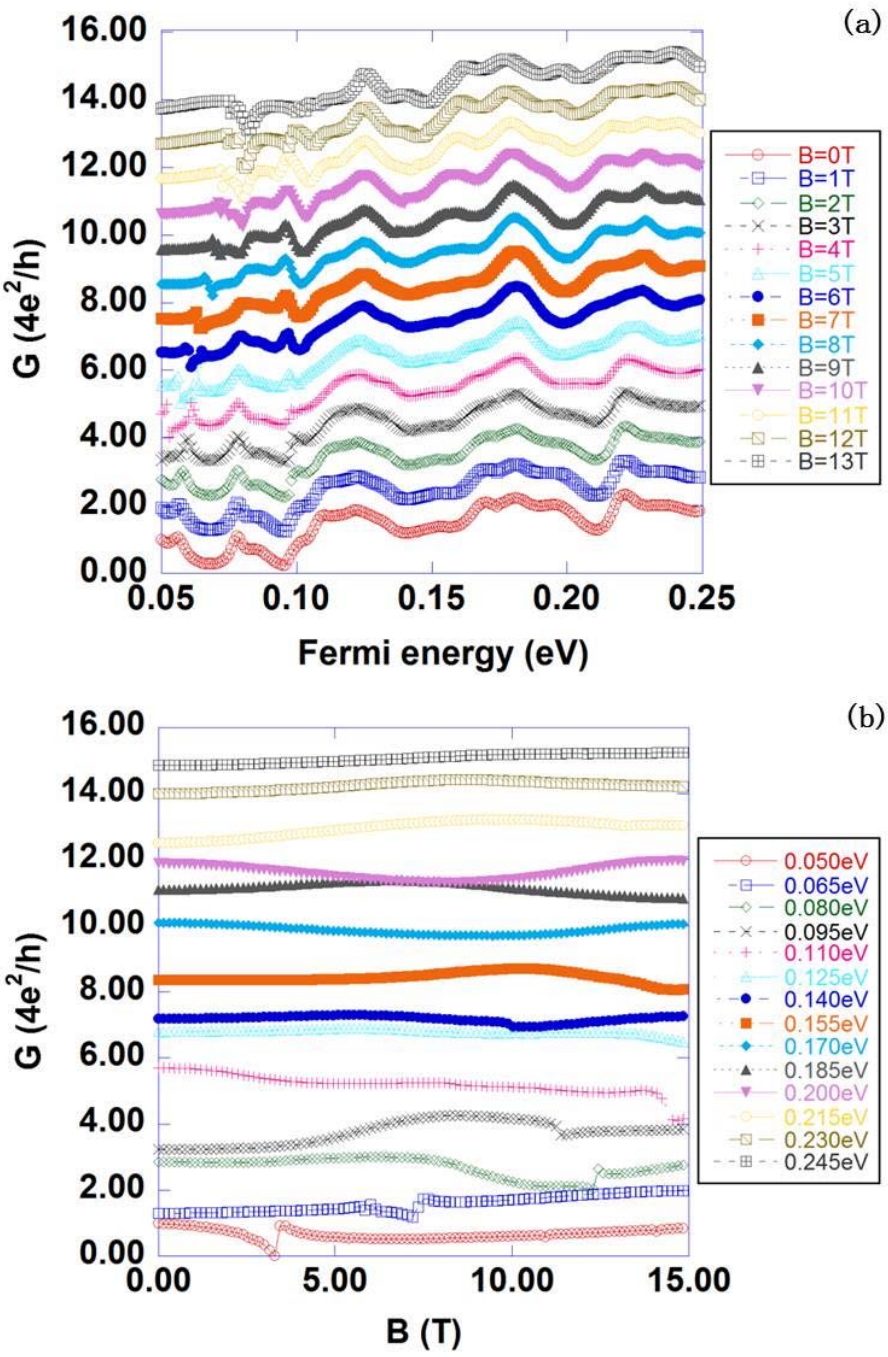

Fig. 6.6 (a) Conductance fluctuations for Fermi energy sweeps at various magnetic fields. (To aid clarity, curves are shifted up by i ($4e^2/h$) for B= i (T)) (b) Conductance fluctuations for magnetic field sweeps at various Fermi energies. (To aid clarity, curves are shifted up by i ($4e^2/h$) for Fermi energy=$50+i\times15$ (meV)) [59].

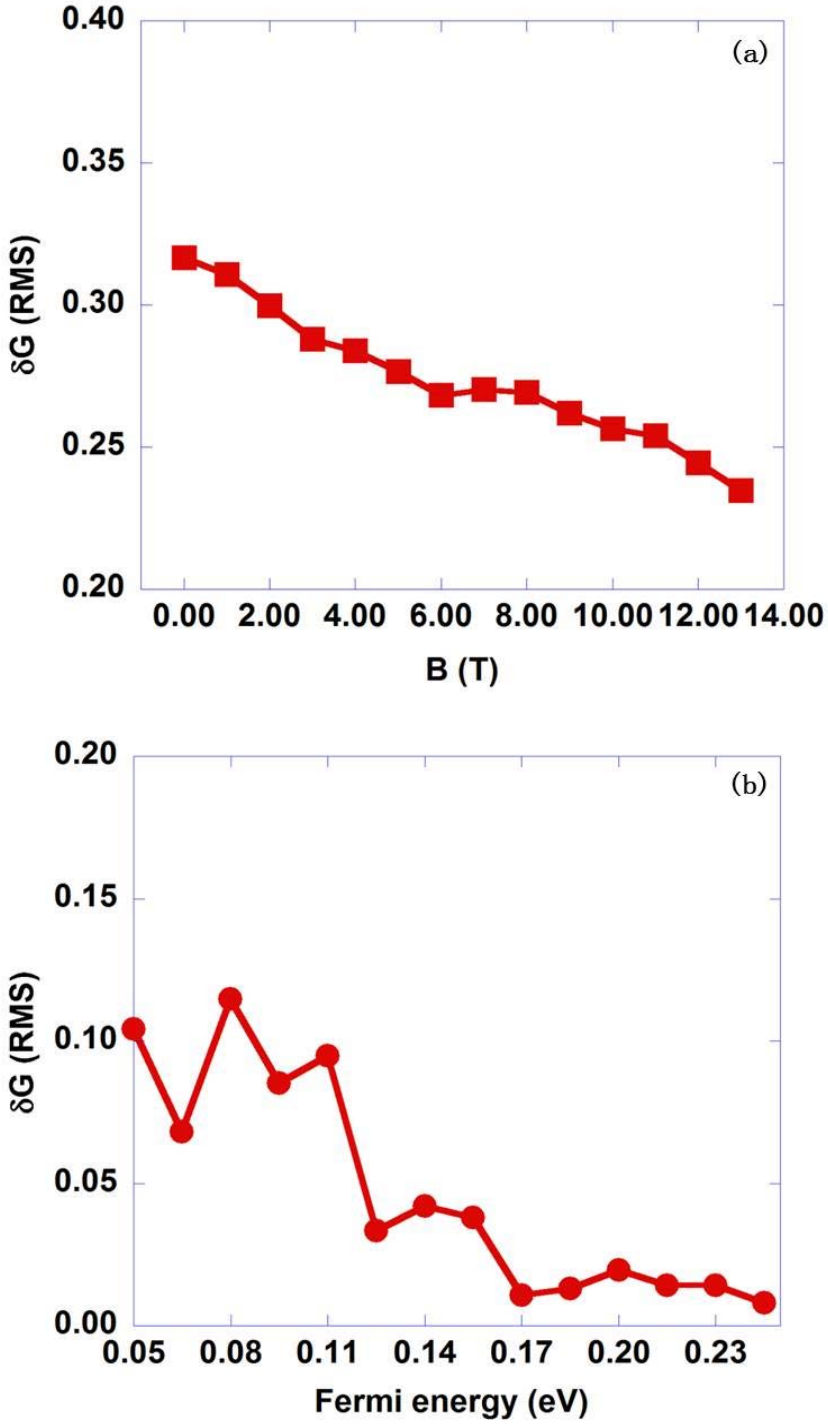

Fig. 6.7 (a) δG(RMS) for Fermi energy sweeps as a function of magnetic field. (b) δG(RMS) for magnetic field sweeps as a function of Fermi energy [59].

Another feature is that the δG (RMS) values of fluctuations for magnetic field sweeps at different Fermi energies shown in Fig. 6.7(b) are smaller than those for Fermi energy sweeps shown in Fig. 6.7(a). This behavior indicates that the hypothesis of ergodicity does not hold in graphene with long-range disorder [19]. And in Fig. 6.7(b), the δG (RMS) values for magnetic field sweeps have a higher value of $0.1(4e^2/h)$ for lower Fermi energies and decreases to as low as $0.01(4e^2/h)$ at the higher energies (densities), which is close to the results that I have obtained in short-range impurity disorder induced fluctuations [57, 59].

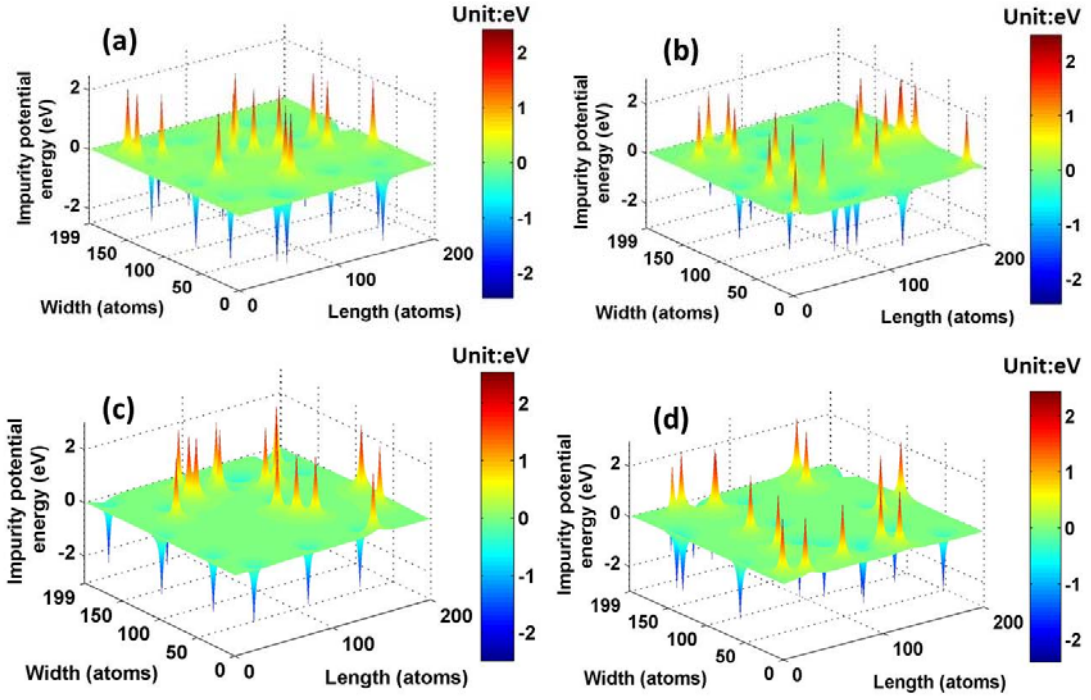

Fig. 6.8 Four different graphene nanoribbon samples with remote charge impurity random potentials, indicated with (a), (b), (c) and (d) [59].

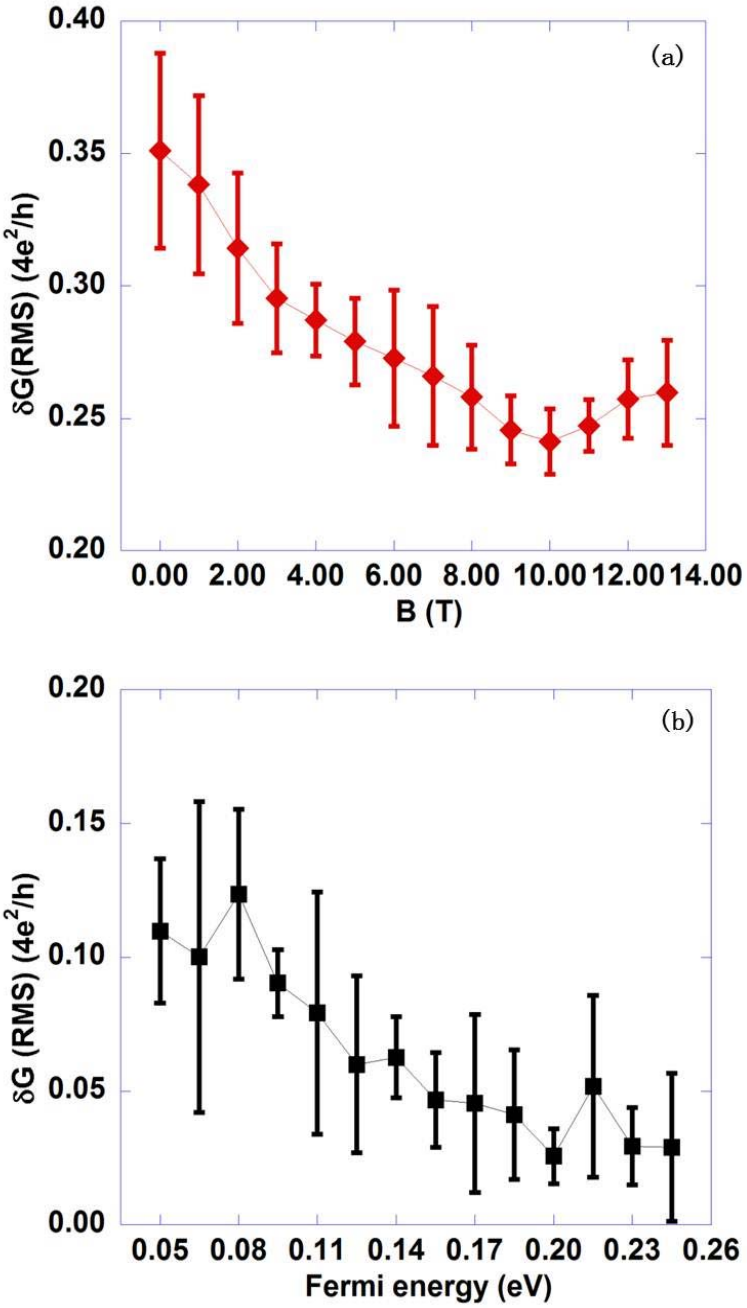

Fig. 6.9 (a) Statistical results of δG (RMS) for Fermi energy sweeps as function of magnetic field for 4 different samples. (b) Statistical results of δG (RMS) for magnetic field sweeps as a function of Fermi energy for 4 different samples [46, 59].

6.5 Conclusions

In this section, some conclusions that can be drawn from the results obtained above will be summarized briefly in the following. Since the distribution patterns of impurity charges are different from sample to sample, I also considered the dependence of δG (RMS) vs magnetic field or Fermi energy on sample differences in my investigation. I use 4 samples which have the same impurity density of $3\times10^{12}cm^{-2}$ but different distribution patterns, as shown in Fig. 6.8 (a), (b), (c) and (d), to calculate the values of δG (RMS) as a function of magnetic field and Fermi energy for each of them, respectively [59].

Fig. 6.9(a) presents the statistical results of δG (RMS) for Fermi energy sweeps as a function of magnetic fields for the 4 different samples. Fig. 6.9(b) is the statistical results of δG (RMS) for magnetic field sweeps as a function of Fermi energy for 4 different samples. It is obvious that, in Fig. 6.9(a), the δG (RMS) for Fermi energy sweeps is decreased by magnetic field. Over the range shown, the value of δG (RMS) drops from $0.35(4e^2/h)$ to $0.24(4e^2/h)$. Values of δG (RMS) for magnetic field sweeps are basically between 0 and $0.15(4e^2/h)$ for different Fermi energies, as shown in Fig. 6.9 (b). These latter values are lower than those for Fermi energy sweeps in Fig. 6.9 (a). The calculation results obtained in this thesis chapter show a failure of the hypothesis of ergodicity and universality in graphene nanoribbons in the presence of long-range disorder [46, 59].

CHAPTER 7

CONCLUSION AND PERSPECTIVE

This thesis work numerically addresses the problems as to whether or not universality and ergodicity of conductance fluctuations hold in GaAs nanowires and graphene nanoribbons at low temperature [17, 18, 51, 56, 57, 59].

For GaAs nanowires [51], many samples with different sizes were used to study the conductance fluctuations. The conductance is calculated for both Fermi energy sweeps and magnetic field sweeps in both the parabolic band regime and the quasi-linear band regime. There are no significant differences between the results of parabolic band and quasi-linear band within the statistical errors. The root-mean-square values of δG are calculated for disorder potentials with different peak-to-peak amplitudes. As the peak-to-peak values of the disorder increase, the root-mean-square values of δG for Fermi energy sweeps will reach a saturation value of around $0.35(2e^2/h)$ and the rms values of δG for magnetic field sweeps will reach value of $0.15(2e^2/h)$ in the saturation regime. Since the saturation δG values of Fermi energy sweeps are generally larger than that of magnetic field sweeps and δG varies with the disorder amplitude, these results indicate a deviation of the conductance fluctuations from both universality and ergodicity in GaAs nanowires [19].

The effect of a magnetic field on the amplitudes of conductance fluctuations for Fermi energy sweeps also was studied in GaAs nanowires by using both weak and strong disorder potentials. The results show that the amplitude of conductance fluctuations of Fermi energy sweeps is reduced as the perpendicular magnetic field is increased. Because of the edge state formation near the edges of the GaAs nanowires, the scattering events

are reduced near the edges. Hence, the fluctuations for a perpendicular magnetic field have reduced amplitudes compared with the case without a magnetic field [46].

After the investigation on GaAs nanowires, I turn to the study of conductance fluctuations in graphene nanoribbons [54]. The atomistic-basis tight-binding model is used to establish the slice Hamiltonian of graphene nanoribbons with armchair edges [56]. Then, the Hamiltonians are integrated into the generalized transfer matrix equations. The conductance is calculated by the recursive scattering matrix technique [52]. A perpendicular magnetic field is also incorporated into the calculation. The conductance fluctuations arise with the incorporation of a disorder potential. In this thesis, conductance fluctuations from both short-range disorder [57] and long-range disorder [59] were investigated.

For short-range disorder in graphene nanoribbons [57], the root-mean-square values of δG for Fermi energy sweeps were calculated for several different samples at different amplitudes of the disorder potential. The Fermi energy sweeps were made for magnetic fields of 0T, 4T and 10T. The three curves of the δG rms values, as a function of the random potential amplitudes overlapped with one another, indicating that the magnetic field does not have any effect on the amplitude of fluctuations in the presence of short-range disorder. But the dependence of the rms values of δG on the random potential amplitudes shows a deviation from universality in graphene nanoribbons. In addition, from comparison results of δG (RMS) values for Fermi energy sweeps and magnetic field sweeps, it was observed that the values of δG (RMS) for Fermi energy sweeps are higher than the values of magnetic field sweeps, which implies a violation of ergodicity in graphene nanoribbons [57].

For long-range disorder in graphene nanoribbons [59], several different configurations of impurities in the samples are considered in the calculation of conductance fluctuations. The statistical results of δG (RMS) of Fermi energy sweeps as function of magnetic fields and the statistical results of δG (RMS) of magnetic field sweeps as function of Fermi energies were compared and it was found that values of δG (RMS) for magnetic field sweeps are lower than the values of δG (RMS) for Fermi energy sweeps. Again, this shows a failure of the hypothesis of ergodicity in the presence of long-range disorder in graphene nanoribbons [18, 46]. Moreover, the δG (RMS) of Fermi energy sweeps is reduced as the magnetic field increased from 0T to 10T. In this case, the value of δG (RMS) drops from $0.35(4e^2/h)$ to $0.24(4e^2/h)$. This effect can also be explained by the formation of edge states near the edges of graphene nanoribbons, which is similar to the situation in GaAs nanowires for a perpendicular magnetic field. This suppression of the fluctuation amplitude by a magnetic field in graphene nanoribbons agrees qualitatively with the experimental results [46, 59].

There are still some questions to be addressed in the future. Firstly, the atomistic basis simulations here show good performance for studying devices of small sizes, but when the device size gets larger, it becomes quite time-consuming. The principle graphene nanoribbon size used here was 24nm×42nm in my calculation, which is smaller than the real size of a graphene flake in experiment [46]. While large sizes were used to check the result, most of the data arises from this smaller sample size. In future work, one could consider using a finite difference method, which allows a larger grid size to solve the relativistic Dirac equation [60]. One could then simulate nanoribbons with sizes close to the experimental flakes. Secondly, this thesis work is limited to the investigation

of conductance fluctuations in monolayer graphene. Future work can be extended to bilayer, trilayer and multilayer graphene devices [54]. Finally, for smaller samples, other approaches, such as the empirical pseudopotential method and density functional theory [61], can be considered for studying conductance fluctuations in graphene.

REFERENCES

[1] D. K. Ferry, Quantum mechanics: an introduction for device physicists and electrical engineers. Institute of Physics Pub, Bristol, UK (1995)

[2] Y. Aharonov and D. Bohm, Significance of electromagnetic potentials in the quantum theory, Physical Review, Volume 115, Issue 3, pp. 485 – 491 (1959)

[3] R. G. Chambers, Shift of an electron interference pattern by enclosed magnetic flux, Physical Review Letters, Volume 5, Issue 1, pp. 3 – 5 (1960)

[4] R. A. Webb, S. Washburn, C. P. Umbach, R. B. Laibowitz, Observation of h/e Aharonov-Bohm Oscillations in Normal-Metal Rings, Physical Review Letters, Volume 54, Issue 25, pp. 2696 – 2699 (1985)

[5] P. M. Mankiewich, et al. Observation of Aharonov-Bohm effect in quasi-one-dimensional GasAs/AlGaAs rings. J. Vac. Sci. Technol. B 6, 13-133 (1988)

[6] Richard P. Feynman, Robert B. Leighton, Matthew L. Sands. The Feynman Lectures on Physics, Vol. 3. (1965)

[7] Jed Z. Buchwald, The rise of the wave theory of light: optical theory and experiment in the early nineteenth century, University of Chicago Press (1989)

[8] R. Landauer, Spatial variation of currents and fields due to localized scatterers in metallic conduction, Journal of Mathematical Physics, volume 37, issue 10, pp. 223 – 231 (1996)

[9] Y. V. Nazarov, Ya. M. Blanter, Quantum transport: Introduction to Nanoscience. Cambridge University Press. (2009)

[10] B. J. van Wees et al. Quantized conductance of point contacts in a two-dimensional electron gas, Physical Review Letters 60 (9): 848–850. (1988)

[11] N. Aoki, A. Burke, C. R. da Cunha, R. Akis, D. K. Ferry, Y. Ochiai, Study of quantum point contact via low temperature scanning gate microscopy, Journal of Physics: Conference Series, Volume 38, Issue 1, pp. 79 – 82 (2006)

[12] H. van Houten and C.W.J. Beenakker, Quantum point contacts, Physics Today 49 (7): 22–27. (1996)

[13] David K. Ferry and Carlo Jacoboni, Quantum transport in semiconductors, Plenum Press (1992)

[14] Supriyo Datta, Electronic transport in mesoscopic systems, Cambridge University Press, (1995)

[15] John H. Davies. The physics of low-dimensional semiconductors: an introduction. Cambridge University Press (1998)

[16] A. Grincwajg, G. Edwards, D. K. Ferry, Conductance fluctuations in microstructures: crossover between different transport regimes. Phys. B 218, 92 (1996)

[17] D. K. Ferry, S. M. Goodnick, J. P. Bird, Transport in Nanostructures, 2nd edn. Cambridge University Press, Cambridge (2009)

[18] P. A. Lee, A. D. Stone, Universal conductance fluctuations in metals. Phys. Rev. Lett. 55, 1622 (1985)

[19] P. A. Lee, A. D. Stone, H. Fukuyama, Universal conductance fluctuations in metals: effects of finite temperature, interactions, and magnetic field. Phys. Rev. B 35, 1039 (1987)

[20] C. W. J. Beenakker and H. van Houten, Quantum Transport in Semiconductor Nanostructures, Solid State Physics - Advances in Research and Applications, Volume 44, Issue C, pp. 1 – 228 (1991)

[21] C. P. Umbach, S. Washburn; R. B. Laibowitz, R. A. Webb, Magnetoresistance of small, quasi-one-dimensional, normal-metal rings and lines, Physical Review B, Volume 30, Issue 7, pp. 4048 – 4051 (1984)

[22] D. E. Beutler, T. L. Meisenheimer, N. Giordano, Resistance Fluctuations in Thin Bi Wires and Films, Physical Review Letters, Volume 58, Issue 24, p. 2608 (1987)

[23] R. A. Webb, S. Washburn, C.P. Umbach, Experimental study of nonlinear conductance in small metallic samples, Physical Review B, Volume 37, Issue 14, pp. 8455 - 8458 (1988)

[24] D. C. Ralph, K. S. Ralls, and R. A. Buhrman, Ensemble studies of nonlinear conductance fluctuations in phase coherent samples, Physical Review Letters, Volume 70, Issue 7, pp. 986 – 989 (1993)

[25] Roland Schäfer, Klaus Hecker, Helmut Hegger, Wolfram Langheinrich, Experimental study of mesoscopic fluctuations in nonlinear conductance and magnetoconductance, Physical Review B, Volume 53, Issue 23, pp. 15964 - 15970 (1996)

[26] E. Scheer, H. v. Löhneysen, A. D. Mirlin, P. Wölfle, H. Hein, Angular Dependence of Universal Conductance Fluctuations in Noble-Metal Nanowires, Physical Review Letters, Volume 78, Issue 17, pp. 3362 – 3365 (1997)

[27] R. Häussler, E. Scheer, H. B. Weber, H. v. Löhneysen, Conductance oscillations in mesoscopic rings: Microscopic versus global phase, Physical Review B, Volume 64, Issue 8 (2001)

[28] Jing-Zhe Chen, Jin Zhang, Ru-Shan Han, First Principles Calculation of Universal Conductance Fluctuation in Monatomic Metal Chains, Chinese Physics Letters, Volume 25, Issue 3, pp. 1060 – 1063 (2008)

[29] S Lee, A Trionfi, D Natelson, Quantum coherence in a ferromagnetic metal: Time-dependent conductance fluctuations, Physical Review B, Volume 70, Issue 21 (2004)

[30] W. E. Howard, F. F. Fang, Low temperature effects in Si FETs, solid-state electronics, Vol. 8, pp. 82-83. (1965)

[31] A. B. Fowler, A. Hartstein, R. A. Webb, Conductance in Restricted-Dimensionality Accumulation Layers, Physical Review Letters, Volume 48, Issue 3, pp. 196 - 199 (1982)

[32] W. J. Skocpol, Magnetoconductance and quantized confinement in narrow silicon inversion layers, Surface Science, Volume 142, Issues 1–3, Pages 14–18 (1984)

[33] R. F. Kwasnick, M. A. Kastner, J. Melngailis, and P. A. Lee, Nonmonotonic Variations of the Conductance with Electron Density in □70-nm-Wide Inversion Layers, Phys. Rev. Lett. 52, 224 (1984)

[34] W. J. Skocpol, L.D. Jackel, R. E. Howard, P. M. Mankiewich, D. M. Tennant, Quantum transport in narrow MOSFET channels, Surface Science, Volume 170, Issues 1–2, Pages 1–13 (1986)

[35] S. B. Kaplan, A. Hartstein, Universal Conductance Fluctuations in Narrow Si Accumulation Layers, Physical Review Letters, Volume 56, Issue 22, pp. 2403 – 2406 (1986)

[36] W. J. Skocpol, Conductance Fluctuations in Narrow Silicon MOSFETs, Physica Scripta, Volume 1987, pp. 95 - 101(1987)

[37] S. B. Kaplan, Asymmetric conductance and coherence effects in mesoscopic Si metal-oxide-semiconductor field-effect transistors, Physical Review B, Volume 38, Issue 11, pp. 7558 - 7567(1988)

[38] T. J. Thornton, M. Pepper, H. Ahmed, Universal conductance fluctuations and electron coherence lengths in a narrow two-dimensional electron gas, Physical Review B, Volume 36, Issue 8, pp. 4514 - 4517(1987)

[39] P. Debray, and J.-L. Pichard, Reduction of mesoscopic conductance fluctuations due to Zeeman splitting in a disordered conductor without spin-orbit scattering, Physical Review Letters, Volume 63, Issue 20, pp. 2264 - 2267(1989)

[40] S. J. Klepper, O. Millo, M. W. Keller, D. E. Prober, R. N. Sacks, Sensitivity of conductance fluctuations to the addition of single elastic scatterers in mesoscopic GaAs/AlxGa1−xAs heterostructures, Physical Review B, Volume 44, Issue 15, pp. 8380 - 8383(1991)

[41] C. V. Brown, A. K. Geim, T. J. Foster, C. J. G. M. Langerak, P. C. Main, Mesoscopic fluctuations in high magnetic fields: Change in behavior due to boundary diffusion, Physical Review B, Volume 47, Issue 16, pp. 10935 - 10938 (1993)

[42] S. V. Morozov, K. S. Novoselov, M. I. Katsnelson, F. Schedin, L. A. Ponomarenko, D. Jiang, and A. K. Geim, Strong Suppression of Weak Localization in Graphene, Phys. Rev. Lett. 97, 016801 (2006)

[43] D.W. Horsell, A.K. Savchenko, F.V. Tikhonenko, K. Kechedzhi, I.V. Lerner, V.I. Fal'ko, Mesoscopic conductance fluctuations in graphene, Solid State Communications, Volume 149, Issues 27–28, Pages 1041–1045 (2009)

[44] Yung-Fu Chen, Myung-Ho Bae, Cesar Chialvo, Travis Dirks, Alexey Bezryadin, Nadya Mason, Magnetoresistance in Single Layer Graphene: Weak Localization and Universal Conductance Fluctuation Studies, Journal of Physics: Condensed Matter, Volume 22, Issue 20, p. 205301 (2010)

[45] F. Freitag, J. Trbovic, C. Schönenberger, Conductance fluctuations in graphene devices with superconducting contacts in different charge density regimes, Phys. Status Solidi B (2011)

[46] G. Bohra, R. Somphonsane, N.Aoki, Y. Ochiai, R. Akis, D. K. Ferry, J. P. Bird, Nonergodicity and microscopic symmetry breaking of the conductance fluctuations in disordered mesoscopic graphene. Phys. Rev. B 86, 161405 (2012)

[47] Zhi-Min Liao, Bing-Hong Han, Hong-Zhou Zhang, Yang-Bo Zhou, Qing Zhao and Da-Peng Yu, Current regulation of universal conductance fluctuations in bilayer graphene, New Journal of Physics, Volume 12, p. 083016 (2010)

[48] Mohammed S. El-Bana, Daniel Wolverson, David W. Horsell and Simon J. Bending, Localization and field-periodic conductance fluctuations in trilayer graphene, Semicond. Sci. Technol. 29115010 (2014)

[49] J. Trbovic, N. Minder, F. Freitag and C. Schönenberger, Superconductivity-enhanced conductance fluctuations in few-layer graphene, Nanotechnology 21, 274005 (2010)

[50] Chiashain Chuang, et al., Mesoscopic conductance fluctuations in multi-layer graphene, Applied Physics Letters, 103, 043117 (2013)

[51] B. Liu, R. Akis, D. K. Ferry, Conductance fluctuation in semiconductor nanostructure. J. Phys. Cond. Matter. 25, 395802 **(**2013)

[52] T. Usuki, M. Saito, M. Takatsu, R.A. Kiehl, N. Yokoyama, Numerical analysis of ballistic-electron transport in magnetic fields by using a quantum point contact and a quantum wire. Phys. Rev. B 52, 8244 (1995)

[53] R. Akis, D. K. Ferry, Use of the scattering matrix for device simulations. J. Comput. Electron. 12(3), 356–362 (2013)

[54] A. H. Castro Neto, F. Guinea, N. M. R. Peres, K. S. Novoselov, A. K. Geim, The electronic properties of graphene. Rev. Mod. Phys. 81, 109 (2009)

[55] P. W. Anderson, Absence of diffusion in certain random lattices. Phys. Rev. 109, 1492 (1958)

[56] B. Liu, R. Akis, D. K. Ferry, Conductance fluctuations in graphene nanoribbons. J. Comput. Electron. 13(4), 950-959 (2014)

[57] B. Liu, R. Akis, D. K. Ferry, Conductance fluctuations in graphene subjected to short-range disorder, accepted, J. Vac. Sci. Technol. B 33, 04E101 (2015)

[58] E. Rossi, J. H. Bardarson, M. S. Fuhrer, S. Das, Sarma, Universal conductance fluctuations in Dirac materials in the presence of long-range disorder, Phys. Rev. Lett. 109, 096801 (2012)

[59] B. Liu, R. Akis, D. K. Ferry, G. Bohra, R. Somphonsane, H. Ramamoorthy, and J. P. Bird, Conductance fluctuations in graphene in the presence of long-range disorder, submitted (2015)

[60] J. Tworzydlo, C. W. Groth, C. W. J. Beenakker, Finite difference method for transport properties of massless Dirac fermions, Phys. Rev. B 78, 235438 (2008)

[61] Massimo V Fischetti *et al*, Pseudopotential-based studies of electron transport in graphene and graphene nanoribbons, J. Phys.: Condens. Matter 25, 473202 (2013)